UNIVERSITÉ DU QUÉBEC À MONTRÉAL

LES MINÉRALISATIONS AURIFÈRES NÉOARCHÉENNES ASSOCIÉES À LA ZONE DE FAILLES DE PORCUPINE-DESTOR: LA PROPRIÉTÉ DUQUESNE-OTTOMAN, ABITIBI, QUÉBEC, CANADA

MÉMOIRE

PRÉSENTÉ

COMME EXIGENCE PARTIELLE

DE LA MAÎTRISE EN SCIENCE DE LA TERRE

PAR

SACHA LAFRANCE

DÉCEMBRE 2015

REMERCIEMENTS

Je tiens tout d'abord à remercier Michel Jébrak, mon directeur de maîtrise, pour m'avoir permis de poursuivre ma passion, pour ses précieux commentaires, son enthousiasme et ses innombrables idées qui ont permis la réalisation de ce projet.

Je remercie la compagnie d'exploration minière Xmet Inc., le CRSNG et le FQRNT pour le financement. Un grand merci aux géologues d'Xmet Inc. pour leurs conseils, particulièrement Pierre Riopel pour son aide, encadrement et pour les discussions très enrichissantes. Un grand merci à Ludovic Bigot, Stéphane Faure, Noémie Fayol, Yannick Daoudene et Pierre Lacoste pour leurs commentaires très constructifs qui ont grandement amélioré la qualité de cet ouvrage. Merci aux correcteurs, Stéphane De Souza et Jean Goutier, pour la relecture du document. Un grand merci à Michelle Laithier pour son temps et ses conseils qui ont permis l'élaboration des illustrations. Merci à Raynald Lapointe pour l'aide technique, à Denise Roy pour la gestion et à Frédérik Toupin pour le soutien informatique. Je suis aussi très reconnaissant envers la SEG et les chapitres étudiants SEG de l'Université du Québec à Montréal et de McGill pour les bourses et le support à la réalisation des voyages géologiques au Brésil, aux États-Unis, en Ontario et au Québec.

Finalement, mille mercis à ma très chère Ariane pour son merveilleux soutien et sa compréhension. Un grand merci à ma famille et amis, ainsi qu'aux collègues et amis, Nicolas, Christophe, Marion, Samuel, Ludovic, Noémie, Julien, Kristina, Clyde, Christine, Yannick et James.

AVANT-PROPOS

Ce mémoire est rédigé sous la forme d'un article scientifique qui sera soumis à la revue *Canadian Journal of Earth Sciences* sous le titre *Neoarchean Gold Mineralization associated with the Porcupine-Destor fault zone: Duquesne-Ottoman Property, Abitibi Greenstone Belt, Québec, Canada.* Sa présentation diffère des mémoires habituellement présentées à l'Université du Québec à Montréal; la rédaction est en anglais et les figures et tableaux sont situés à la fin de l'article. Michel Jébrak, le directeur de maîtrise, est co-auteur de cet article. Ce format de mémoire a été choisi car il donne l'opportunité de transmettre de nouvelles connaissances à la communauté scientifique à l'échelle internationale.

TABLE DES MATIÈRES

LISTE DES FIGURES

LISTE DES TABLEAUX

RÉSUMÉ

La propriété Duquesne-Ottoman (ressources inférées de 22.6t Au de 4.171 Mt à 5.42 g/t Au) est associée à la Faille Porcupine-Destor au sud de la Sous-province de l'Abitibi, Province du Supérieur, Québec, Canada. La propriété se situe dans la séquence volcanique de compositions felsique à ultramafique de la Formation de Lanaudière coupée par des massifs et dykes porphyriques calco-alcalins et alcalins. Deux phases hydrothermales sont distinguées sur la propriété. La première phase, associée à la zone Fox, se situe au contact entre un massif porphyrique calco-alcalin et des roches volcaniques mafiques et ultramafiques. Cette phase est associée à une altération principale en quartz-calcite-hématite. Elle est aussi associée à des veines épithermales et une minéralisation à pyrite et chalcopyrite, et avec des traces de tellurures et de sulfosels. L'or visible est observé en inclusions et en remplissage de microfractures dans les pyrites. On note dans cette zone un gain géochimique en Au, SiO_2, CO_2, S, Cu et des gains mineurs en Ag, Te, Pb, Zn, Bi and Co. La seconde phase hydrothermale est associée aux zones Shaft et Liz. Elle est située dans des failles secondaire orientées est-ouest recoupant l'ensemble des unités lithologiques. Cette phase est associée à un assemblage d'altération à carbonate de fer, séricite et quartz. La minéralisation consiste de pyrite avec de la chalcopyrite mineure et des traces de tellurures et de sulfosels. On note dans ce second assemblage un gain géochimique en CO_2, K_2O, S, Mo, W, Sb, As, Au et des gains mineurs en Te, Ag, Hg and Ba, et une perte en Sn. La séquence paragénétique des zones Shaft et Liz reflète une évolution de la pyrite et de l'or en plusieurs étapes. Les pyrites à cœur poreux et surcroissances nettes montrent une zonation géochimique nette avec un enrichissement au cœur en Au, Ag et Te. La composition isotopique du soufre ($\delta^{34}S$) de huit échantillons de pyrite des zones Shaft, Liz et Fox montre des valeurs négatives de -12,7 à 0,6 ± 0,2‰. Les relations de recoupement suggèrent que la minéralisation postdate la mise en place d'intrusions calco-alcalines à 2689 ± 3 Ma et est contemporaine de la déformation régionale D_2. Ces deux phases hydrothermales sont interprétées comme une phase épithermale acide à laquelle se superpose une phase aurifère de type orogénique de la transition épizonale-mésozonale. Les caractéristiques de la propriété Duquesne-Ottoman se comparent fortement au gisement d'or Beattie, en partie interprété comme étant d'origine magmatique-hydrothermale. Cette ressemblance pourrait souligner un champ magmatique-hydrothermal relié à l'évènement Timiskaming s'étendant dans la région de Duparquet, de la syénite de Beattie à la propriété Duquesne-Ottoman.

MOTS CLÉS: Minéralisation aurifère orogénique, Abitibi, Porcupine-Destor, Duparquet, porphyre néoarchéen, hydrothermalisme.

INTRODUCTION GÉNÉRALE

Les couloirs de déformation de la Sous-province de l'Abitibi (e.g. Zones de Faille Porcupine-Destor et Larder Lake-Cadillac) sont reconnus pour leur production abondante de gisements aurifères (Goldfarb *et al.*, 2005). Cette richesse, distribuée principalement dans les district minier de Timmins (1980 metric ton (t) Au; Bateman et Bierlien, 2007), Kirkland Lake (797t Au; Goldfarb *et al.*, 2005), et Val-d'Or (900t Au; Olivo et Williams-Jones, 2002), a influencé lors du dernier siècle le développement de modèle portant sur la gîtologie de l'or et la tectonique archéenne. La recherche appliquée à ces structures minéralisées a permis de développer le concept de continuum-crustal (Colvine, 1988; Groves, 1993) essentiel à l'élaboration du modèle de gisement d'or orogénique (Groves *et al.*, 1998). Alors que l'exploration en Abitibi s'est surtout basée depuis les 25 dernières années sur ce dernier modèle, de nouveaux modèles d'exploration, tel que le modèle d'intrusions porphyriques aurifères, ont été développés et testés, parfois avec succès (p.ex. mine Canadian Malartic). Toutefois, la nature complexe de l'environnement orogénique associée à ce type de gisement impose une prudence de l'interprétation génétique des gisements aurifères. Puisque les gisements hydrothermaux aurifères peuvent se former à toutes les étapes d'une orogénie, la juxtaposition, la surimposition ou la remobilisation de plusieurs types de gisements est probable (Robert *et al.*, 2005) et soulève de nombreuses interrogations sur la genèse de ces minéralisations (Groves *et al.*, 2003). L'hétérogénéité des caractéristiques de certains gisements le long des grands corridors de déformation (Berger, 2001; Rafini, 2014) et l'incertitude des âges de minéralisations imposent une remise en question de certains aspects de ce modèle. Des pistes de recherche nouvelles et revisitées ont récemment été proposées pour l'évolution hydrothermale et la source de l'or des gîtes orogéniques dans d'autres environnements géologiques tel que: sédimentaire

(Large *et al.*, 2011; Gaboury, 2013), métamorphique (Goldfarb *et* al., 2005; Pitcairn *et al.*, 2006) et magmatique (Robert, 2001; Goldfarb *et al.*, 2005; Bigot et Jébrak, 2015). Dans la perspective magmatique, l'évènement néoarchéen «Timiskaming» (~2682-2670 Ma; Robert, 2001; Ayer *et al.*, 2005; David *et al.*, 2011) auquel sont associés la sédimentation fluviatile-alluviale du Groupe de Timiskaming et un épisode de magmatisme alcalin diagnostique est d'intérêt majeur dans l'ensemble de Sous-province de l'Abitibi. Une compréhension de la genèse et des mécanismes de minéralisation liés à cet évènement participerait à préciser les complexités associées au modèle d'or orogénique et ses sources d'or potentiel. Dans la région de Duparquet, l'attention a été concentrée sur le gisement d'or à sulfures disséminés de la syénite de Beattie (Bigot et Jébrak, 2015). Et pour cause, ce gisement est le plus gros du camp minier de Duparquet avec une production historique de 1931 à 1956 d'environ 31.2t d'or extrait de 10Mt de matériau, d'une teneur de 3.92 g/t Au (Bigot and Jébrak, 2015) et des ressources actuelles mesurées et indiquées de plus de 96.4t d'or extrait de 60.9Mt à 1.59 g/t Au (Bigot and Jébrak, 2015). D'autres gisements d'or ont également fait l'objet de production historique dans le camp minier de Duparquet tels que les mines Yvan-Vézina (1.1 Mt à 3.72 g/t Au; Legault *et al.*, 2005), Duquesne (3.1t à 10.31 g/t Au; Legault *et al.*, 2005), et Davangus (32 120 t à 4.31 g/t Au; Legault *et al.*, 2005). Plusieurs autres gîtes d'or, dont celui de la propriété Duquesne-Ottoman, sont présentement la cible de travaux d'exploration. À ce jour, la typologie descriptive de Legault *et al.* (2005) représente le seul travail métalogénique effectué sur l'ensemble du camp minier de Duparquet. Les six types de minéralisation identifiés par ces auteurs sont: (1) veines de quartz + carbonates, (2) sulfures disséminés associés à une intrusion porphyrique, (3) veine épithermale, (4) veine de quartz argentifère, (5) sulfures disséminés associés à un lessivage et (6) sulfures massifs volcanogènes.

L'objectif principal de cet ouvrage est d'approfondir la compréhension métallogénique de la propriété Duquesne-Ottoman, en caractérisant ses principales zones aurifères, en déterminant la nature et les contrôles de la minéralisation et en établissant son évolution géologique par rapport à la région de Duparquet. Afin d'y arriver, plusieurs aspects de la géologie ont été étudiés. La caractérisation pétrologiques et minéralogiques des roches de la propriété s'est faite par l'analyse de lames minces polies au microscope optique et au microscope électronique à balayage. Cette étude a permis de développer la typologie du gîte, de déterminer la distribution des altérations et de la minéralisation sur le terrain et la séquence paragenétique qui le caractérise. Les analyses géochimiques de roche totale et de composition isotopique du soufre de la pyrite ont permis de préciser la nature des fluides hydrothermaux impliqués dans la minéralisation aurifère. L'approche multidisciplinaire de cette recherche a permis de contextualiser la minéralisation de la propriété Duquesne-Ottoman dans l'histoire géologique de la région de Duparquet.

Ce mémoire est présenté sous la forme d'un article scientifique qui sera soumis à une revue scientifique qui traite entre autres de géologie économique. L'article a été rédigé par le premier auteur, tandis que le second auteur, Michel Jébrak, a agis à titre de directeur de maîtrise. L'implication de ce dernier s'est faite par l'élaboration et le suivi de pistes de recherche, l'aide de terrain, le soutien financier et la relecture de l'article.

L'article présente tout d'abord la problématique, la géologie régionale du sud de l'Abitibi et la géologie du secteur de Duparquet sous les thèmes stratigraphiques et structuraux. Les techniques d'échantillonnage et les méthodes analytiques sont ensuite détaillées. S'en suit la géologie de la propriété Duquesne-Ottoman : en premier lieu la pétrographie et géochimie des roches encaissantes, puis la typologie des altérations et leur géochimie respective, la

caractérisation des types de minéralisation, leur minéralogie et la séquence paragenétique, suivent la cartographie géochimique et la composition isotopique du soufre des pyrites. Une discussion soulève et interprète les caractéristiques pétrologiques, structurales, d'altération et de la minéralisation qui permettent la distinction de deux phases hydrothermales distinctes. Ces phases sont classées par types métallogéniques et mise en contexte historique par rapport à l'évolution géologique du secteur de Duparquet. La discussion se termine par une comparaison avec d'autres gisements aurifères similaires. La conclusion souligne les points importants et met de l'avant les idées proposées au cours de ce projet de recherche.

Référence

Ayer, J. A. et Ontario Geological Survey. (2005). Overview of results from the greenstone architecture project: discover Abitibi initiative. Ontario Geological Survey.

Bateman, R. et Bierlein, F. P. (2007). On Kalgoorlie (Australia), Timmins–Porcupine (Canada), and factors in intense gold mineralisation. Ore Geology Reviews, 32(1), p. 187-206.

Berger, B. R. (2001). Variation in styles of gold mineralization along the Porcupine–Destor deformation zone in Ontario: an exploration guide. Ontario Geological Survey Open File Report, 6070, 9-1.

Bigot, L. et Jébrak, M. (2015). Gold Mineralization at the Syenite-Hosted Beattie Gold Deposit, Duparquet, Neoarchean Abitibi Belt, Canada. Economic Geology, 110(2), p.315-335.

Colvine, A. C. (1988). Archean lode gold deposits in Ontario, Ontario Ministry of Northern Development and Mines, Vol. 139, 136 p.

David, J., McNicoll, V., Simard, M., Bandyayera, D., Hammouche, H., Goutier, J., Pilote, P., Rhéaume, P., Leclerc, F. et Dion, C. (2011).Datations U-Pb effectuées dans les provinces du Supérieur et de Churchill en 2009-2010. Ressources naturelles et faune Québec, 37p.

Gaboury, D. (2013). Does gold in orogenic deposits come from pyrite in deeply buried carbon-rich sediments?: Insight from volatiles in fluid inclusions. Geology, 41(12), p.1207-1210.

Goldfarb, R.J., Baker, T., Dubé, B., Groves, D.I., Hart, C.J.R. et Gosselin, P. (2005). Distribution, character, and genesis of gold deposits in metamorphic terranes. Economic Geology 100th anniversary, Vol. 40, p. 407-450

Groves, D. I. (1993). The crustal continuum model for late-Archaean lode-gold deposits of the Yilgarn Block, Western Australia. Mineralium deposita, 28(6), p. 366-374.

Groves, D. I., Goldfarb, R. J., Gebre-Mariam, M., Hagemann, S. G. et Robert, F. (1998). Orogenic gold deposits: a proposed classification in the context of their crustal distribution and relationship to other gold deposit types. Ore geology reviews, 13(1), p. 7-27.

Groves, D. I., Goldfarb, R. J., Robert, F. et Hart, C. J. (2003). Gold deposits in metamorphic belts: overview of current understanding, outstanding problems, future research, and exploration significance. Economic Geology, 98(1), p. 1-29.

Large, R. R., Bull, S. W. et Maslennikov, V. V. (2011). A carbonaceous sedimentary source-rock model for Carlin-type and orogenic gold deposits. Economic Geology, 106(3), p. 331-358.

Legault, M., Goutier, J., Beaudoin, G. et Aucoin, M. (2005). Synthèse métallogenique de la faille Destor-Porcupine, Ministère des Ressources Naturelles et de la Faune, Québec;
ET 2005-01, 37 p.

Olivo, G. R. et Williams-Jones, A. E. (2002). Genesis of the auriferous C quartz-tourmaline vein of the Siscoe mine, Val d'Or district, Abitibi subprovince, Canada: structural, mineralogical and fluid inclusion constraints. Economic Geology, 97(5), p.929-947.

Pitcairn, I. K., Teagle, D. A., Craw, D., Olivo, G. R., Kerrich, R. et Brewer, T. S. (2006). Sources of metals and fluids in orogenic gold deposits: insights from the Otago and Alpine Schists, New Zealand. Economic Geology, 101(8), p.1525-1546

Rafini, S. (2014). Typologie des minéralisations aurifères associées à la Faille de Cadillac. Rapport du projet CONSOREM 2011-01 et 2012-01, 45p.

Robert, F. (2001). Syenite-associated disseminated gold deposits in the Abitibi greenstone belt, Canada. Mineralium Deposita, 36(6), p. 503-516

Robert, F., Poulsen, K. H., Cassidy, K. F. et Hodgson, C. J. (2005). Gold metallogeny of the Superior and Yilgarn cratons. Economic Geology 100th anniversary, p. 1001-1033.

CHAPITRE 1

NEOARCHEAN GOLD MINERALIZATION ASSOCIATED WITH THE PORCUPINE-DESTOR FAULT ZONE: DUQUESNE-OTTOMAN PROPERTY, ABITIBI BELT, QUÉBEC, CANADA

Abstract

The Duquesne-Ottoman property (inferred resources of 26.2t of gold from 4.171 Mt grading 5.42 g/t Au) is located along the Porcupine-Destor fault zone (PDFZ), in the southern Abitibi greenstone belt of the Superior Province, Québec, Canada. It is hosted by Archean felsic to ultramafic volcanic rocks of the Lanaudière Formation, which is intruded by Neoarchean calc-alkaline and alkaline porphyritic stocks and dykes, and unconformably overlain by fluvial-aluvial sedimentary rocks of the Timiskaming Group. Two hydrothermal events are distinguished on the property. Associated with the Fox zone, the first event is located at the high-strained contact between a large calc-alkaline porphyry stock and the volcanic rocks of the Lanaudière Formation. The Fox zone consists of a quartz-calcite-hematite alteration assemblage with ore mineral consisting of pyrite, hematite and chalcopyrite, and with minor epithermal veining. Visible gold occurs in pyrite as inclusions and filling late microfractures. This hydrothermal event shows notable gains in Au, SiO_2, CO_2, S, Cu and a minor input in Ag, Te, Pb, Zn, Bi and Co. The second hydrothermal event, in the Shaft and Liz zones, is principally hosted in east-trending second-order shear zones overprinting all rock types and associated with a ferroan carbonate-sericite-quartz alteration assemblage. Ore minerals include mainly pyrite, minor chalcopyrite, and traces of tellurides and sulphosalts. This event displays notable gains in CO_2, K_2O, S, Mo, W, Sb, As and Au, with minor input in Te, Ag, Hg and Ba,

and loss in Sn. Ore paragenesis reflects a multistage evolution of pyrite and gold. Pyrite displays a distinct geochemical zonation with a porous core enriched in Au, Ag and Te, and numerous overgrowths. Negative $\delta^{34}S$ isotopic composition of eight pyrite samples collected on the property ranges from -12.7 to 0.6 ± 0.2 ‰. Overprinting relationships for this event indicate that gold deposition postdates emplacement of intrusions at 2689 ± 3 Ma during a regional D_2 phase of deformation. The nature of these two distinct hydrothermal events may be explained by an early syenite-related high-sulphidation epithermal mineralization overprinted by an epizonal to mesozonal orogenic gold deposit. Features of the Duquesne-Ottoman Property are strongly comparable to the Beattie gold deposit, which is at least in part interpreted as magmatic-hydrothermal. Their similarities between these two sites, in terms of petrology, structural evolution, alteration and mineralization, may underline a syenite-related magmatic-hydrothermal event extending from the Beattie syenite to the Duquesne-Ottoman property.

KEYWORDS: Orogenic gold mineralization, Abitibi, Porcupine-Destor, Duparquet, Neoarchean porphyry, hydrothermalism.

1.1 Introduction

The Duquesne-Ottoman property (DOP) is located in the Archean Abitibi greenstone belt of the Superior Province (Fig. 1), within a kilometer north of the PDFZ, on the southern margin of the Duparquet fluvial-aluvial sedimentary basin (Fig. 2). Along with the Larder Lake-Cadillac fault zone (Fig. 1), these regional deformation corridors have been of great economic and scientific interests over the last century, as these large deformation corridors host many world class gold mining camp, such as the Timmins (1980t Au; Bateman and Bierlein, 2007), Kirkland Lake (797t Au; Goldfarb *et al.*, 2005) and Val-d'Or (900t Au; Olivo and Williams-Jones, 2002) districts. Scientifically, research on these mineralized

structures has led in part to the development of the crustal-continuum model (Colvine, 1988; Groves, 1993) central to the development of the orogenic gold deposit model (Groves *et al.*, 1998) which has been revised over time to better represent the variety and the complexity of this style of deposit. However, several unanswered questions remain (Groves *et al.*, 2003), and new and revisited lines of investigation have recently been proposed for the hydrothermal evolution and the source of gold in orogenic deposits in different environments: sedimentary (Large *et al.*, 2011; Gaboury, 2013), metamorphic (Goldfarb *et* al., 2005; Pitcairn *et al.*, 2006) and magmatic (Robert, 2001; Goldfarb *et al.*, 2005; Bigot and Jébrak, 2015). In the magmatic perspective, the Neoarchean Timiskaming event (Robert, 2001, Robert *et* al., 2005; Bleeker, 2012, 2015) which is associated with diagnostic alkaline magmatism and fluvial-alluvial sedimentation of the Timiskaming Group, is of major interest throughout the southern Abitibi greenstone belt.

In the Duparquet area, exploration work has been focused on the Beattie syenite-associated disseminated gold deposit (including the Beattie mine and Donchester mine) the largest deposit of this mining camp, with past-productions from 1931 to 1956 of approximately 31.2t of gold extracted from 10Mt of material, at an average grade of 3.92 g/t Au (Bigot and Jébrak, 2015). Recent exploration work established measured and indicated resources of 96.4t of gold extracted from 60.9Mt, grading 1.59 g/t Au (Bigot and Jébrak, 2015). Several other smaller deposits are also present in the Duparquet mining camp, such as those of the past-producing Yvan-Vézina (1.1Mt grading 3.72 g/t Au; Legault *et al.*, 2005), Duquesne (1.0Mt grading at 10.31 g/t Au; Legault *et al.*, 2005) and the Davangus mines (32 120 t grading 4.31 g/t Au; Legault *et al.*, 2005). The DOP, which is the focus of this study, comprises six gold zones (Power-Fardy and Breede, 2011): the Liz, Shaft (including North Shaft and South Shaft), Fox,

Stinger, 20-20 and the Nip (both Nip-North and Nip-South) zones. From 2010 to 2013, intense exploration work conducted by Xmet Inc. established for the DOP inferred resources of 22.6t of gold (capped with a cut-off grade of 30.0 g/t Au) from 4.171 Mt grading at 5.42 g/t Au (capped) (Power-Fardy and Breede, 2011). To date, five main types of mineralization are identified by Legault *et al.* (2005) in the Duparquet area: (1) Quartz + carbonate veins, (2a) disseminated sulphides associated with calc-alkaline porphyritic intrusions, (2b) disseminated sulphides associated with alkaline porphyritic intrusions (3) epithermal veins, (4) disseminated sulphides associated with leaching and,(5) sulphides associated with volcanogenic massive sulphides.

The objectives of this paper is to (1) characterize the DOP main gold zones entitled Liz, Shaft and Fox; (2) establish the geological evolution of the area; and (3) put the observations in the metallogenic context of the Duparquet area. In order to accomplish these objectives, this paper documents the geological setting, the mineralogy and geochemical signatures of mineralization and alteration and provides detailed characterization of the main ore mineral, as well as sulfur stable isotopic composition and LA-ICP-MS geochemical map of pyrite.

1.2 Regional geology

Extending roughly 700 km east-west and 300 km north-south, the Abitibi greenstone belt is the world's largest Archean greenstone belt (Card. 1990). In Québec, it is bounded to the south by Neoarchean sedimentary rocks of the Pontiac Subprovince, and to the north by granitoid and orthogneiss of the Opatica Subprovince (Card, 1990; Percival, 2007; Stott *et al.*, 2010). The belt is truncated to the west by the Paleoproterozoic Kapuskasing structural zone and to the east by the orogenic front of the Mesoproterozoic Grenville Province (Percival, 2007; Stott *et al.*, 2010).

Various Archean plate tectonic models involving allochtonous terranes accretions, in which the PDFZ represents an Archean tectonic suture between the Northern Volcanic Zone and the Southern Volcanic Zone has been proposed (Mueller *et al.*, 1996, Polat and Kerrich, 2001; Daigneault *et al.*, 2002). The Northern Volcanic Zone is interpreted by Chown *et al.* (1992) as a diffuse monocyclic oceanic arc system developing, by arc unroofing, into a polycyclic back-arc system, whereas the Southern Volcanic Zone has been interpreted by some authors (Dimroth *et al.*, 1982; Daigneault *et al.*,2002) as a homoclinal oceanic floor-to-arc succession. Alternative autochthonous models have also been proposed (Ayer *et al.*, 2002; Bédard *et al.*, 2013), where the PDFZ represents an evolved anticline fold detachment in a large autochthonous terrane (Benn and Peschler, 2005; Bédard *et al.*, 2013). The PDFZ is interpreted by Goutier (1997) as the imbrication site for the between the Blake River, Malartic and Kinojévis tectonic blocs.

The early construction of the Abitibi greenstone belt by several volcanic episodes, along with minor sedimentation and coeval TTG plutonism, occurred between ca. 2750 and 2697 Ma (Ayer *et al.*, 2002; Thurston, *et al.* 2008). A subsequent period of flyshoid sedimentation followed between ca. 2690 and 2685 Ma (Ayer *et al.*, 2005; Thurston *et al.*, 2008). Following deposition, a polyphased tectonic evolution affected the southern Abitibi greenstone belt (Bleeker and Parrish, 1996; Daigneault *et al.*, 2002; Bleeker, 2012, 2015). A first episode of N-S shortening (D_1) is recognized in the southern volcanic zone as tilting, folding and local thrusting and was accompanied by the intrusions of calc-alkaline "syntectonic" high-level porphyries between *ca.* 2695 and 2685 Ma (Chown *et al.*, 2002; Ayer *et al.*, 2005). A subsequent period of uplift and erosion led locally to the formation of basins along major faults between 2678.9 ± 2.8 (U/Pb on detrical zircon; David *et al.*, 2006) and 2672 Ma (Corfu *et al.*, 1991;

Corfu, 1993), and to the deposition of the Timiskaming-type fluvial-alluvial sedimentary rocks above angular unconformities. The emplacement of alkaline "late syntectonic" intrusions and their local volcanic equivalents between *ca.* 2682 and 2670 Ma in the Kirkland Lake area (Corfu *et al.*, 1991; Chown *et al.*, 2002; Ayer *et al.*, 2005; David *et al.*, 2011) is coeval with the Timiskaming-type sedimentation and represents the "Timiskaming event" (Robert, 2001, Robert *et* al., 2005; Bleeker, 2012, 2015). Timiskaming-type sequences are well preserved in multiple areas in the Abitibi belt, such as the Kirkland Lake, Larder Lake, Matachewan, Granada, Timmins and Duparquet mining camps (Fig. 1). The Timiskaming event was followed by the main period of greenstone belt deformation, responsible for a regional N-S shortening (D_2) that produced thick-skinned thrusting, east-west trend of lithologic units, upright folds and the formation of a penetrative foliation (S_2) in the southern part of the Abitibi belt (Daigneault *et al.*, 2002, 2004; Bleeker, 2012, 2015). The D_2 deformation event evolved gradually into dextral transcurrent deformation (D_3) localized mainly along major fault zones (Daigneault *et al.*, 2002, 2004; Bleeker, 2012, 2015). The D_2-D_3 event was partly accompanied, and outlasted, by the latest Archean intrusions, grouped as "post-tectonic intrusions" of monzogranitic composition such as the flat-lying Pressiac and Lamotte intrusions in Québec dated at 2660 Ma (Chown *et al.*, 2002). Subsequent deformational events (D_4-D_8) are described in the SVZ (Daigneault *et al.*, 2002) but are not the focus of this paper.

Regional metamorphism in the south volcanic zone spans from sub- to greenschist grade facies, with lower amphibolite grade facies locally surrounding intrusions (Powell *et al.*, 1995) and occurring in depth (>1km) along major faults (Simard *et al.* 2013).

1.3 Geology of the Duparquet area

The DOP is located in the central sector of the Duparquet basin, along second-order faults located between the PDFZ to the south and a large stock of quartz-feldspar porphyry to the north. The Duparquet basin is defined as a synclinal sedimentary basin located east of the town of Duparquet and north of the PDFZ (Fig. 2), where the majority of the Duparquet Formation sedimentary rocks of the Timiskaming Group where deposited.

1.3.1 Stratigraphy

The geology of the Duparquet area (Fig. 2) consists of a complex arrangement of heterogeneously deformed volcano-sedimentary rock assemblage divided, from oldest to youngest, into the Kinojévis and Blake River volcanic groups, the Porcupine and Timiskaming metasedimentary groups and is host to four main types of intrusions (Fig. 3). Nevertheless, the presence of high-level calc-alkaline and alkaline porphyries and penecontemporaneous Timiskaming Group conglomerates suggests that outliers of upper- to supracrustal rocks are preserved within the Duparquet basin. The oldest metavolcanic rock assemblage of the area belongs to the Kinojévis Group, which encompasses the Deguisier and Lanaudière Formations. The Deguisier Formation (2719 - 2718 Ma; Pilote *et al.*, 2009) is constituted of abundant Fe-Mg tholeiitic massive and pillowed basalts, with minor andesite, rhyolite and pyroclastic rocks (Goutier and Lacroix , 1992). It is overlain by the Lanaudière Formation (2718-2716 Ma; Pilote *et al.*, 2009), which is described as predominantly Fe-Mg tholeiitic basaltic rocks with lesser amounts of intercalated rhyolite, andesite and komatiite (Goutier and Lacroix , 1992). This unit correlates with the 2719 to 2711 Ma volcanic episode of the Kidd-Munro assemblage in Ontario (Thurston *et al.*, 2008). The Kinojévis Group is interpreted by Kerrich *et al.* (2008) to represent oceanic crust formation in a back-arc rift setting.

The youngest metavolcanic assemblage of the area is the Hébécourt Formation of the Blake River Group (2704 - 2695 Ma; Thurston *et al.*, 2008). Located south of the PDFZ, it consists of tholeiitic, transitional, and calc-alkaline submarine volcanic successions (McNicoll *et al.*, 2014).

The Mont-Brun Formation of the Kewagama Group consists of deep-water turbiditic sandstones and mudrocks (Goutier and Lacroix , 1992) that locally unconformably overlie the Deguisier Formation (Fig. 2), and were deposited between 2686 ± 4 Ma (Ayer *et* al., 2005) and 2681 ± 1.1 Ma (Mueller *et al.*, 2012). The source for the Porcupine Group sediments would come from the erosion of mafic volcanic rocks from the oldest assemblages of the Abitibi greenstone belt as suggested by U-Pb detrital zircon dating (Ayer *et al.*, 2002, 2005). The youngest metasedimentary rock unit is the Duparquet Formation of the Timiskaming Group, which forms an EW-trending corridor along of the Duparquet basin (Fig. 2). This unit consists of polymictic conglomerate and sandstone recording deposition in alluvial fan, fan-delta and/or a braid delta adjacent to a sea or lake (Mueller *et al.*, 1996; David *et al.*, 2006), with an estimated maximal age of deposition of the polymictic conglomerate of 2679 ± 2.8 Ma (U/Pb on detrital zircon), and suggesting a proximal source for the volcanic and intrusive fragments.

Multiple ultramafic to felsic and alkaline intrusions occur in the area. Mafic and ultramafic intrusions occur as < 300m thick, irregular to tabular bodies (Bourdeau, 2013). A portion of these intrusions are interpreted as synvolcanic sills coeval with the Kinojévis Group (Bourdeau, 2013; Goutier, 1997). The oldest intermediate to felsic intrusions (2689 ± 3 Ma; Mueller *et al.*, 1996) are composed of quartz-feldspar (QFP) and feldspar porphyry (FP) of andesitic to rhyodacitic composition with a calc-alkaline affinity (Legault *et al.*, 2005). They intrude the Lanaudière Formation typically as dykes and are

truncated by the unconformity making the base of the Timiskaming Group. Geointegrated 3-D modeling (see Fig. 8 of Legault *et al.*, 2003) in the Duparquet area shows that the porphyry stocks are subparallel to the east-west structural trend of the basin at surface and in depth. Based on their age, spatial distribution, porphyritic texture and geochemistry, these intrusions are interpreted as syntectonic intrusions emplaced at shallow depths (Goutier and Lacroix, 1992). The youngest intermediate to felsic intrusions are of alkaline composition (2682.9 ± 1.1 Ma; David *et al.*, 2006; 2681.6 ± 1 Ma; Mueller *et al.*, 1996), and outcrop in the Duparquet area in two locations: in the area of the Beattie mine and to a lesser extent, in the DOP area (Fig. 2). They are described as small porphyritic stocks spatially associated with the PDFZ (Bigot and Jébrak 2015), and range in composition from quartz-monzonite to syenite (Bourdeau, 2013; Bigot and Jébrak, 2015). In the Duparquet area, all observed syenite bodies are truncated by the Timiskaming unconformity and all documented phases occur as clasts in the overlying Timiskaming conglomerate (Mueller *et al.* 1991). Therefore, these intrusions predate sedimentation of the Timiskaming Group, which is consistent with published U/Pb zircon crystallization (Mueller *et al.*, 1996; David *et al.*, 2007) and detrital ages (David *et al.*, 2006). As for the calc-alkaline intrusion, these alkaline intrusions are interpreted as syntectonic intrusions emplaced at shallow depths (Goutier and Lacroix, 1992)

1.3.2 Structural geology

The stratigraphic units of the Duparquet area have undergone polyphase deformation, resulting in a heterogeneous and complex structural pattern and a southward increasing strain gradient toward the PDFZ (Fig. 2). A first deformational event (D_1) is responsible for the E-W to ENE-trending large scale folds (F_1) and the tilting to the north of the Lanaudière and Deguisier Formation (Beaudry, 1992; Goutier and Lacroix, 1992; Goutier, 1997). The F_1 folds are truncated by the Duparquet Formation. The development of schistosity (S_1)

prior to the Duparquet Formation is demonstrated by the presence of shistosed volcanic fragments within the Duparquet Formation and porphyry intrusions (Goutier and Lacroix, 1992; Legault *et al.*, 2005). The D_1 event is interpreted as a N-S shortening event. A subsequent phase of local N-S extension is suggested to explain the formation of the Duparquet basin and related deposition of Timiskaming-type sediments as well as the emplacement of high-level porphyry intrusions. This extensive phase is interpreted by Mueller *et* al. (1996) as the result of a syn-D_2 strike-slip movement along the PDFZ, whereas it is interpreted by Bleeker (2012, 2015) as a sharp phase of pre-D_2 synorogenic extension. As shown by Goutier and Lacroix (1992), a number of EW-trending faults in the sector are not related to the PDFZ but are rather predating or contemporaneous with the formation of the Duparquet basin. Following this event, a second contractional event (D_2) led to the development of the first-order crustal-scale PDFZ, multiple second-order faults, EW- to ENE-trending penetrative schistosity (S_2) and small-scale Z-shaped folds (F_2). These structures truncate all lithologies. The ESE-trending PDFZ dips from 50° to 80° to the south, displays a variable thickness of 15 to 200 meters and is characterized by a strong mylonitic fabric and intense hydrothermal alteration (Goutier and Lacroix, 1992). Multiple discontinuous bands of talc-carbonate-chlorite schist mark the trace of the PDFZ. Kinematic indicators along the PDFZ in the Duparquet area suggest a north-verging reverse displacement with a dextral component (Goutier and Lacroix, 1992) or a dextral transpression (Dimroth *et al.*, 1983a; Mueller *et al.*, 1996). The second-order faults are EW- to ENE-striking and steeply south-dipping (Goutier and Lacroix, 1992). A subsequent episode (D_3) of dextral strike-slip movement reactivated the PDFZ and the second-order faults (Goutier and Lacroix, 1992). A late N-S compression event (D_4) generated conjugate NE-SW and NW-SE brittle faults, which overcut all lithologies and pre-existing structures.

In the Destor township area, about ten kilometers east of the DOP, the PDFZ separates into numerous second-order faults of contrasting attitude and kinematics (Goutier, 1997), suggesting multiple distinctive deformational event for the evolution of the PDFZ in this sector. On a regional scale, numerous kinematics were identified along the strike of the PDFZ, ranging from thrusting in the Manneville segment of the fault (Mueller *et al.*, 1996), to sinistral strike-slip (Hubert *et al.*, 1984) or thrust imbrication (Jackson *et al.*, 1990).

1.4 Sampling and analytical methods

Samples for the petrological and geochemical study were collected both from trenches and from six drill holes of the DOP. The drill holes that were sampled (DO-11-23, DO-11-40, DO-11-51, DQ-04-22, DO-12-71 and DO-12-73) intersect the stratigraphic units and faults that host the Shaft, Liz, South and Fox ore zones, which are the main zones that were studied for the analysis of the deposit. The localization of samples and pictures presented in this study are synthesised (Table 1 and Figure 1 and 2; Annexe A).

The East-Shaft trenches were mapped in the summer of 2012 by the first author. The objective was to characterize the host rocks, structural features as well as alteration typology and distribution in order to establish their relationship with gold mineralization.

Whole-rock major and trace element concentrations (Table 1) were determined by inductively coupled plasma-mass spectrometry (ICP-MS; lithium tetraborate and lithium metaborate fusion followed by dissolution) and trace and precious metals by instrumental neutron activation analysis (INAA). The samples were analyzed at Techni-Lab S.G.B Abitibi inc., Sainte-Germaine, Canada.

Ore mineralogy and textures were examined under a Leica DMLP transmitted-reflected light polarizing microscope. Further investigations were performed with a Hitachi TM-3000 scanning electron microscope at Université du Québec à Montréal, QC, Canada.

Concentrations of trace elements in pyrite were determined by laser-ablation inductively coupled plasma mass spectrometry (LA-ICPMS) at the LabMaTer of Université du Québec à Chicoutimi, QC, Canada. The instrumentation used is a 193-nm M-50 resolution Excimer ArF resonetics laser microprobe coupled with an Agilent 7700x mass spectrometer. Analyses were performed in spot mode using a laser beam of 15 μm, a laser repetition rate of 15 Hz and with laser energy of 5 mj/cm^2. Data were collected in the time-resolved mode with analysis time at 90 s, including a 30 s preablation background measurement. This enabled a 50 s interval of data acquisition rastering at a rate of 10 μm/s under a fixed beam. The data produced by this technique were treated by the IOLITE 2.5 software. All analyses were quantified against GSE and Mass-C standard using Fe as the internal standard. Standards were analyzed before and after the acquisition to assess drift.

Sulfur isotope compositions were measured in the three main mineralized zones. Eight pyrite grains aggregates fluid from ore and quartz-feldspar porphyry have been analyzed at the Queen's Facility for Isotope Research at Queen's University, ON, Canada. Sulfur isotopes were measured using a Carlo Erba NCS 2500 Elemental Analyzer coupled to a MAT 252 Stable Isotope Ratio Mass Spectrometer (IRMS). $\delta^{34}S$ values are reported using the delta (δ) notation in units of permil (‰) and were calculated by normalizing the $^{34}S/^{32}S$ ratios in the sample to the same ratio in the Vienna Canyon Diablo Troilite (VCDT) international standard, with a precision of 0.2‰.

1.5 Geology of the Duquesne-Ottoman property

The rock sequence at the DOP consists of a rheologically and geochemically heterogeneous package of metamorphosed, highly deformed, and altered rocks. The dominant lithologic group, composed of basalt, rhyolite, and komatiite of the Lanaudière Formation, is located between the clastic sedimentary rocks of the Duparquet Formation and a large calc-alkaline porphyry (North Porphyry) stock to the north, and the Porcupine-Destor fault zone to the south (Fig. 4, 5). Multiple calc-alkaline porphyries, a few alkaline intrusions and rare ultramafic intrusions overcut the volcanic rocks. Deformation is heterogeneously distributed and partitioned into second-order deformation zones and high-strain zones, which are in part controlled by competency contrasts as evidenced by the deformation being preferably developed in less-competent mafic to ultramafic rocks (Fig. 5, 6). Field observations of the deformation zone at the East-Shaft trenches exhibit evidences of non-coaxial deformation, as illustrated by z-shaped folds, s-c structures, asymmetric boudins and pinch-and-swell structures (Fig, 6). The second-order deformation zone in the DOP area can therefore be classified as shear zones. A preliminary study of the deformation of quartz and feldspar phenocryst in mafic and felsic rocks located in the second-order shear zone of the East-Shaft trenches has broadly constrained the structural regime for the area to the brittle-plastic transition (Appendice A). The shear zones are 5 to 20 m thick, E-striking steeply dipping to the south, with stretching-lineation plunging ~60-70° to the east (Fig. 6) and a reverse-dextral sense of shear (Fig. 6). Foliation and crenulation is well developed in intermediate to ultramafic rocks within the shear zone boundary. Gold mineralization on the DOP is principally hosted in second-order shear zone zones and at the southern high-strain contact between the North Porphyry and the volcanic rocks of the Lanaudière Formation.

1.5.1 Host rocks

Petrographic descriptions of the Duparquet area and the Beattie syenite area are given in (Goutier and Lacroix, 1992) and Bourdeau (2013), respectively. This section provides a petrographical and geochemical description for the rocks of the DOP.

1.5.1.1 Petrography

In the Lanaudière Formation, ultramafic rocks are volumetrically minor, strongly foliated and altered, especially by iron-carbonatization, and occur as metric bands align in foliation or in contact with calc-alkaline intrusions (Fig. 8A). These rocks display a dark-coloured aphanitic matrix, with locally preserved relics of original spinifex textures in zones of low strain, indicating Archean ultramafic volcanism. No unaltered komatiite have been found in the DOP to describe in further details the primary mineralogy of this unit. Basalt, the dominant lithology in the DOP area, is fine- to medium-grained, and weakly to strongly foliated. Least-altered basalt is composed of chlorite, plagioclase feldspar, pyroxene, carbonate, Ti oxides, quartz and epidote. Basaltic rocks exhibit a variety of textures, including massive, pillowed, vesicular, amygdaloidal and porphyritic textures, with millimetric feldspar or chloritized ferromagnesian phenocryst. Andesite is also present and is petrographically very similar to the basaltic rocks, although they are showing more strongly chloritized or sericitized feldspar phenocrists. Rhyolite is typically massive and locally exhibit amoeboidale and brecciated flow structures (Fig. 8B). They are characterized by an aphanitic groundmass of quartz and feldspathic composition and round, millimetric quartz phenocryst (< 5%).

Quartz-feldspar porphyries form small to large discordant stocks (e.g. North Porphyry, Fig. 4) and dykes that are weakly to strongly deformed. The larger stocks accommodate deformation mostly at their boundary, whereas the smaller dykes are elongated and transposed subparallel to second-order shear zone (Fig.4, 5). They display a porphyritic texture, with a fine-grained matrix of quartz and feldspathic composition, millimetric plagioclase feldspar laths (30-40%), round, centimetric quartz phenocryst (10 %) and millimetric idiomorphic biotite phenocryst (<3%) (Fig. 8C). Feldspar porphyries are similar to quartz-feldspar porphyries as they display a fine-grained matrix, millimetric plagioclase feldspar laths (40-50%) but lack quartz phenocrysts.

A particular breccia is located at the 20-20 zone's trenches (Fig. 4). It is partially enclosed within the North porphyry and preserved in a zone of low strain. It is polymictic, with quartz-feldspar porphyritic rock as the main component (~90%) and contains minor amounts of white aplitic rock (<5%), mafic volcanic rocks (<2%), chert (<1%), fuchsite-altered volcanic rock (<1%), quartz and epithermal veins (<1%) (Fig. 8D). The clast-supported breccia is intercalated by fine-grained silt layers, displays a disorganized east-west trending fabric and has a polydisperse particle size distribution with millimetric to decametric clasts. The clasts are sub-rounded to angular and have an approximate 1:1 to 1:5 aspect ratios. Although this breccia may simply be related to the Timiskaming Group conglomerates, numerous elements may elsewise suggest a felsic subvolcanic explosive origin with subsequent clasts transport and sedimentation, such as the quartz and epithermal vein fragments, the angular clasts, the disorganized fabric, mostly monogenic QFP fragments and a close spatial relationship with the North Porphyry. The intercalation of silt layers in the breccia is consistent with a post-collapse reworking. Further investigation is nevertheless required to confirm this interpretation.

Based on petrographic observations, the pinkish to reddish intrusive rocks on the DOP are referred as quartz-monzonite. Quartz-monzonite intrusions are discordant small dykes and stocks that are weakly to highly deformed. On the Property, these intrusions are locally elongated subparallel to the east-west structural trend, and comprise equigranular and porphyritic subtypes. Equigranular intrusions show a medium-grained whitish matrix, whereas porphyritic ones have a fine-grained pinkish to reddish matrix and millimetric phenocrystic feldspar laths (20-30%) (Fig. 8E).The variability in mineralogical composition and textures likely represents multiple intrusive phases. Given the felsic nature, structural setting, porphyritic texture and relative timing of emplacement, these intrusions are likely associated with the syenite dyke reported in the Lanaudière Formation by Goutier and Lacroix (1992) or more precisely in the Shaft sector by Legault *et al.* (2005).

Polymictic conglomerate of the Duparquet Formation is also present in the northern part of the DOP (Fig. 4). It is locally moderately strained, iron-carbonatized, and composed of rounded clasts of mafic to felsic volcanic rock, quartz-feldspar porphyry, granite and jaspillite fragments (Fig. 8F).

1.5.1.2 Geochemistry

Twenty-six samples (twelve basaltic and andesitic rocks, five komatiites, five rhyolites, two quartz-feldspar porphyries and two quartz-monzonites) were selected from the DOP for geochemical characterization of the variably altered volcanic rocks hosting mineralization, and of least-altered rocks distal from the mineralized zones. Three average samples group of the Lanaudière Formation (Unit 1: Basalte, rhyolite and Komatiite) from Goutier and Lacroix (1992) were selected from the Duparquet area for comparison. Four average samples groups (fresh syenite, syenite-hematite alteration, syenite-iron carbonate alteration, syenite-sericite alteration) from the Beattie syenite (Bigot and Jébrak, 2015) are

reported in the geochemical diagrams for comparison with the DOP felsic intrusions. The major and trace elements lithogeochemical data are reported in Table 1. The qualitative group names attributed to the data in the geochemical diagrams, such as «Felsic volcanic rock», are proposed to simplify the presentation and were established by petrographic observations.

Ultramafic volcanic rocks plot in the sulbalkaline basalt field and alkaline basalt field in the Nb/Y versus SiO_2 diagram (Fig. 9A). A depletion of SiO_2 by alteration processes may explain the slight geochemical difference between the DOP altered ultramafic rocks and the komatiite group sample reported by Goutier and Lacroix (1992). Moreover, ultramafic volcanic rocks have a komatiitic composition in the Al versus Mg versus $Fe_{(T)}$ + Ti diagram (Fig. 9B) and a tholeiitic affinity (Fig. 9C). Two trends can be identified in the mafic and intermediate volcanic rocks. The first trend plot in the sub-alkaline basalt field (Fig. 9A) and the Fe-rich tholeiitic basalt field (Fig. 9B), and display a tholeiitic affinity (Fig. 9C). The second trend plot in the sub-alkaline field (Fig. 9A) and plot broadly from the tholeiitic basalt and dacite fields to the calc-alkaline basalt fields(Fig. 9B). This trend displays a calc-alkaline affinity (Fig. 9C). The first and second trends are interpreted as Fe-rich tholeiitic basalts and calc-alkaline basalts and andesites, respectively. Altered felsic volcanic rocks plot in the rhyolite field (Fig. 9A). Silicification is observed in thin-section and explains the rich SiO_2 content (> 80% SiO_2). Rhyolites have a transitional to calc-alkaline affinity (Fig. 9B, C).

Quartz-feldspar porphyries are of rhyodacitic composition in the Nb/Y versus SiO_2 diagram (Fig. 9A) and plot in the granodiorite field in the R1 versus R2 diagram (Fig. 9D). The quartz-monzonite of the DOP plot in the rhyodacitic field in the Nb/Y versus SiO_2 diagram (Fig. 9A) and in the quartz-syenite and quartz-monzonite fields in the R1 versus R2 diagram (Fig. 9D). As for the Beattie

syenite, it differs from the DOP quartz-monzonite intrusion by plotting in the trachy-andesite and trachyte field (Fig. 9A) and in the syenite and syeno-diorite fields (Fig. 9D).

The rare earth element (REE) pattern are presented for all samples of varying alteration assemblages and intensity to further discriminate lithological units of the DOP (Fig. 10A, B). Komatiites REE pattern show a depleted flat patterns, with chondrite-normalized La and Lu values not exceeding 2.5 and 1.5, respectively (Fig. 10A). Mafic and intermediate volcanic rocks are enriched relative to komatiite, with some samples showing slight enrichment in light REE. These mafic to intermediate rocks displays two trends in the REE pattern, as ndesite samples display and enrichment in light REE compared to the basalt samples. The REE profiles of felsic volcanic rocks (Fig. 9A) show overall enrichment relative to the other volcanic rocks. The rhyolites heavy REE are enriched relative to middle and light REE, and the REE pattern shows a negative Eu anomaly indicating plagioclase fractionation (e.g. Taylor *et al.*, 1981).

Quartz-feldspar porphyries have fractionated REE patterns and an enrichment of heavy REE relative to the light REE. The quartz-feldspar porphyry shares a similar REE pattern with the quartz-monzonite, but show lower REE abundances (Fig. 10B). The Beattie syenite REE pattern is similar to the DOP quartz-monzonite intrusions, but show overall enrichment (Fig. 10B). This limited comparison between the Beattie syenite and the DOP quartz-monzonite shows differences in geochemical classification but similitudes in REE patterns. The REE pattern of these intrusions is comparable to the REE pattern of the Shaft sector syenite in Legault *et al.* (2005), which suggest that the quartz-monzonite of this study likely belong to a broad, multiphase family of alkaline intrusions in the DOP sector, similar to the monzonitic to syenitic porphyry intrusions group reported by Robert (2001). Furthermore, the similarity

between the syenite of the DOP and the Beattie sector may suggest they were derived from the same plutonic event, and probably derive from the same parental magma during the Timiskaming event.

1.5.2 Hydrothermal alteration

On the DOP, hydrothermal alteration is extensive, diverse, and commonly restricted to the PDFZ and second-order shear zone. The nature, distribution and intensity of hydrothermal alteration are hereby characterized in an effort to define the major alteration and mineralization events. The nature of alteration is presented here as a mineral-based description of diagnostic mineral assemblages and alteration textures. The distribution refers to the mappable extent of the alteration types and its relationship to structures, mineralized rocks and other alteration types. The alteration intensity is estimated qualitatively (i.e. subtle, weak, moderate, strong and intense) based on the classification provided by Gifkins *et al.* (2005). With regard to the spatial relationship with gold mineralization, two alteration types are distinguished on the DOP, metamorphic assemblages and mineralization-related assemblages.

1.5.2.1 Metamorphic assemblages

Pre-ore greenschist facies metamorphic assemblages are preserved outside the PDFZ and second-order shear zones. Main minerals in basaltic rocks consist of subhedral plagioclase and pyroxene phenocryst, with minor amounts of disseminated magnetite and titanite, and a groundmass of feldspar and quartz. There is a strong chlorite and actinolite alteration and minor carbonatization (calcite) and epidotization (Fig. 11A).

1.5.2.2 Hydrothermal mineral assemblages

Hydrothermal alterations associated with gold mineralization consist of two distinct mineral assemblages which replaces regional metamorphic

assemblages. The most prominent alteration on the DOP consists of a pervasive carbonate-quartz-sericite assemblage, which is documented at the Liz and Shaft zones (Fig. 4). This assemblage includes variable proportions of millimetric anhedral to euhedral, calcic to ferroan carbonate, microcrystalline quartz and disseminated seams of millimetric anhedral sericite marking foliation (Fig. 11B, C). When exposed at surface and subsequently weathered, this alteration displays a distinctive orange colour. Variably deformed centimetric quartz and carbonate veins are common with this alteration assemblage. Locally, a few laminated quartz-and carbonate veins are preserved from deformation (Fig. 11D). Accessory minerals include hematite, Ti-bearing oxydes and fuschite. Relict metamorphic chlorite is commonly preserved in schist derived from basaltic and andesitic protolith, but its abundance decreases with increasing intensity of alteration. Hematite locally occurs as fine dusting, veinlets and disseminated grains in the vicinity of second-order shear zone (Fig. 7). Fuchsite and chromite occurs in ultramafic rocks as milimetric seams and disseminated grains, respectively, along with talc and serpentine as a selective replacement of relic olivine and pyroxene crystals.

The second type of mineralization-related alteration is characterized as a pervasive quartz-calcite-hematite assemblage and is documented at the Fox zone (Fig. 4). It consists either of an undeformed to moderately deformed stockwork of calcite and quartz veinlets, patchy hematite dust (<10%) and local seams of fine-grained sericite (Fig. 11E), or a massive quartz replacement with minor patchy hematite dust, with disseminated or clustered pyrite grains (Fig. 11F). Relict igneous or metamorphic minerals are also variably preserved in mafic to ultramafic protolith, such as disseminated millimetric grains of magnetite and chromite (<5%) or patchy chlorite. Their abundance decreases with increasing intensity of alteration. Microcrystalline quartz and carbonate

veins displaying open-space crystallization and and corrosion have also been documented (Fig. 11G). Massive quartz replacement and disseminated pyrite (5-10%) has also been documented in the Fox zone by Legault et al., (2005) and interpreted as a residue of moderately to strongly leached wall-rock based on mass-balance calculation indicating mass losses in all major elements.

1.5.2.3 Distribution of alteration assemblage

The mineralization-related alteration assemblages have different distributions on the DOP. Pervasive carbonate-quartz-sericite wall-rock alteration characterizes second-order shear zones and extends for as much as 20m into areas of unstrained rocks, defining a broad zonation surrounding gold mineralization (Fig. 12). At the South trenches (Fig. 4), which expose the northern part of the PDFZ, no sericitization was observed and a strong carbonatization along with minor quartz veins extends for as much as 50m outward of the strained rocks. At the studied Shaft trenches, the alteration sequence consists of three zones, the distal calcite-chlorite-quartz, the transitional calcite-ferroan carbonate-chlorite-quartz and the proximal ferroan carbonate-sericite-quartz zones. The complete alteration sequence associated with second-order shear zones can be as wide as 30m (Fig. 7). The distal zones reflect partial replacement of regional metamorphism alteration minerals such as actinolite and epidote by the calcite-chlorite-quartz assemblage (Fig. 12). Gold concentrations in the distal zones rarely grade higher than 30 ppb. The transitional zones reflect the gradual replacement of distal calcite and chlorite by ferroan carbonate (ferroan dolomite or ankerite) and minor sericite toward the proximal alteration zone (Fig. 12). Gold grades associated with this zone generally occur between 35 and 1000 ppb. Areas of proximal and the most intense alteration is the result of sericitization, iron-carbonatization and silicification replacing chlorite and calcite, the relatively abundant disseminated

pyrite, and intense deformation (Fig. 12). Gold grades (~1 to 10 ppm) are at their highest in this zone compared to the transitional and distal zones.

With exception of the constant strong carbonatization, the intensity of sericitization and silicification is heterogeneous within the proximal zone from moderate to strong. The maximal alteration intensity is observed in high-strain contact between less competent mafic and ultramafic units and competent quartz-feldspar porphyry (Fig.11G, H). The carbonate-quartz-sericite assemblage alteration is most prominent in mafic and ultramafic rocks but also overprints, to a lesser degree, felsic rocks. As for the quartz-calcite-hematite assemblage of the Fox zone, it has been documented in highly strained mafic and ultramafic units in contact with the North Porphyry stock (Fig. 5). The chronological relationship between the two types of mineralization-related alteration has not been established, but their respective overprint on quartz-feldspar porphyritic intrusions in second-order shear zones give a broad post-QFP crystallization at 2689 ± 3Ma.

1.5.3 Alteration geochemistry

1.5.3.1 Single precursor mass transfer calculation

It is evident by the alteration paragenetic sequence that significant changes in the chemical composition of the host rocks occurred during alteration. Therefore, mass balance calclutations (Grant, 1986) is an effective method to quantitatively define elements that were mobilized and to underline the signature of the geochemical dispersion surrounding the hydrothermal mineralization (Eilu *et al.*, 2001). At the DOP, mass transfer calculations were performed separately on seven altered samples related to mineralization on the Shaft (n=3) and Liz (n=4) zones. No mass-balance calculations were performed on the Fox zone mineralized samples, as this study lacked adequate

representative of the least-altered protolith. The protoliths and altered sample are paired as tholeiitic basalt, calc-alkcaline basalt-andesite or transitional rhyolite. A summary of the results are discussed below and sumarized in Fig. 13. Caution is necessary when analysing the histogram in Fig. 13 as it is dependant of the effect of analytical error on the enrichment factor. The mass balance calculations are based on the immobility of aluminium and zirconium. The immobility of aluminium and zirconium is indicated by the coherent trends shown in the TiO_2 versus Zr, Al_2O_3 versus Zr and Al_2O_3 versus TiO_2 (Figure 1; Annexe B). The parameters of the mass balance calculations (Table 1; Annexe B) the isochon diagrams for each calculations are summarized (Figure 2; Annexe B). In order to simplify the presentation of figure 13, the «Enrichment factor» represents the mass-balance calculation results (in %) divided by 100. The enrichment factor for Au is not presented in Fig. 13 as all samples are enriched.

Enrichment factors show that some major (Fig. 13A) and trace elements (Fig. 13B) are mobile in the alteration. Overall enrichment in most of the samples includes MnO, K_2O, Mo, W and Sb whereas leaching in most of the samples is limited to Sn. Although all samples studied belong to the mineralization-related Dol-Ser-Qtz alteration assemblage, notable differences in gains and losses occur between the Shaft and Liz zones, such is the case for Fe_2O_3(T) MgO, CaO, Na_2O, P_2O_5, Cu and Ni. Moreover, enrichments for the Shaft zone are heterogeneous. For example, the 30960 sample presents anomalous gains relative to the two other Shaft samples, including Fe_2O_3 T, MnO, Na_2O, TiO_2, Co, Zn and Pb. The anomalous chemistry of the 30960 sample can be explained by its brecciated texture (Fig. 11C), as dark-colored fragments potentially rich in Fe_2O_3(T), MnO, TiO_2, Co, Zn and Pb are encompassed in a light-grey matrix reflecting the overall rhyolitic composition of the sample. As for the more homogenous Liz zone distribution, all samples exhibit enrichment in K_2O, Ni, As,

Mo, W, Sb and Ba, and leaching of CaO, P_2O_5, Zn and Sn. Although no chemical analysis was undergone for S and CO_2, both zones show enrichments in CO_2 and S due to carbonatization and pyritization, respectively.

1.5.3.2 Sericite saturation alteration index

A number of empirical alteration indices have been proposed to underline alteration intensities related to mineralogical changes and to define pathfinders to lode-gold mineralizations (Kishida and Kerrich, 1987; Eilu et al., 2001). As sericitization commonly correlates with mineralization on the DOP, the usage of the sericite saturation alteration index (Kishida and Kerrich, 1987) may present a simple tool for further gold exploration. As presented in Fig. 13C, most of mineralized samples occurred in the alteration zone associated with alkali leaching. However, further analysis is necessary to establish a statistically representative correlation.

1.5.4 Gold mineralization

Gold mineralized zones on the DOP consists of the Liz, Shaft (including North and South Shaft), Fox, Stinger, Nip (including Nip-North and Nip-South) and the 20-20 zones (Power-Fardy and Breede, 2011). The main mineralized zones (Shaft, Liz, Fox, Nip and 20-20) are hosted mainly by tholeiitic basalt and komatiite, in highly altered, discontinuous metric zones centered on second-order shear zones (Fig. 7) and at high-strained contacts between felsic and mafic-ultramafic rocks (Fig. 11H).The Fox and 20-20 zones are located at the contact between deformed mafic to ultramafic rocks and the North Porphyry, whereas the Stinger zone is located in mineralized brittle fractures within the North Porphyry (Fig. 4). Minor fracture-filling epithermal veins occur in the vicinity of the North Porphyry, at the Fox, Stinger and 20-20 zones.

1.5.4.1 Typology of mineralized zones

On a descriptive basis, mineralized occurrences of the DOP are characterized by three distinct types (Table 2): (1) *disseminated sulphides*, (2) *clusters of sulphides and iron* oxides and, (3) *epithermal veins*. Disseminated sulphides, mostly represented by pyrite, are common on the DOP, and occur in all mineralized zone. However, alteration, ore mineralogy, as well as elemental associations are dissimilar depending on the type of mineralized occurrence. The Shaft and Liz zones display features associated with disseminated sulphides, whereas the Fox zone comprises clusters of sulphides and iron oxides and has minor occurrences of epithermal veins. Epithermal veins have also been observed in the Stinger and 20-20 zones (Power-Fardy and Breede, 2011).

The *disseminated sulphides* type is structurally-controlled, occurring as lenses in the foliated and altered wall-rock of second-order shear zones. Although no exclusive lithology hosts mineralized zones, basaltic, komatiitic and andesitic rocks are the most recurrent hosts. Ore minerals consist mainly of anhedral to euhedral pyrite (G2 to G6) and minor anhedral chalcopyrite finely disseminated in a moderate to strong ferroan carbonate-sericite-quartz altered foliation (Fig. 15A, B). There are also traces of Au-Ag-Hg tellurides (Fig. F, G) and anhedral Cu-Sb-As sulphosalts (Fig. 15H).The sulphide content varies from 5% to 10%. Gold particles are very fine-grained (3 to 5 μm), are located at grain boundaries of pyrite and silicate gangue minerals, and gold grades generally correlate with greater pyrite abundance. Gold occurs mainly as native gold, alongside limited amounts of electrum. The alteration assemblage, the ore mineralogy and mass-balance calculations reflect a main input of CO_2, K_2O, S, Mo, W, Sb, As, Au and minor input in Te, Ag, Hg and Ba, and a loss in Sn. Liz and Shaft zones grade up to 10 g/t Au, with average values of 4.5 g/t Au, and disparate high grade zones above 10 g/t Au (Power-Fardy and Breede, 2011). Anomalous

gold grades of 0.5 to 1 ppm occur outside second-order shear zones and are associated with minor east-west trending shear zones cutting all rocks types (Fig. 7).

The *clusters of sulphides and iron oxides* type occurs in high-strained zones of mafic to ultramafic rocks bounding the southern contact of the North Porphyry. This mineralization type is associated with a strong quartz-calcite-hematite alteration (Fig. 16A, B). Ore minerals consist of disseminated millimetric clusters of mainly anhedral pyrite (5-10%), chalcopyrite (1%), hematite and magnetite (Fig. 16C). There are also trace occurrences of galena, bismuth- and cobalt-bearing minerals (Fig. 16C, D), and Au-Ag-Hg-Bi tellurides (Fig. 16E). As the host rock is a mafic to ultramafic rock, the origin of the euhedral magnetite is interpreted as primary magmatic. Hematite is present as fine dust and clusters overprinting euhedral magnetite and anhedral pyrite. Gold particles are very fine-grained (3 to 4.5μm) and are mostly located at grain boundaries of pyrite and silicate gangue minerals. Gold occurs mainly as native gold, with minor occurrences of electrum and Au-Ag tellurides. The alteration assemblage and ore mineralogy reflect a main hydrothermal input of SiO_2, CO_2, S, Cu, Au, Ag and Te and a minor input in Pb, Zn, Bi and Co. The Fox zone grade up to 10 g/t Au, with average values of 3.5 g/t Au (Power-Fardy and Breede, 2011).

The *epithermal veins* (Fig. 16 G) occur as disparate, millimetric to centimetric microcrystalline quartz and carbonate veinlets filling fractures in the North Porphyry, at some locations displaying open spaces crystallization textures such as crustiform and comb textures. This terminology is chosen to reflect the similitude between the DOP veins and the epithermal vein type suggested in Legault *et al.* (2005). The veins were deformed by the D_2 deformation event. Fragments of microcrystalline quartz veins are reported by Legault *et al.* (2005) to have been found at the base of the Timiskaming

conglomerates, suggesting, at least partly, a synchronicity with opening of the basin and relative Timiskaming sedimentation. Ore minerals consist of chalcopyrite, pyrite, galena, sphalerite, tourmaline, tennatite-tetrahedrite and Au-Ag tellurides (Fig. 16G). Gold occurs as native gold and Au-Ag telluride. There are also locally a large number of very coarse Ag-telluride grains. Chalcopyrite, sphalerite and molybdenite in epithermal veins are reported in the East Stinger Zone and the zone displays at depth increased base metal and silver grades (Power-Fardy and Breede, 2011). This type of mineralization is not included in our geochemical study.

This type of mineralization is analogous to the epithermal vein type of Legault *et* al. (2005) which is characterized as microcrystalline quartz or chalcedony veins with open spaces crystallization textures, local spectacular gold content (149 g/t Au over 3.0m at the Nipissing showing; Legault *et* al., 2005), anomalous enrichments in Zn, Pb and Hg (±Cu) and Mo-Bi, .

1.5.4.2 Mineralogy and paragenesis

The paragenetic sequence of the main mineralization type of the Shaft and Liz zones, the *disseminated sulphides type,* is composed of five stages (Fig. 14): (1) Pre-ore metamorphic stage, (2) hematite stage, (3) sulfide stage, (4) cataclasis and remobilisation stage, and (5) weathering. The mineral paragenesis illustrates the progression in time from pre-ore, volcanic and metamorphic assemblages, to hydrothermal input to cataclasis and remobilisation to weathering. As much as six generations of pyrite (G1-G6) are distinguished on textural and compositional basis. G1 is an early pre-ore stage pyrite found in the least-altered rocks, whereas G2 to G6 are intimately related to gold mineralization. The composition of these gold-related pyrites is described in the next section.

The *pre-ore metamorphic stage* is related to the least-altered, metamorphosed primary mafic volcanic host rocks. It consists of subhedral magnetite associated with anhedral titanite and minor pyrite. Pyrite of this stage (G1) consists of disseminated rounded and fractured centimetric clusters (Fig. 15C). Trace occurences of anhedral porous apatite are also present.

The *hematite stage* consists of martite and hematite. The former occurs as partial to complete pseudomorphic replacement of magnetite by hematite (Fig.15D); the latter as a fine dust and needles disseminated in the groundmass. Also, leucoxene is widespread and results of the complete alteration of titaniferous mineral. Leucoxene generally appears as disseminated grains and dust.

The *sulphide stage* defines the main phases of sulphidation and gold mineralization. Subhedral to euhedral (pyritohedron) pyrite (0.1-0.5 mm) is disseminated in the altered rock (<10%), and aligned according to the main schistosity. Pyrite is the main ore mineral, consisting of more than 90% of all metallic minerals. As many as five generations of pyrite are recognized in a single grain (Fig.15E), but two to three generations are the most recurrent. The first generation of hydrothermal pyrite (G2) is porous and filled with quartz, chalcopyrite, gold and tellurides inclusion. The following generations of pyrite (G3 to G6), which generally overgrows on the G2 pyrite, are recognized by their nonporous to slightly porous surface and distinct boundaries. Anhedral chalcopyrite, which consists of 5% of the metallic minerals, is present as fine inclusions (Fig. 15G, H), along with trace amounts of fine irregular-shaped Au-Ag tellurides, enargite and tetrahedrite-tennantite inclusions in pyrite (Fig. 15G, H). This stage is associated with the iron carbonate, sericite and quartz alteration.

The *cataclasis and remobilisation stage* consists of the brecciation of sulphides along deformation corridors. All generations of pyrite (G1- G6) are

present, but have undergone brecciation and present irregular shapes. The brittle deformation is heterogeneous, as strongly deformed sulphides corridors contrast with less to undeformed grains. The remobilisation consists of metallic mineral such as chalcopyrite (Fig. 15I), native gold, Au-Ag tellurides and electrum (Fig 15J) occuring in the microfractures, at the boundaries and in the porosity of brecciated pyrite grains as well as intergrown with silicate gangue minerals in the matrix.

A late *weathering* event led to goethite crystallization as coronitic to pseudomorphic textures around sulphide and iron-rich minerals.

1.5.4.3 Pyrite element mapping

Pyrite is the primary sulphide on the property and it is spatially related to gold mineralization. In an attempt to trace the sulphidation history and a geochemical signature for gold, LA-ICP-MS mapping was realized on 9 pyrite samples from the Liz (n=3), Shaft (n=3) and Fox zones (n=3) (Table 1; Annexe C). The following section presents and discuss the results of element mapping of an anhedral pyrite mass (Fig. 17) and a subhedral pyrite grain sampled from the *disseminated sulphides type* of the Liz zone (Figure 1; Annexe C).

As the pyrite grains are optically heterogeneous, displaying a porous core (G2) and a cleaner outer rim (G3), elemental mapping reveals nonuniform distribution of many elements. Au, Ag, and Te are restricted to the earliest growths stage, in the core of the crystal. Mo and Se are slightly concentrated in all areas of the pyrite. Although present throughout the crystal, enrichment of Cu, Pb and Co appears in the core of the pyrite. As, Co and Ni are enriched in the pyrite core, which is enveloped by a slightly depleted zone and then an enriched outer rim. The thin outer rim enrichment of As, Co and Ni characterizes the latest pyrite growth phase. Bi, Zn and W are concentrated outside the pyrite,

whereas Ti appears slightly concentrated in the G2 core and outside the pyrite. These results underline the geochemical relationship between gold, silver and tellurides, and the early G2 pyrite growth phase.

1.5.4.4 Preliminary stable-isotope geochemistry

The sulphur stable isotope data are reported in Fig. 18A. The $\delta^{34}S$ values for numerous generations of hydrothermal pyrite grains show significant variation from -12.7 to -0.6 ± 0.2‰ (n=6, average = -7.4‰ ± 0.2‰). The $\delta^{34}S$ values for magmatic pyrite from quartz-feldspar porphyries are identical at 0.6 ± 0.2‰ (n=2). In relation to the three mineralized zones, the S composition of pyrite is remarkably heterogeneous; pyrite from the proximal alteration of the Liz zone shows the lowest negative $\delta^{34}S$ values ranging from -12.7 to -11.6 ± 0.2‰, followed by the pyrite of the Shaft zone from -6.9 to -6.2± 0.2‰, and contrasting with the Fox zone at –0.6 ± 0.2‰. Finally, pyrite values from a pollymetallic vein within a filled fracture of QFP shows values of -6.5± 0.2‰. These limited data indicate a trend toward lower $\delta^{34}S$ values of pyrite toward the southern Liz zone.

1.6 Discussion

1.6.1 Proposed metallogenic evolution

The chronology of the geologic events occurring in the Duparquet area is summarized in Figure 3. This local overview provides a geological context for the DOP mineralization, as discussed in the section below.

The DOP hosts multiple deformed and metamorphosed rock types. The felsic to ultramafic volcanic rocks, quartz-feldspar porphyry, quartz-monzonite, alkaline intrusions and clastic sedimentary rocks described previously are petrographically and geochemically strongly similar to the Lanaudière Formation, calc-alkaline and alkaline porphyritic intrusions and to the Duparquet Formation respectively, as defined by Goutier and Lacroix (1992).

In terms of structural features, the DOP is characterized by the first-order PDFZ to the south, and multiple east-trending, steeply dipping to the south, second order shear zones overprinting all rock types. Field observations exhibit evidences of reverse dextral sense of shear. The occurrence of weakly to highly deformed quartz-feldspar porphyry and alkaline intrusions in these shear zones suggest a syntectonic origin likely associated with a local extensive event prior to the regional compressive deformation events D_2. As conglomerates of the Duparquet Formation uncomfortably overly the calc-alkaline to alkaline porphyric intrusions, these intrusions were therefore emplace prior to sedimentary basin opening.

Paleostress fields modeling, based on the geometry of the PDFZ in the Duparquet area (Faure and Rafini, 2009), provides insights on the relationship between structural kinematics and gold deposit distribution. Effectively, as fluids migrate from high- to low-stress zones in the crust, this modeling illustrates the close spatial link between low paleostress areas, hydrothermal alteration fields resulting from fluid migration, and localization of gold deposits near or within such field, such is the case for the Beattie gold deposit, Yvan-Vézina and Duquesne past-producing mines and the DOP prospect.

Detailed trench mapping and core logging on the property indicate that mineralized zones and associated alteration are hosted by (1) second-order shear zones and altered wall-rock (Liz and Shaft zones), (2) within the high-strain zone marking the contact between the North Porphyry and the volcanic rocks of the Lanaudière Formation (Fox and 20-20 zones) and (3) as fracture-filling within the North Porphyry (Fox and Stinger zone).

Several lines of evidence indicate that the DOP mineralized zones are the product of at least two distinct hydrothermal events. This is highlighted by the significant differences between the Shaft and Liz zones, and the Fox zone (Table

2). The former zones are characterized by ferroan carbonate-quartz-sericite alteration assemblage, which contrasts with the quartz-calcite-hematite assemblage of the latter zone in terms of ore mineralogy, textures, geochemical signature and metallic association (Table 2).

In the Fox zone case, the iron oxide-rich ore mineralogy along with negative isotopic sulphur compositions for ore-stage pyrite reflects a relatively high fO_2 environment. The massive quartz replacement and the corrosive texture of some veins (Fig. 11F, G) may indicate the presence of leaching and acidic fluids. The ore mineralogy associated with this zone indicates anomalous Cu-Au-Ag-As-Te ± Pb-Zn-Co-Bi-W-Sn hydrothermal enrichment, which is comparable to the epithermal vein type documented by Legault *et al.* (2005). The possible felsic subvolcanic explosive breccia observed at the 20-20 trench may indicate shallow crustal level. These observations indicate an oxidized, acid, surficial character for the Fox zone, which is reminiscent of an epithermal system.

Although speculative, the epithermal character of the Fox, Stinger and 20-20 zones may be related to the alkaline intrusions of the DOP, as it shares a close temporal and spatial relationship. Although volumetrically minor, hence potentially insufficient to generate the thermal requirement for an epithermal system, there may be a larger not yet found alkaline intrusion located at greater depth near the Fox, 20-20 and Stinger zones. The distinctive circular magnetic positive anomaly found immediately north-east of the Shaft zone could indicate the presence of such an intrusion (Lambert, 2001).

In the Shaft and Liz zones case, the primary control on gold mineralization is structural, as second-order shear zones host the disseminated sulphides style of mineralization and associate alteration. These shear zones are associated with the second major deformation event (D_2-D_3). Mineralization is

mostly, but not exclusively, concentrated in Fe-rich tholeiites. The iron oxide-poor and pyrite-rich mineralization reflects a relatively reductive environment. K_20 gains in the form of sericite alteration likely represent either an external input or local remobilisation of potassium from the metasomatism of surrounding alkaline intrusions. Ore paragenesis and elemental map of pyrite reflects a multistage evolution of pyrite and gold, which is discussed below. These features shares strong similarities with the mesozonal to epizonal transition of orogenic gold deposits (Gebre-Mariam *et al.*, 1995; Groves *et al.*, 1998). The spatial correlation of mineralization with QFP on the property is inferred to be the results of a favorable competency contrast between the competent QFP and the less competent mafic to ultramafic volcanic rocks. This interpretation is consistent with preferential fracturing and alteration of the volcanic rocks relative to the QFP, as highlighted by the alteration intensity distribution mapping on the East-Shaft trenches (e.g. Fig. 11 H).

In the context of an orogenic gold deposit, sulphides and gold are intimately related. In the DOP, there is a bimodal distribution of gold. The first concentration consists of minor submicroscopic gold enrichment, hereby termed invisible, mapped in the G2 pyrite and associated with silver and tellurium. The LA-ICP-MS mapping cannot determine whether invisible gold occurs as lattice-bound in the pyrite structure, or is present as microinclusions (less than 0.1 μm) in the porosity of the pyrite as demonstrated by Deditius *et al.* (2009). The second type of gold concentration consists of microscopic native gold, electrum and Au/Ag telluride grains (3-5μm) spatially associated with pyrite (G2-G6), sericite and ferroan carbonate. At least two main scenarios could explain the morphology and spatial distribution of gold grains: (1) a hydrothermal phase could have initially introduced invisible gold in the G2 pyrite structure, from which it was subsequently remobilized and deposited as inclusion and in late

fractures in pyrite as a result of brecciation and fluid circulation, as documented by Morey *et al.* (2008) and Cook *et al.* (2009); or (2) syn-D_2 gold was introduced following corrosion of G2 pyrite, and precipitated in residual porosity and fractures. Further scrutiny on this process and the G2 pyrite is required to discern and improve this model.

1.6.2 Comparison with other gold deposits

The DOP Shaft and Liz zones share analogies with other orogenic gold deposits in the Archean Abitibi greenstone belt. The Fox zone shares several features with high-sulphidation epithermal deposits although none have been described in the Abitibi. In order to establish a reasonable comparison, Table 3 enumerates numerous features associated with a high-sulphidation epithermal model and multiple specific cases of orogenic gold deposits hosted by greenschist grade rocks, and associated with the Porcupine-Destor and Larder Lake-Cadillac fault zones (Fig. 1).

Albeit comparable to the Holloway and Sigma deposits, the DOP Shaft and Liz zones resemble most the Hollinger-McIntyre, Beattie and Malartic epigenetic gold deposits because of comparable: (1) spatial association with calc-alkaline and alkaline porphyritic rocks; (2) brittle-ductile structural regime; (3) main replacement style alteration assemblage comprising mostly iron carbonate, sericite and silica; (4) gold mineralization mostly disseminated in strongly foliated rocks; (5) ore mineralogy mainly composed of pyrite; and (6) elemental association indicating similar Ag, Mo, W, Pb, Cu, As, and Te input. Moreover, as illustrated on Fig. 18B, the DOP shares similar negative isotopic composition of sulphides with deposits associated with alkaline magmatism and generally oxidized conditions, such as Thunder Creek (Campbell, 2014), Highway 144 (Campbell, 2014), Canadian Arrow (Schwarcz and Rees, 1986), Beattie (Xue *et al.*, 2013; Bigot and Jébrak, 2015) and Macassa (Cameron and Hattori, 1987)

gold deposits. The Shaft and Liz zones differ from the Holloway and Sigma in terms of main alteration assemblage and structural features. The Holloway deposit Lightning zone sits at the ductile contact between ultramafic flows and tholeiitic and pillowed flows (Luinstra, 2004). The Sigma-Lamaque deposit is renowned as a classical fault-filled and extensional flat vein-hosted orogenic gold deposit. The DOP Fox zone shares a few similarities with high-sulphidation epithermal deposit such as (1) silica alteration (leaching); (2) ore mineralogy composed of pyrite, chalcopyrite and iron oxides; and (3) a similar Au, Ag, As, Cu, Sb, Pb, Sn, and Te metallic association . The Beattie deposit shares the strongest analogies with the gold occurrences of DOP as both have similar spatial relationship with alkaline magmatism and brittle-ductile second-order shear zone, relative timing of mineralization, alteration assemblages, disseminated sulphides, ore mineralogy, metallic association and low sulphur isotopic values for pyrite.

A metallogenic overview of the Duparquet area (Legault *et al.*, 2005) has distinguished three main periods of gold deposition and five main types of gold mineralization: (1) synvolcanic, VMS and neutral epithermal gold mineralization; (2) syntectonic D_2, syn-Timiskaming event, acid epithermal and syenite-associated disseminated gold deposits; (3) syntectonic D_2, post-Timiskaming event, quartz-carbonate veins and disseminated orogenic gold deposits. In this framework, the DOP may present the surimposition of two distinct periods of gold mineralization, an early syn-Timiskaming epithermal mineralization overprinted by an epizonal to mesozonal orogenic gold deposit. Therefore, the less-deformed Fox zone may represent preserved remnants of an epithermal system that was completely destroyed by the D_2 event, which developed the increasingly-deformed Liz and Shaft zones. Based on the pre-enriched G2 pyrite (Au, Ag, Te) which contrast with the later generations of

depleted pyrite, the Shaft and Liz zones, albeit mainly associated with the main post-Timiskaming, D_2 event, may have an early distinctive phase. The nature of such phase remains unclear.

As a syn-magmatic phase was recognized at the Beattie deposit (Bigot and Jébrak, 2015), the shared features in alkaline magmatism, structural setting, alteration, mineralization and geological evolution between the DOP and the Beattie deposit may underline a common syn-Timiskaming event magmatic-hydrothermal system. The distribution of such magmatic-hydrothermal system in the Duparquet area may extend from the Beattie deposit to the DOP and share a syn-Timiskaming event of gold mineralization. This local magmatic imprint at the scale of the Duparquet area along the PDFZ raises questions on the current uniform orogenic model (Groves *et al.*, 1998) as to why gold systems recognized along major crustal faults such as the Porcupine-Destor (Berger, 2001) and the Larder Lake-Cadillac faults (Raffini, 2014) present such heterogeneous metallogenic characteristics.

1.7 Conclusion

Two distinct hydrothermal events are distinguished on the DOP. Associated with the Fox zone, the first gold event is located at the high-strained contact between a large calc-alkaline porphyry stock and the volcanic rocks of the Lanaudière Formation. The Fox zone is characterized with quartz-calcite-hematite alteration, with ore mineral consisting of pyrite, hematite and chalcopyrite, and with minor epithermal veining. Visible gold occurs as inclusions and filling microfractures in pyrite. The alteration assemblage and ore mineralogy reflect a main hydrothermal input of Au, SiO_2, CO_2, S, Cu and a minor input in Ag, Te, Pb, Zn, Bi and Co. This Fox zone mineralization is reminiscent of an epithermal type mineralization, possibly associated with alkaline intrusion. The second hydrothermal gold event, located in the Shaft and Liz zones, is

hosted in east-west trending second-order shear zones overprinting all rock types and associated with a ferroan carbonate- quartz-sericite alteration assemblage. Ore assemblage consists principally of pyrite with minor chalcopyrite, and traces of tellurides and sulphosalts. Mass-balance calculations and alteration mineralogy reflect notable gains in CO_2, K_2O, S, Mo, W, Sb, As, Au and minor input in Te, Ag, Hg and Ba, and a loss in Sn. Ore paragenesis reflects a multistage evolution of sulphides and gold. Most pyrites in these zones have first generation porous core and multiple overgrowths. They display distinct geochemical zonation and a core enriched in Au, Ag and Te. There is a negative $\delta^{34}S$ isotopic composition of pyrites across the property, ranging from -12.7 to -0.6 ± 0.2 ‰. Overprinting relationships show a relative age for gold deposition as postdating QFP crystallization at 2689 ± 3 Ma, and occurring mostly during syn-D_2 post-Timiskaming event. The nature of these two distinct hydrothermal events may be explained by an early epithermal mineralization overprinted by an epizonal to mesozonal orogenic gold deposit. Many of the features of the DOP Liz and Shaft zones are similar to mesozonal Archean orogenic gold deposit found in the southern Abitibi greenstone belt, especially the Beattie gold deposit.

This study has provided a better understanding of the geology and metallogeny of the DOP. However, several aspects need to be clarified, such as the extent of each hydrothermal event at the scale of the property and the Duparquet area, the precise nature of hydrothermal fluids involved in each hydrothermal event, if invisible gold is lattice-bound in the porous G2 pyrite, the exact age of each gold deposition event and the possible genetic link between the DOP alkaline intrusions, epithermal and orogenic type of gold mineralization.

Acknowledgements

The authors thank Xmet Inc., NSERG, and FQRNT for funding this study, which is part of a M.Sc. undertaken at the Université du Québec à Montréal project by the first author (SL). We specially thank the staff of Xmet Inc. for their all-around help and thought-provoking discussions, particularly Pierre Riopel. Ludovic Bigot, Jean Goutier, Stéphane Faure, Noémie Fayol, Yannick Daoudene and Pierre Lacoste are acknowledged for their useful comments, which greatly improved the quality of this work. Stéphane De Souza and Jean Goutier are thanked for their constructive comments on the earlier version of the manuscript. We also thank Raynald Lapointe for the technical help and Michelle Laithier for the artwork.

Reference

Ayer, J., Amelin, Y., Corfu, F., Kamo, S., Ketchum, J., Kwok, K., & Trowell, N. (2002). Evolution of the southern Abitibi greenstone belt based on U–Pb geochronology: autochthonous volcanic construction followed by plutonism, regional deformation and sedimentation. Precambrian Research, 115(1), 63-95.

Ayer, J. A. and Ontario Geological Survey. (2005). Overview of results from the greenstone architecture project: discover Abitibi initiative. Ontario Geological Survey.

Bateman, R. and Bierlein, F. P. (2007). On Kalgoorlie (Australia), Timmins–Porcupine (Canada), and factors in intense gold mineralisation. Ore Geology Reviews, 32(1), p. 187-206.

Beaudoin, G., & Pitre, D. (2005). Stable isotope geochemistry of the Archean Val-d 'Or (Canada) orogenic gold vein field. Mineralium Deposita, 40(1), 59-75.

Beaudry, D. (1992). Analyse structurale des assemblages volcanosédimentaires au voisinage de la faille Porcupine-Destor, Abitibi, Québec. Chicoutimi: Université du Québec à Chicoutimi.

Bédard, J. H., Harris, L. B., & Thurston, P. C. (2013). The hunting of the snArc.Precambrian Research, 229, p. 20-48.

Benn, K., & Peschler, A. P. (2005). A detachment fold model for fault zones in the Late Archean Abitibi greenstone belt. Tectonophysics, 400(1), p. 85-104.

Berger, B. R. (2001). Variation in styles of gold mineralization along the Porcupine–Destor deformation zone in Ontario: an exploration guide. Ontario Geological Survey Open File Report, 6070, 9-1.

Bigot, L. and Jébrak, M. (2015). Gold Mineralization at the Syenite-Hosted Beattie Gold Deposit, Duparquet, Neoarchean Abitibi Belt, Canada. Economic Geology, 110(2), p.315-335.

Bleeker, W., & Parrish, R. R. (1996). Stratigraphy and U-Pb zircon geochronology of Kidd Creek: implications for the formation of giant volcanogenic massive sulphide deposits and the tectonic history of the Abitibi greenstone belt. Canadian Journal of Earth Sciences, 33(8), p. 1213-1231.

Bleeker, W. (2012). Targeted Geoscience Initiative 4. Lode gold deposits in ancient deformed and metamorphosed terranes: the role of extension in the formation of Timiskaming basins and large gold deposits, Abitibi greenstone belt—a discussion. Ontario Geological Survey, Summary of Field Work and Other Activities, 47-1.

Bleeker, W. (2015). Synorogenic gold mineralization in granite-greenstone terranes: the deep connection between extension, major faults, synorogenic clastic basins, magmatism, thrust inversion, and long-term preservation. Targeted Geoscience Initiative 4: Contributions to the Understanding of Precambrian Lode Gold Deposits and Implications for Exploration, Geological Survey of Canada, Open File 7852, p. 25–47.

Bourdeau, J. (2013). Petrology, Mineralogy and Geochemistry of the Beattie Syenite and Country Rocks, Abitibi Greenstone Belt, Québec. University of Ottawa, 440p.

Cameron, E. M., & Hattori, K. (1987). Archean gold mineralization and oxidized hydrothermal fluids. Economic Geology, 82(5), p. 1177-1191.

Campbell, R. A. (2014). Controls on Syenite-Hosted Gold Mineralization in the Western Timmins Camp. The University of Western Ontario, 159p.

Card, K. D. (1990). A review of the Superior Province of the Canadian Shield, a product of Archean accretion. Precambrian Research, 48(1), p. 99-156.

Chown, E. H., Daigneault, R., Mueller, W., & Mortensen, J. K. (1992). Tectonic evolution of the northern volcanic zone, Abitibi belt, Quebec. Canadian Journal of Earth Sciences, 29(10), p. 2211-2225.

Chown, E. H., Harrap, R., & Moukhsil, A. (2002). The role of granitic intrusions in the evolution of the Abitibi belt, Canada. Precambrian Research, 115(1), p. 291-310.

Colvine, A. C. (1988). Archean lode gold deposits in Ontario, Ontario Ministry of Northern Development and Mines, Vol. 139, 136 p.

Cook, N. J., Ciobanu, C. L., & Mao, J. (2009). Textural control on gold distribution in As-free pyrite from the Dongping, Huangtuliang and Hougou gold deposits, North China Craton (Hebei Province, China). Chemical Geology, 264(1), p. 101-121.

Corfu, F., Jackson, S. L., & Sutcliffe, R. H. (1991). U-Pb ages and tectonic significance of late Archean alkalic magmatism and nonmarine sedimentation: Timiskaming Group, southern Abitibi belt, Ontario. Canadian Journal of Earth Sciences, 28(4), p. 489-503.

Corfu, F. (1993). The evolution of the southern Abitibi greenstone belt in light of precise U-Pb geochronology. Economic Geology, 88(6), p. 1323-1340.

Couture, J. F., & Pilote, P. (1993). The geology and alteration patterns of a disseminated, shear zone-hosted mesothermal gold deposit; the Francoeur 3 Deposit, Rouyn-Noranda, Quebec. Economic geology, 88(6), p. 1664-1684.

Daigneault, R., Mueller, W. U., & Chown, E. H. (2002). Oblique Archean subduction: accretion and exhumation of an oceanic arc during dextral transpression, Southern Volcanic Zone, Abitibi Subprovince Canada.Precambrian Research, 115(1), p. 261-290.

Daigneault, R., Mueller, W. U., & Chown, E. H. (2004). Abitibi greenstone belt plate tectonics: the diachronous history of arc development, accretion and collision. The Precambrian Earth: Tempos and Events, Series: Developments in Precambrian geology, 12, 88-103.

David, J., Dion, C., Goutier, J., Roy, P., Bandyayera, D., Legault, M., & Rhéaume, P. (2006). Datations U-Pb effectuees dans la Sous-province de l'Abitibi a la suite des travaux de 2004-2005. Ressources naturelles et faune Québec. 22p.

David, J., Davis, D. W., Dion, C., Goutier, J., Legault, M., & Roy, P. (2007). Datations U-Pb effectuées dans la Sous-province de l'Abitibi en 2005-2006 Ressources naturelles et faune, 17p.

David, J., McNicoll, V., Simard, M., Bandyayera, D., Hammouche, H., Goutier, J., Pilote, P., Rhéaume, P., Leclerc, F. and Dion, C. (2011).Datations U-Pb effectuées dans les provinces du Supérieur et de Churchill en 2009-2010. Ressources naturelles et faune Québec, 37p.

De La Roche, H., Leterrier, J., Grandclaude, P., & Marchal, M. (1980). A classification of volcanic and plutonic rocks using R 1 R 2-diagram and major-element analyses—its relationships with current nomenclature. Chemical geology, 29(1), p. 183-210.

Deditius, A. P., Utsunomiya, S., Ewing, R. C., & Kesler, S. E. (2009). Nanoscale "liquid" inclusions of As-Fe-S in arsenian pyrite. American Mineralogist, 94(2-3), p. 391-394.

Dimroth, E., Imreh, L., Rocheleau, M., & Goulet, N. (1982). Evolution of the south-central part of the Archean Abitibi Belt, Quebec. Part I: Stratigraphy and paleogeographic model. Canadian Journal of Earth Sciences, 19(9), p. 1729-1758.

Dimroth, E., Imreh, L., Goulet, N., & Rocheleau, M. (1983). Evolution of the south-central segment of the Archean Abitibi Belt, Quebec. Part II: Tectonic evolution and geomechanical model. Canadian Journal of Earth Sciences,20(9), p. 1355-1373.

Eilu, P., Mikucki, E. J., & Dugdale, A. L. (2001). Alteration zoning and primary geochemical dispersion at the Bronzewing lode-gold deposit, Western Australia. Mineralium Deposita, 36(1), p. 13-31.

El Goumi, N., De Souza, S., Enkin, R. J., & Dubé, B. Targeted Geoscience Initiative 4: Contributions to the Understanding of Precambrian Lode Gold Deposits and Implications for Exploration.

Faure, S., and Rafini, S. (2009) Modélisation des paléocontraintes le long de la Faille Destor-Porcupine: implication pour l'exploration aurifère. Forum technologique CONSOREM-Divex

Gaboury, D. (2013). Does gold in orogenic deposits come from pyrite in deeply buried carbon-rich sediments?: Insight from volatiles in fluid inclusions. Geology, 41(12), p.1207-1210.

Gebre-Mariam, M., Hagemann, S. G., & Groves, D. I. (1995). A classification scheme for epigenetic Archaean lode-gold deposits. Mineralium Deposita,30(5), p. 408-410.

Gifkins, C. C., Herrmann, W., & Large, R. R. (2005). Altered volcanic rocks: A guide to description and interpretation (Doctoral dissertation, Centre for Ore Deposit Research, University of Tasmania), 275p.

Goldfarb, R.J., Baker, T., Dubé, B., Groves, D.I., Hart, C.J.R. and Gosselin, P. (2005). Distribution, character, and genesis of gold deposits in metamorphic terranes. Economic Geology 100th anniversary, Vol. 40, p. 407-450

Goutier, J., & Lacroix, S. (1992). Géologie du secteur de la Faille de Porcupine-Destor dans les cantons de Destor et Duparquet: Ministère de l'Énergie et des Ressources. Québec, MB, 92-06, 62p.

Goutier, J. (1997). Géologie de la région de Destor (32D/07-200-0201). Gouvernement du Québec, Ministère des ressources naturelles, Secteur des mines. 37p.

Goutier, J. (2003a). Compilation géoscientifique, Géologie 1:20 000, Duparquet (32D11-200-0102). Ministère des Ressources naturelles du Québec; carte SIGÉOM SI-32D11B-C4G-05F.

Goutier, J. (2003b). Compilation géoscientifique, Géologie 1:20 000, Roquemaure (32D11-200-0101). Ministère des Ressources naturelles du Québec; carte SIGÉOM SI-32D11A-C4G-05F.

Grant, J. A. (1986). The isocon diagram; a simple solution to Gresens' equation for metasomatic alteration. Economic Geology, 81(8), p. 1976-1982.

Groves, D. I. (1993). The crustal continuum model for late-Archaean lode-gold deposits of the Yilgarn Block, Western Australia. Mineralium deposita, 28(6), p. 366-374.

Groves, D. I., Goldfarb, R. J., Gebre-Mariam, M., Hagemann, S. G. and Robert, F. (1998). Orogenic gold deposits: a proposed classification in the context of their crustal distribution and relationship to other gold deposit types. Ore geology reviews, 13(1), p. 7-27.

Groves, D. I., Goldfarb, R. J., Robert, F. and Hart, C. J. (2003). Gold deposits in metamorphic belts: overview of current understanding, outstanding problems, future research, and exploration significance. Economic Geology, 98(1), p. 1-29.

Guy, R. L. (1996). The geology of the Holloway gold deposit, Abitibi Greenstone Belt, Ontario. National Library of Canada= Bibliothèque nationale du Canada.

Helt, K. M., Williams-Jones, A. E., Clark, J. R., Wing, B. A., & Wares, R. P. (2014). Constraints on the genesis of the Archean oxidized, intrusion-related Canadian Malartic gold deposit, Quebec, Canada. Economic Geology, 109(3), p. 713-735.

Hubert, C., Trudel, P., & Gélinas, L. (1984). Archean wrench fault tectonics and structural evolution of the Blake River Group, Abitibi Belt, Quebec. Canadian Journal of Earth Sciences, 21(9), p. 1024-1032.

Jackson, S. L., Sutcliffe, R. H., Ludden, J. N., Hubert, C., Green, A. G., Milkereit, B., ... & Verpaelst, P. (1990). Southern Abitibi greenstone belt: Archean crustal structure from seismic-reflection profiles. Geology, 18(11), p. 1086-1090.

Jébrak, M., & Marcoux, É. (2008). Géologie des ressources minérales. Ministère des ressources naturelles et de la faune, 668 p.

Jensen, L. S. (1976). A new cation plot for classifying subalkalic volcanic rocks, Vol. 66. Ministry of Natural Resources.

Kishida, A., & Kerrich, R. (1987). Hydrothermal alteration zoning and gold concentration at the Kerr-Addison Archean lode gold deposit, Kirkland Lake, Ontario. Economic Geology, 82(3), p. 649-690.

Kerrich, R., Polat, A., & Xie, Q. (2008). Geochemical systematics of 2.7 Ga Kinojevis Group (Abitibi), and Manitouwadge and Winston Lake (Wawa) Fe-rich basalt–rhyolite associations: Backarc rift oceanic crust?. Lithos, 101(1), p. 1-23.

Lambert, G. (2001) Compilation géophysique, projet Pitt Gold, SOQUEM, GM 59030, 5 p. et 8 plans.

Large, R. R., Bull, S. W. and Maslennikov, V. V. (2011). A carbonaceous sedimentary source-rock model for Carlin-type and orogenic gold deposits. Economic Geology, 106(3), p. 331-358.

Legault, M., Fallara, F., Goutier, J., Perron, G., and Cheng., L.Z.(2003). Étude métallogenique et modélisation 3D de la Faille Destor-Porcupine dans le secteur de Duparquet, Sous-province de l'Abitibi (phase 1 de 3) Ministère des Ressources Naturelles et de la Faune, Québec, RP 2003-02, 16 p.

Legault, M., Goutier, J., Beaudoin, G. and Aucoin, M. (2005). Synthèse métallogenique de la Faille Destor-Porcupine, Ministère des Ressources Naturelles et de la Faune, Québec; ET 2005-01, 37 p.

Luinstra, B. R. (2001). Structural geology of the Holloway mine, Abitibi greenstone belt, Ontario. Ontario Geological Survey. 50p.

Luinstra, B. R. (2004). Geology, structure and gold mineralization within the Porcupine-Destor Deformation Zone, Harker-Holloway gold camp, southwestern Abitibi Greenstone Belt, Canada.

Martin, R. D. (2012). Syenite-hosted gold mineralization and hydrothermal alteration at the Young-Davidson deposit, Matachewan, Ontario.

McNicoll, V., Goutier, J., Dubé, B., Mercier-Langevin, P., Ross, P. S., Dion, C. & Gibson, H. (2014). U-Pb Geochronology of the Blake River Group, Abitibi Greenstone Belt, Québec, and Implications for Base Metal Exploration. Economic Geology, 109(1), p. 27-59.

Morey, A. A., Tomkins, A. G., Bierlein, F. P., Weinberg, R. F., & Davidson, G. J. (2008). Bimodal distribution of gold in pyrite and arsenopyrite: examples from the Archean Boorara and Bardoc shear systems, Yilgarn Craton, Western Australia. Economic Geology, 103(3), 599-614.

Mueller, W., Donaldson, J. A., Dufresne, D., & Rocheleau, M. (1991). The Duparquet Formation: sedimentation in a late Archean successor basin, Abitibi greenstone belt, Quebec, Canada. Canadian Journal of Earth Sciences, 28(9), p. 1394-1406.

Mueller, W. U., Daigneault, R., Mortensen, J. K., and Chown, E. H. (1996). Archean terrane docking: upper crust collision tectonics, Abitibi greenstone belt, Quebec, Canada. Tectonophysics, 265(1), p. 127-150.

Mueller, W. U., Friedman, R., Daigneault, R., Moore, L., & Mortensen, J. (2012). Timing and characteristics of the Archean subaqueous Blake River megacaldera complex, Abitibi greenstone belt, Canada. Precambrian Research, 214, p. 1-27.

Olivo, G. R. and Williams-Jones, A. E. (2002). Genesis of the auriferous C quartz-tourmaline vein of the Siscoe mine, Val d'Or district, Abitibi subprovince, Canada: structural, mineralogical and fluid inclusion constraints. Economic Geology, 97(5), p.929-947.

Percival, J. A. (2007). Geology and metallogeny of the Superior Province, Canada. Mineral Deposits of Canada: A Synthesis of Major Deposit-Types, District Metallogeny, the Evolution of Geological Provinces, and Exploration Methods, p. 903-928.

Pilote, P., McNicoll, V., Daigneault, R. and Moorhead, J. (2009) Géologie et nouvelles corrélations dans la partie ouest du Groupe de Malartic et dans le Groupe de Kinojévis, Québec. Congrès Abitibi 2009, GM 64195, p.55-60

Pitcairn, I. K., Teagle, D. A., Craw, D., Olivo, G. R., Kerrich, R. and Brewer, T. S. (2006). Sources of metals and fluids in orogenic gold deposits: insights from the Otago and Alpine Schists, New Zealand. Economic Geology, 101(8), p.1525-1546

Polat, A., & Kerrich, R. (2001). Magnesian andesites, Nb-enriched basalt-andesites, and adakites from late-Archean 2.7 Ga Wawa greenstone belts, Superior Province, Canada: implications for late Archean subduction zone petrogenetic processes. Contributions to Mineralogy and Petrology, 141(1), p.36-52.

Powell, W. G., Carmichael, D. M., & Hodgson, C. J. (1995). Conditions and timing of metamorphism in the southern Abitibi greenstone belt, Quebec.Canadian Journal of Earth Sciences, 32(6), p. 787-805.

Power-Fardy, D. and Breede, K. (2011). Technical report and mineral resource estimate update for the Duquesne-Ottoman Property, Québec, Canada. For Xmet Inc. 104 p.

Rabeau, O., Royer, J. J., Jébrak, M., & Cheilletz, A. (2013). Log-uniform distribution of gold deposits along major Archean fault zones. Mineralium Deposita, 48(7), p. 817-824.

Rafini, S. (2014). Typologie des minéralisations aurifères associées à la Faille de Cadillac. Rapport du projet CONSOREM 2011-01 et 2012-01, 45 p.

Robert, F., & Brown, A. C. (1986). Archean gold-bearing quartz veins at the Sigma Mine, Abitibi greenstone belt, Quebec; Part I, Geologic relations and formation of the vein system. Economic Geology, 81(3), p. 578-592.

Robert, F., & Brown, A. C. (1986). Archean gold-bearing quartz veins at the Sigma Mine, Abitibi greenstone belt, Quebec; Part II, Vein paragenesis and hydrothermal alteration. Economic Geology, 81(3), p. 593-616.

Robert, F. (2001). Syenite-associated disseminated gold deposits in the Abitibi greenstone belt, Canada. Mineralium Deposita, 36(6), p. 503-516

Ross, P. S., & Bédard, J. H. (2009). Magmatic affinity of modern and ancient subalkaline volcanic rocks determined from trace-element discriminant diagrams. Canadian Journal of Earth Sciences, 46(11), 823-839.

Robert, F., Poulsen, K. H., Cassidy, K. F. and Hodgson, C. J. (2005). Gold metallogeny of the Superior and Yilgarn cratons. Economic Geology 100th anniversary, p. 1001-1033.

Schwarcz, H. P., & Rees, C. E. (1986). Sulphur isotope studies of Archean gold deposits. Ontario Ministry of Northern Development and Mines.

Simard, M., Gaboury, D., Daigneault, R., & Mercier-Langevin, P. (2013). Multistage gold mineralization at the Lapa mine, Abitibi Subprovince: insights into auriferous hydrothermal and metasomatic processes in the Cadillac–Larder Lake Fault Zone. Mineralium Deposita, 48(7), 883-905

Stott, G. M., Corkery, M. T., Percival, J. A., Simard, M., & Goutier, J. (2010). 20. Project Units 98-006 and 98-007. A Revised Terrane Subdivision of the Superior Province.

Taylor, S. R., McLennan, S. M., Armstrong, R. L., & Tarney, J. (1981). The composition and evolution of the continental crust: rare earth element evidence from sedimentary rocks [and discussion]. Philosophical Transactions of the Royal Society of London A: Mathematical, Physical and Engineering Sciences, 301(1461), p. 381-399.

Thurston, P. C., Ayer, J. A., Goutier, J., & Hamilton, M. A. (2008). Depositional gaps in Abitibi greenstone belt stratigraphy: a key to exploration for syngenetic mineralization. Economic Geology, 103(6), p. 1097-1134.

Trudel, P., Hoy, L., Gaulin, R., Lao, K. (1991). Géologie de la mine Elder, canton de Beauchastel – Région de Rouyn-Noranda. Ministère de l'Énergie, des Mines et des Ressources du Québec. MB 91-09, 153p.

White, N. C., & Hedenquist, J. W. (1995). Epithermal gold deposits: styles, characteristics and exploration. SEG newsletter, 23(1), p. 9-13.

Winchester, J. A., & Floyd, P. A. (1977). Geochemical discrimination of different magma series and their differentiation products using immobile elements. Chemical geology, 20, p. 325-343.

Wood, P. C. (1991). The Hollinger-McIntyre gold-quartz vein system, Timmins, Ontario: geologic characteristics, fluid properties and light stable isotope geochemistry. Ontario Ministry of Northern Development and Mines, Ontario Geological Survey.

Wong, L., Davis, D. W., Krogh, T. E., & Robert, F. (1991). U Pb zircon and rutile chronology of Archean greenstone formation and gold mineralization in the Val d'Or region, Quebec. Earth and Planetary Science Letters, 104(2), p. 325-336.

Xue, Y., Campbell, I., Ireland, T. R., Holden, P., & Armstrong, R. (2013). No mass-independent sulfur isotope fractionation in auriferous fluids supports a magmatic origin for Archean gold deposits. Geology, 41(7), p. 791-794.

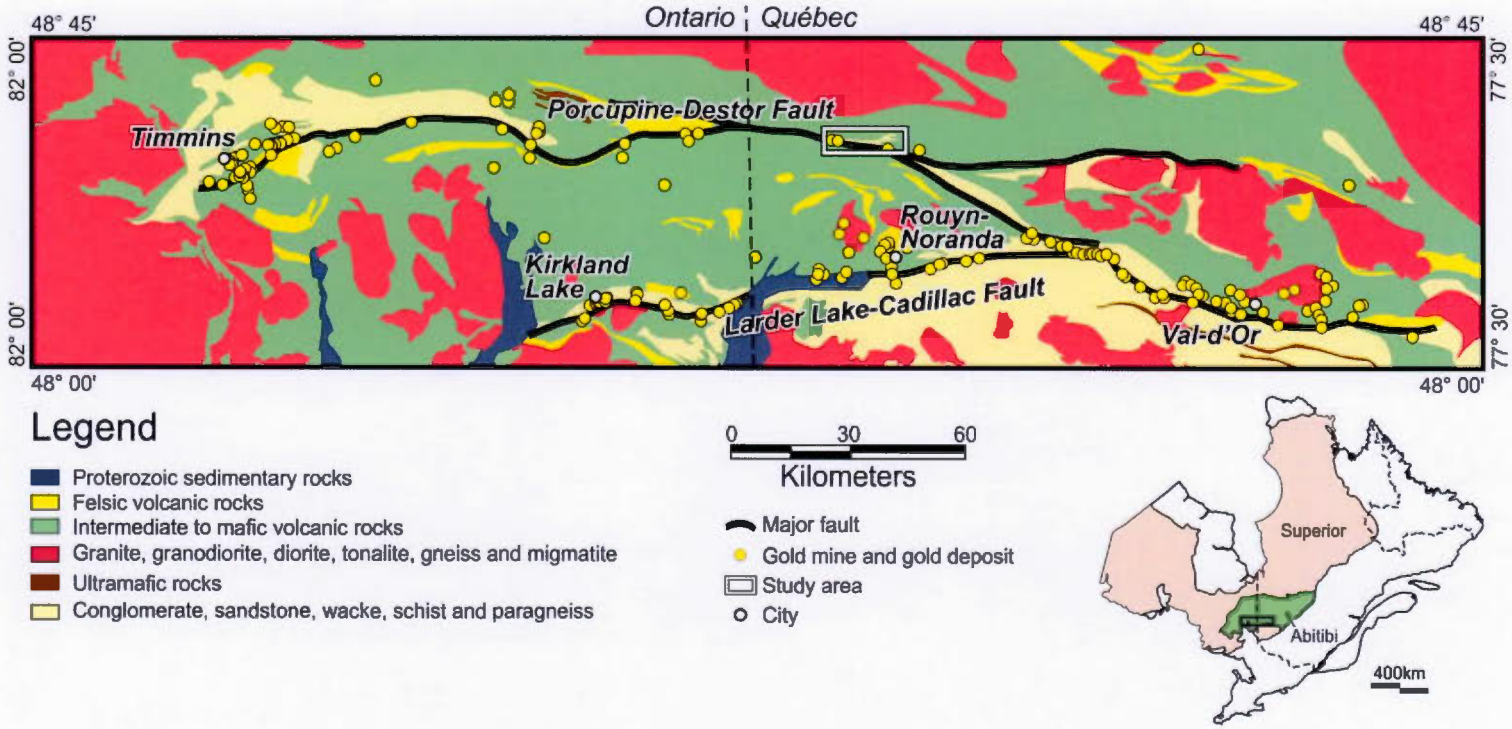

FIGURE 1.1- Geological map of the Timmins-Val-d'Or gold belt showing the location of the Porcupine-Destor and Larder Lake-Cadillac fault zones, and the distribution of gold deposits (modified from Rabeau *et al.*, 2013). The inset shows the distribution of the Abitibi greenstone belt and Superior Province.

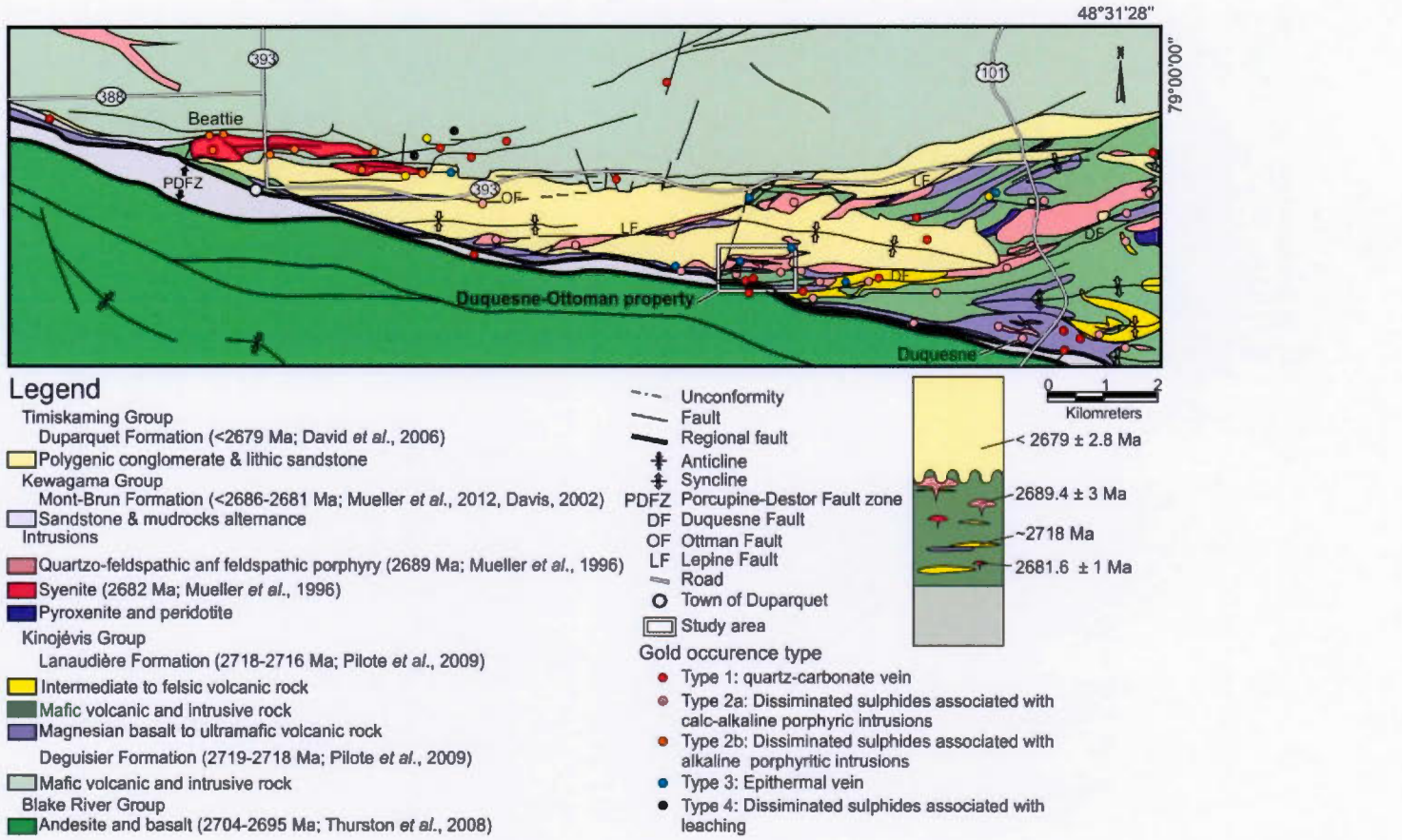

FIGURE 1.2- Geological map of the Duparquet area showing the typology and location of the main gold deposits and showings. The figure is taken and modified from Goutier, 2003a, b), Legault *et al.* (2005) and Thurston *et al.* (2008).

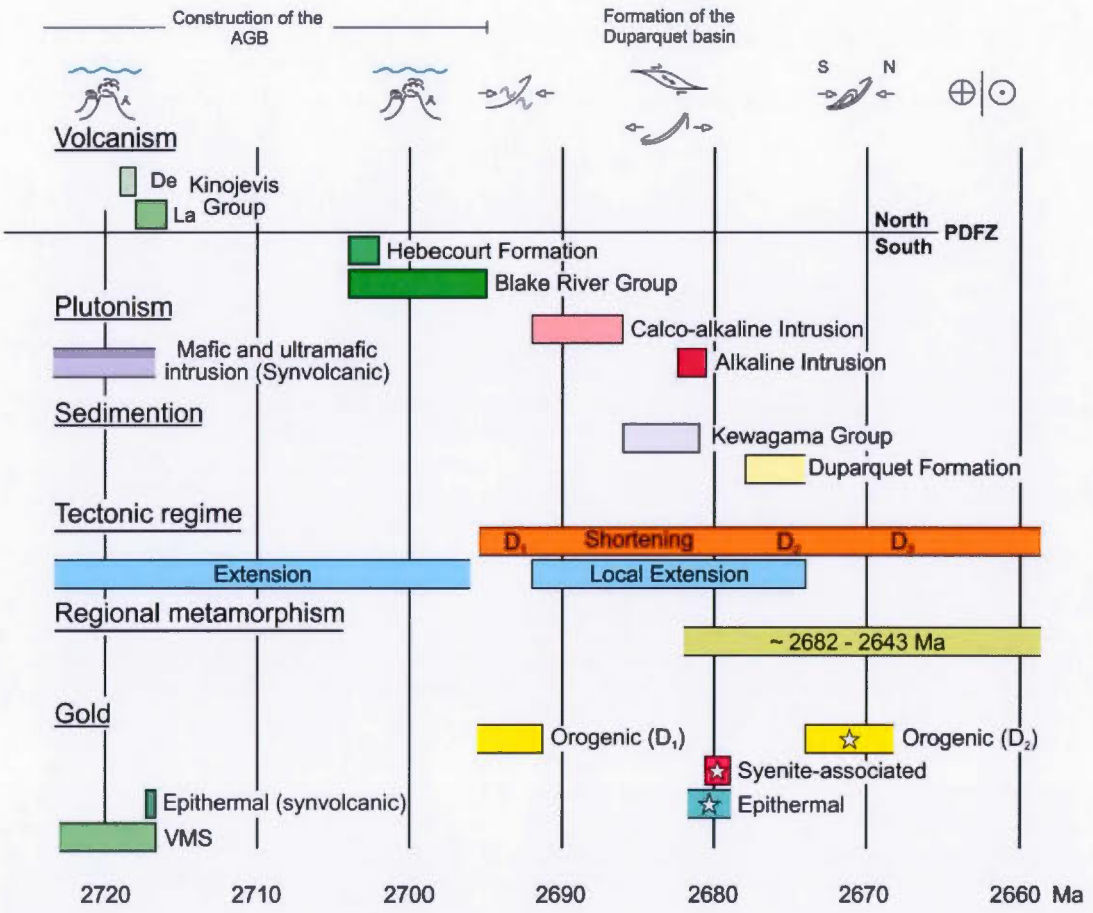

FIGURE 1.3- Geological evolution and metallogeny of the Duparquet area (Modified from Legault *et al.*, 2005). De= Deguisier Formation; La = Lanaudière Formation; D_1, D_2, D_3 = Deformation event. The white stars represent the two gold-related hydrothermal phases of the Duquesne-Ottoman property.

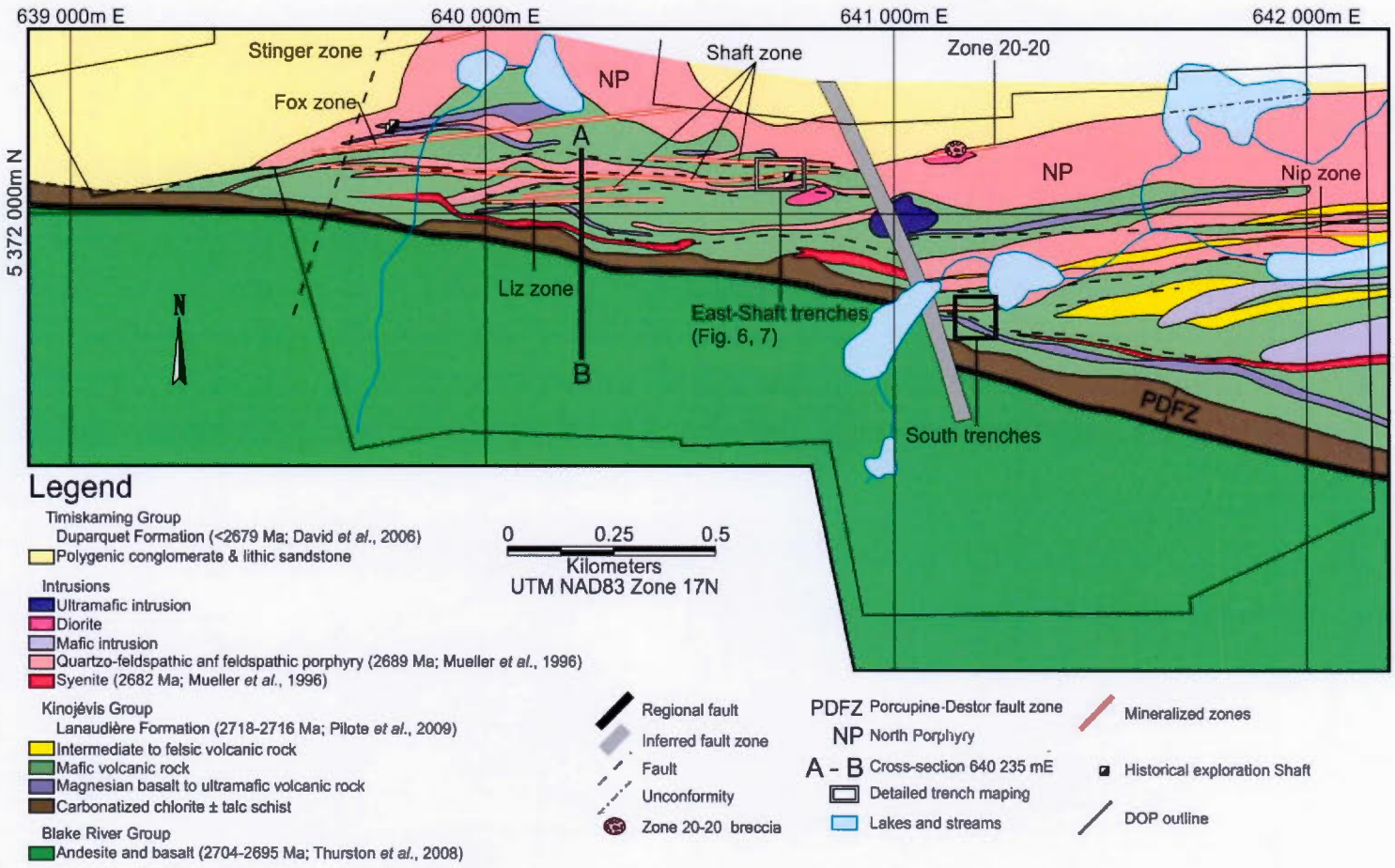

FIGURE 1.3 – Geological map of the Duquesne-Ottoman property (modified from Power-Fardy and Breede, 2011).

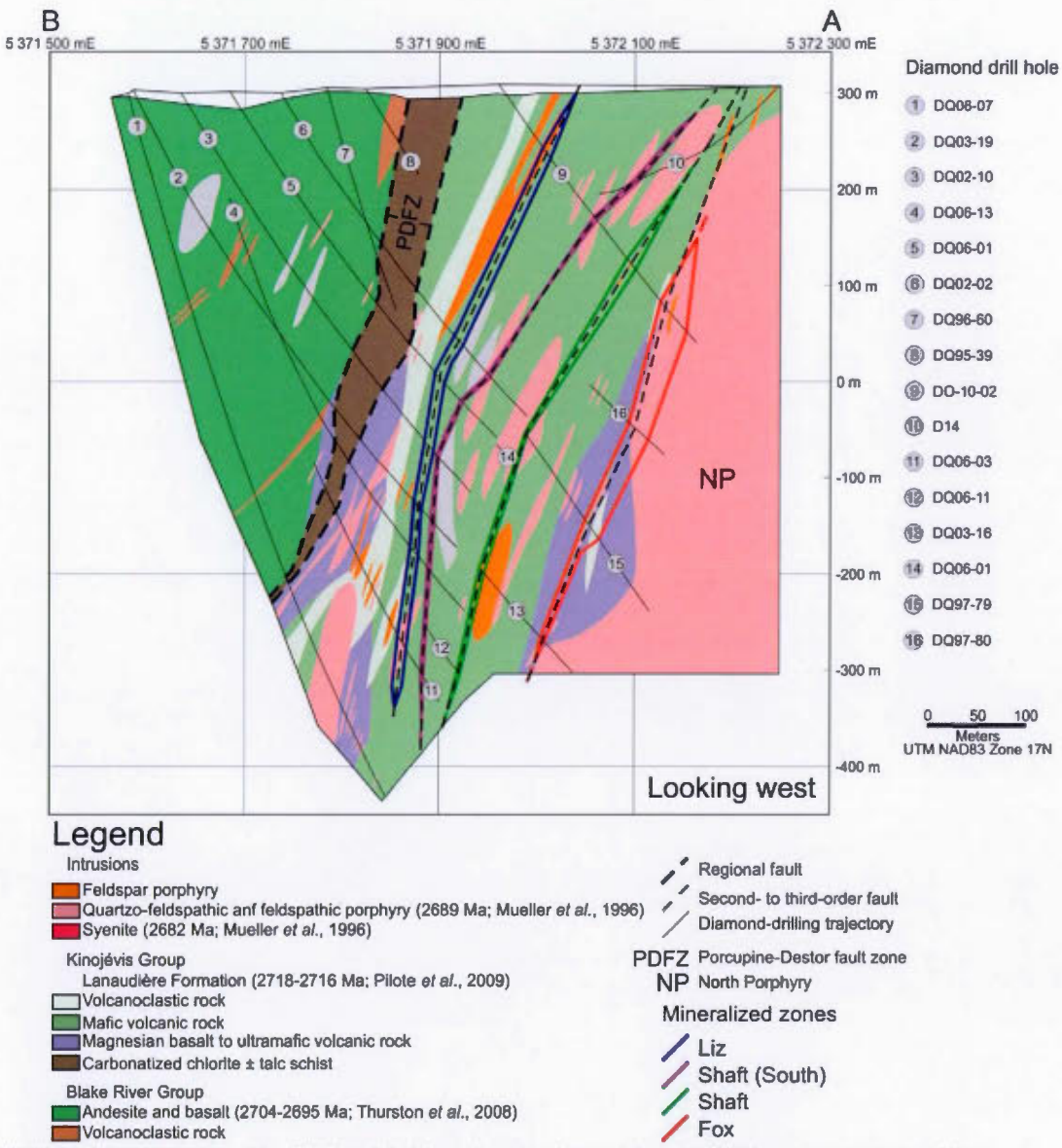

FIGURE 1.4–Cross-section of the DOP (Modified from Xmet Inc. internal data, 640235E cross-section). A and B are positioned on figure 4.

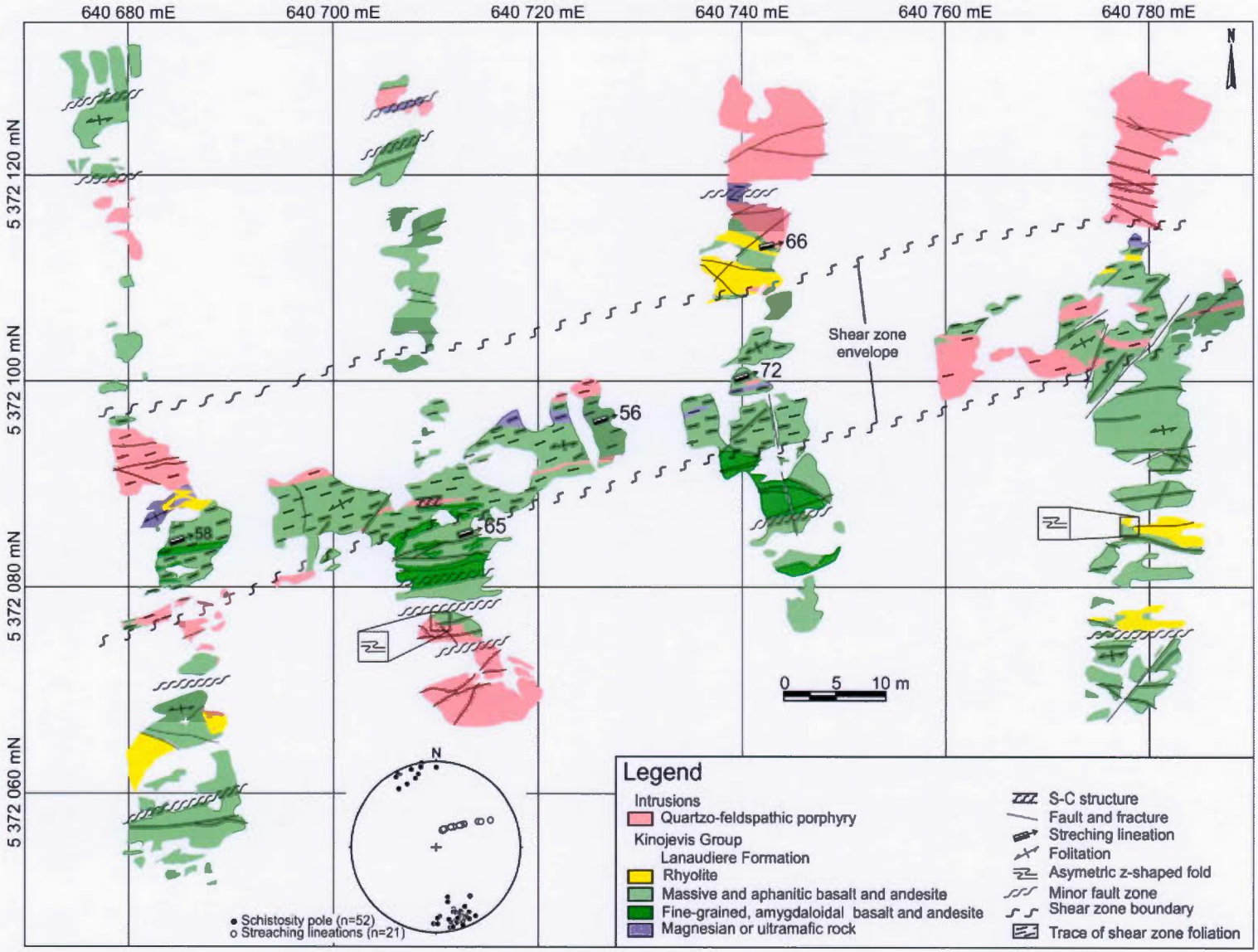

FIGURE 1.5- Geological map of the East-Shaft trenches. Structural measurement presented as equal-area, lower-hemisphere stereographic projections. The number of measurements (*n*) is displayed along with legend at the lower left of stereonet. Refer to figure 4 for location of the trenches of the DOP

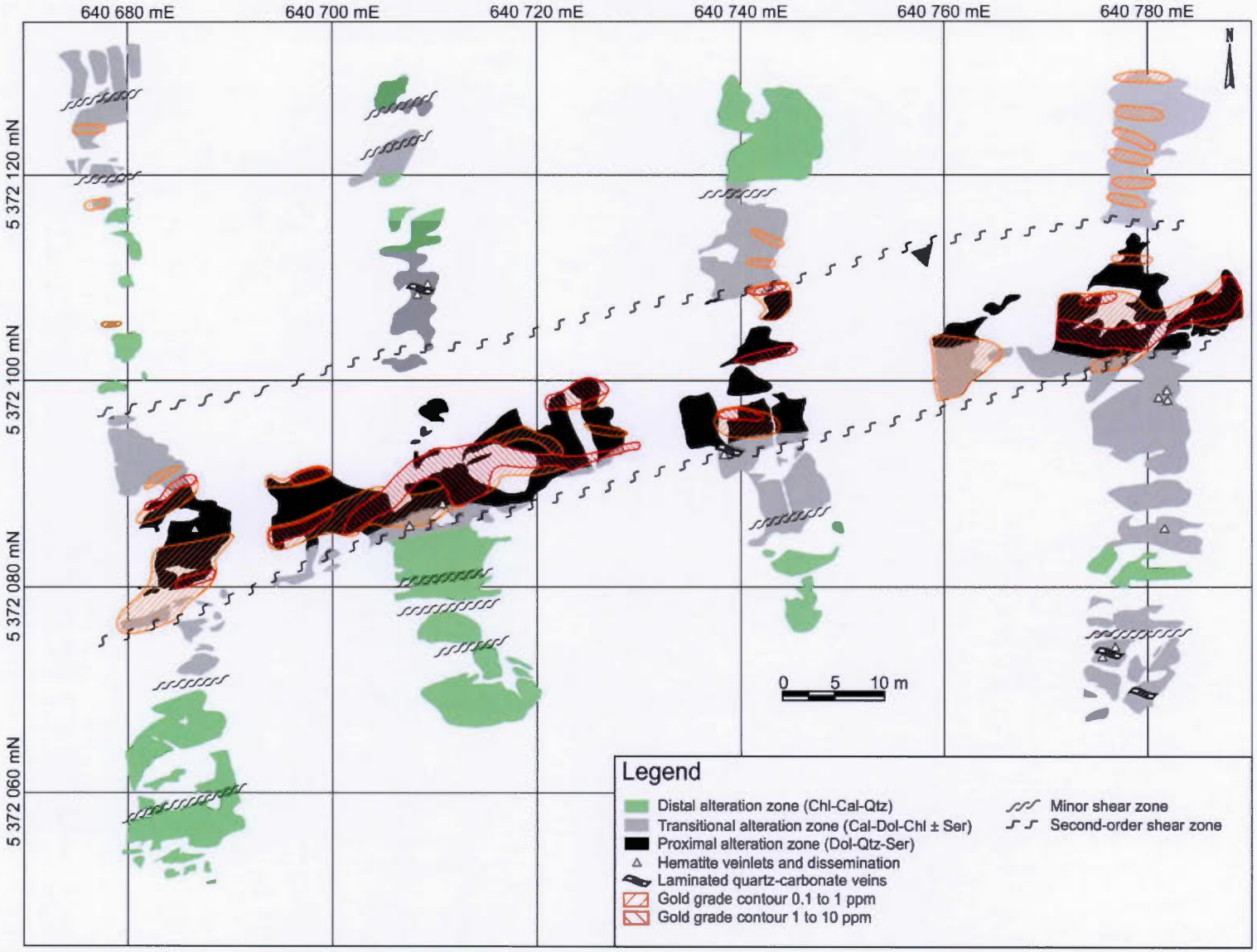

FIGURE- 1.6 Qualitative alteration mapping spatially correlated with the quantitative trench sampling gold results of the East-Shaft trenches.

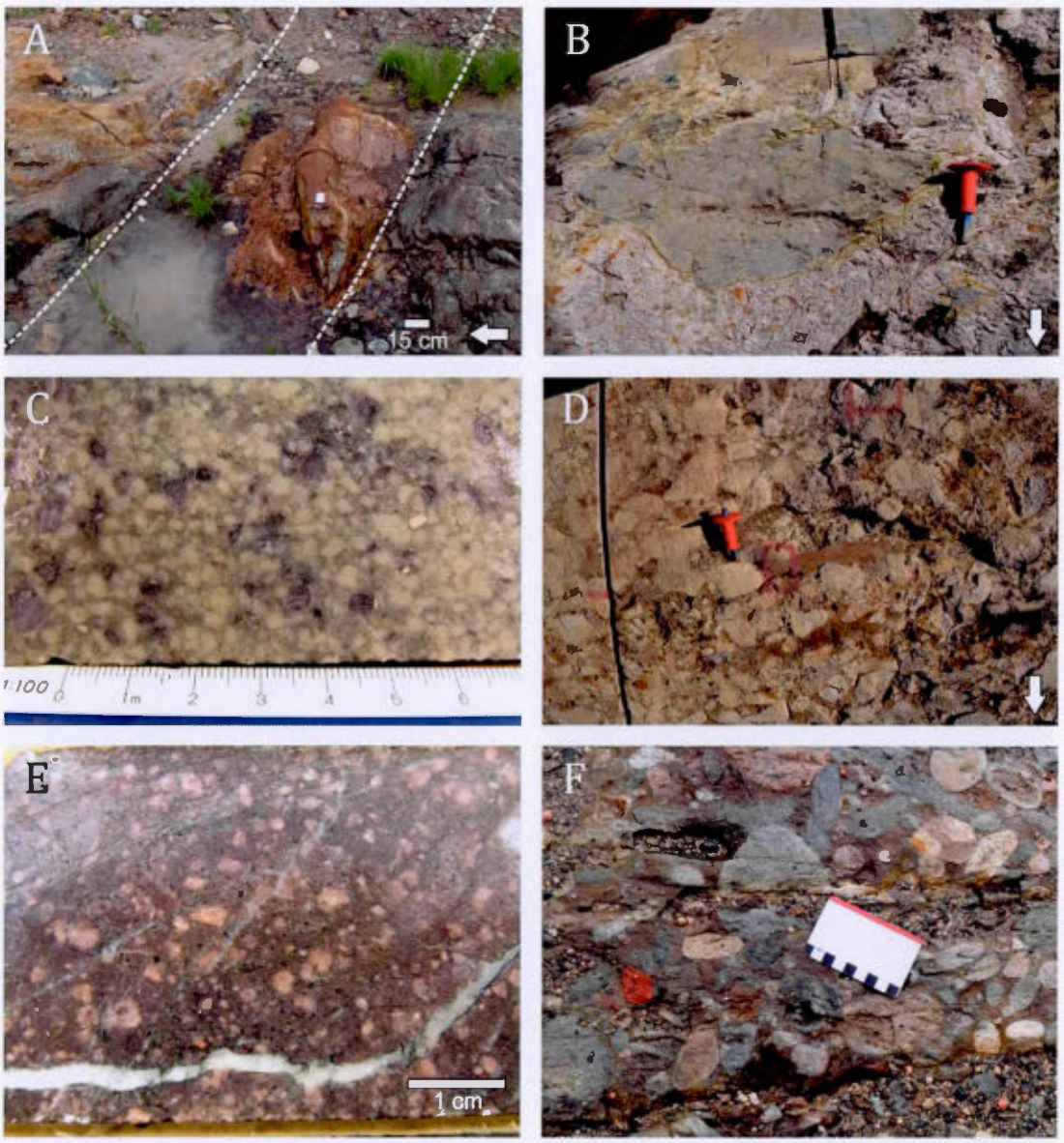

FIGURE 1.7– Photographs showing particular rocks of the Duquesne-Ottoman. (A) Highly deformed sliver of carbonate-chlorite-talc brown ultramafic schist quench in between the North Porphyry on the left and a rhyolite on the right side of the picture, white arrow pointing north and white dotted line for lithological boundary. (B) Local amoeboidale and brecciated flow of felsic and mafic volcanic rocks. Chisel for scale and white arrow pointing north. (C) Moderately sericite-altered quartz-feldspar porphyry. Ruler (cm) for scale. (D) Explosive breccia of the 20-20 zone. Chisel for scale and white arrow pointing north (E) Porphyritic alkaline intrusion (F) Undeformed polymictic conglomerate of the Duparquet Formation.

A

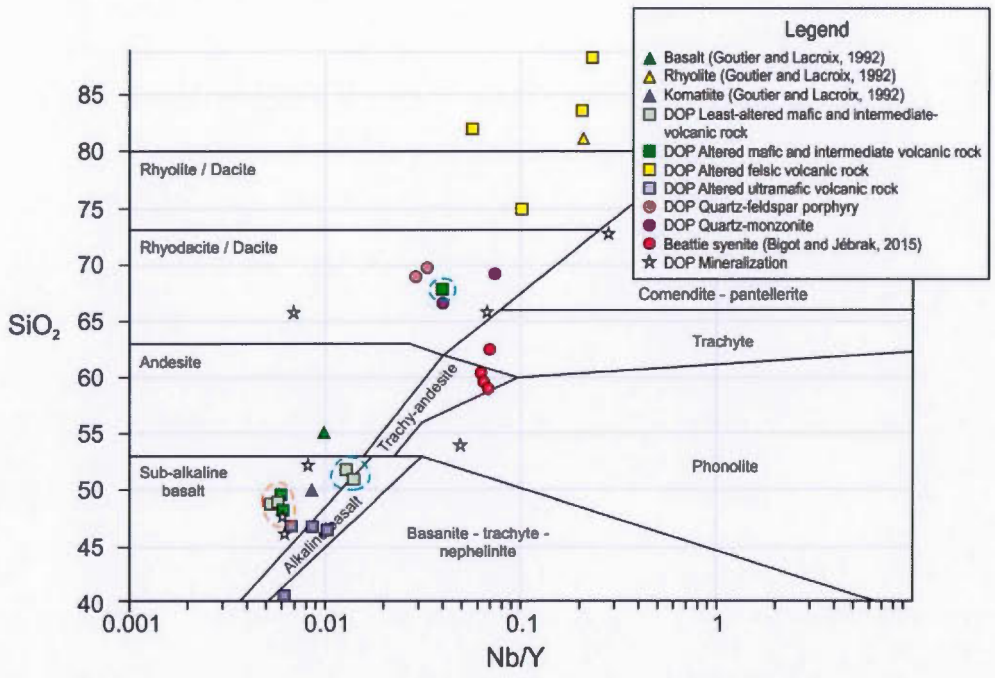
Legend
Basalt (Goutier and Lacroix, 1992)
Rhyolite (Goutier and Lacroix, 1992)
Komatiite (Goutier and Lacroix, 1992)
DOP Least-altered mafic and intermediate-volcanic rock
DOP Altered mafic and intermediate volcanic rock
DOP Altered felsic volcanic rock
DOP Altered ultramafic volcanic rock
DOP Quartz-feldspar porphyry
DOP Quartz-monzonite
Beattie syenite (Bigot and Jébrak, 2015)
DOP Mineralization
Rhyolite / Dacite
Rhyodacite / Dacite
Andesite
Sub-alkaline basalt
Trachy-andesite
Alkaline basalt
Comendite - pantellerite
Trachyte
Phonolite
Basanite - trachyte - nephelinite
SiO2
Nb/Y
85
80
75
70
65
60
55
50
45
40
0.001
0.01
0.1
1

B

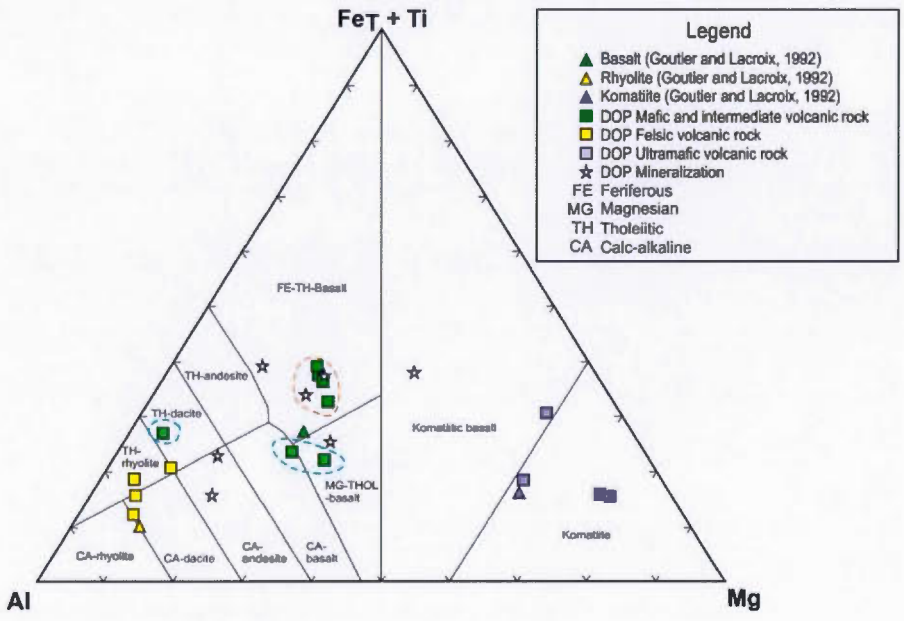
FeT + Ti
Al
Mg
Legend
Basalt (Goutier and Lacroix, 1992)
Rhyolite (Goutier and Lacroix, 1992)
Komatiite (Goutier and Lacroix, 1992)
DOP Mafic and intermediate volcanic rock
DOP Felsic volcanic rock
DOP Ultramafic volcanic rock
DOP Mineralization
FE Feriferous
MG Magnesian
TH Tholeiitic
CA Calc-alkaline
FE-TH-Basalt
TH-andesite
TH-dacite
TH-rhyolite
Komatiitic basalt
MG-THOL -basalt
Komatiite
CA-rhyolite
CA-dacite
CA-andesite
CA-basalt

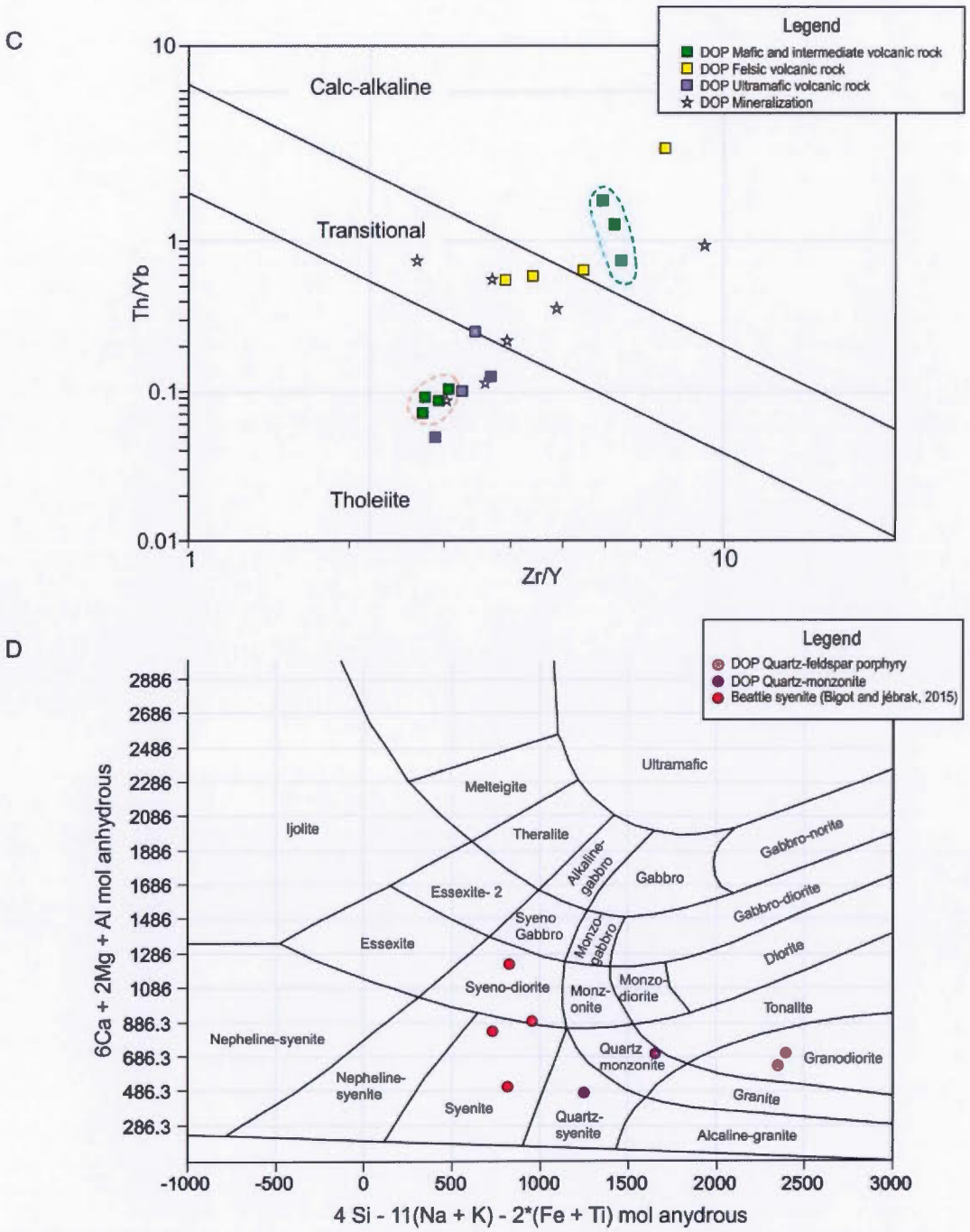

FIGURE 1.8– Geochemical discrimination diagrams. (A) Nb/Y versus SiO_2 diagram from Winchester and Floyd (1977), (B) $Fe_{(T)}$+Ti versus Al versus Mg diagram from Jensen (1976), (C) Zr/Y versus Th/Yb diagram for discrimination of geochemical affinities from Ross and Bédard (2009), and (D) R1 versus R2 intrusive classification from De La Roche *et al.* (1980). The orange dotted line represents the tholeiitic basalt trend and the blue dotted line represent the calc-alkaline andesite/basalt trend.

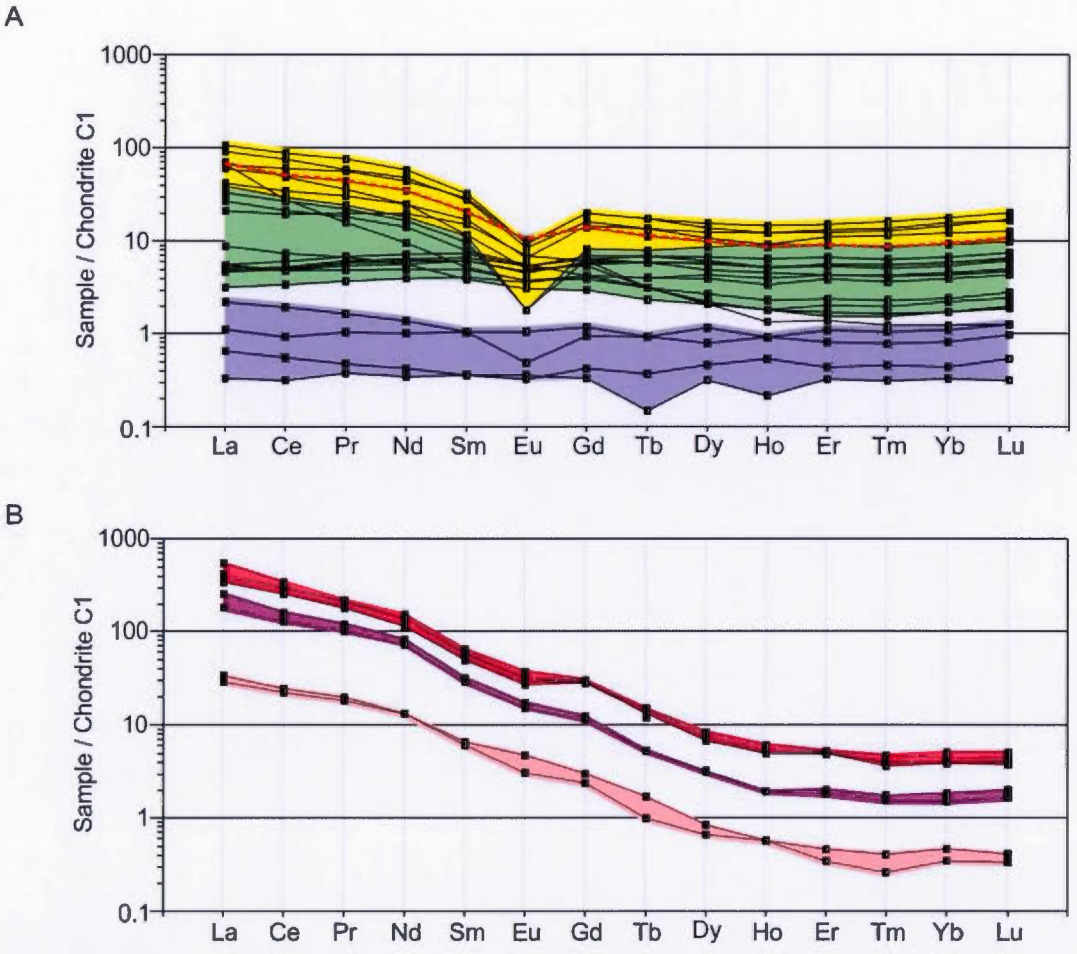

FIGURE 1.9–Chondrite normalized rare earth element diagrams normalized to C1 chondrite values of Palme and O'Neil (2004) for (A) volcanic rocks of the DOP, and (B) intrusive rocks of the DOP and Beattie syenite. Data for the Beattie syenite are from Bigot and Jébrak (2015). The colored background is provided to broadly delineate each lithology. Yellow: rhyolite; green: basalt; light purple: komatiite; light pink: quartz-feldspar porphyry; dark purple: DOP quartz-monzonite; pinkinsh red: Beattie syenite. The red dotted line in (A) represents the upper limit of the mafic volcanic rocks samples.

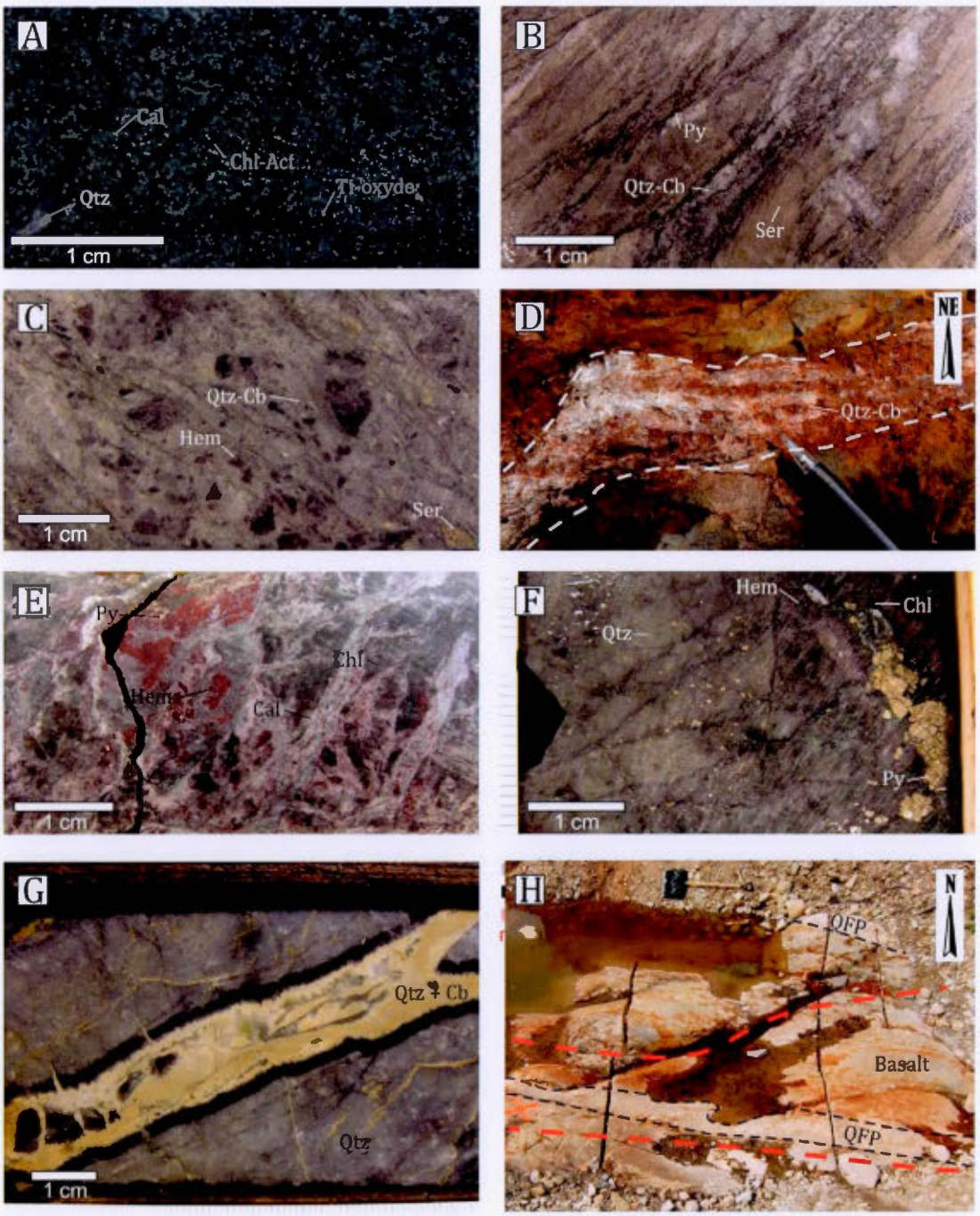

FIGURE 1.10–Photographs of alteration features on the DOP. (A) Regional metamorphic greenschist grade assemblage. (B) Strong proximal ferroan carbonate-sericite-quartz alteration of the Liz zone. (C) Strong proximal ferroan carbonate-sericite-quartz ± hematite alteration of the Shaft zone. (D) Quartz-carbonate laminated vein cutting basaltic rock on the East-Shaft trenches. Pen for scale. (E) Strong quartz-calcite-hematite alteration of the Fox zone. (F) Massive quartz replacement with patchy hematite dust and

disseminated pyrite in the Fox zone (G) Epithermal quartz and carbonate vein showing open-space crystallization and cutting massive quartz replacement in the Foz zone (H) East-Shaft trench highlighting strong proximal alteration on mafic rocks and distributed favorably along quartz-feldspar porphyry deformed dyke. Shovel for scale. Red dotted line: 10 ppm Au contour. Black dotted line: Lithological contact between basalt and QFP. Abbreviation: Act=Actinolite, Cal=Calcite, Cb=Carbonate, Chl=Chlorite, Dol =Ferroan dolomite, Hem=Hematite, Py=Pyrite, Qtz =Quartz, Ser =Sericite.

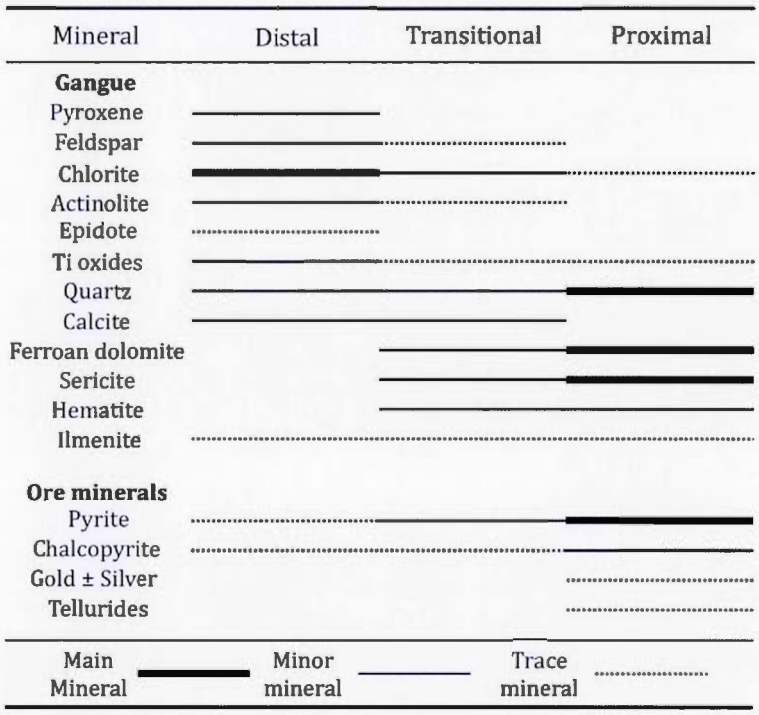

FIGURE 1.11– Paragenetic sequence from distal to proximal alteration in mafic rocks of the Shaft and Liz zones, as described on the East-Shaft trenches and from drill core of the Shaft and Liz zones.

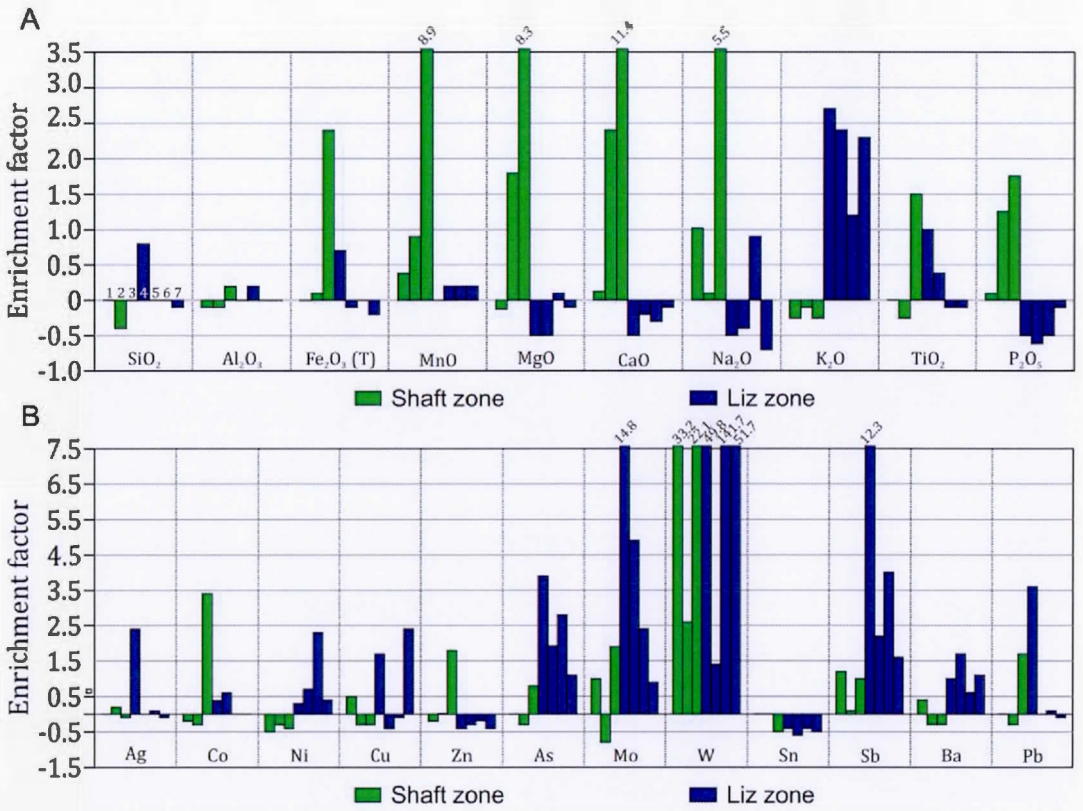

FIGURE 1.12 -Enrichment factors for seven samples from the DOP. (A) Major elements and; (B) Trace elements. 1) Sample #30954; 2)Sample #30959; 3) Sample #30960; 4) Sample #30963; 5) Sample #30964; 6) Sample #30975; 7) Sample #30976.

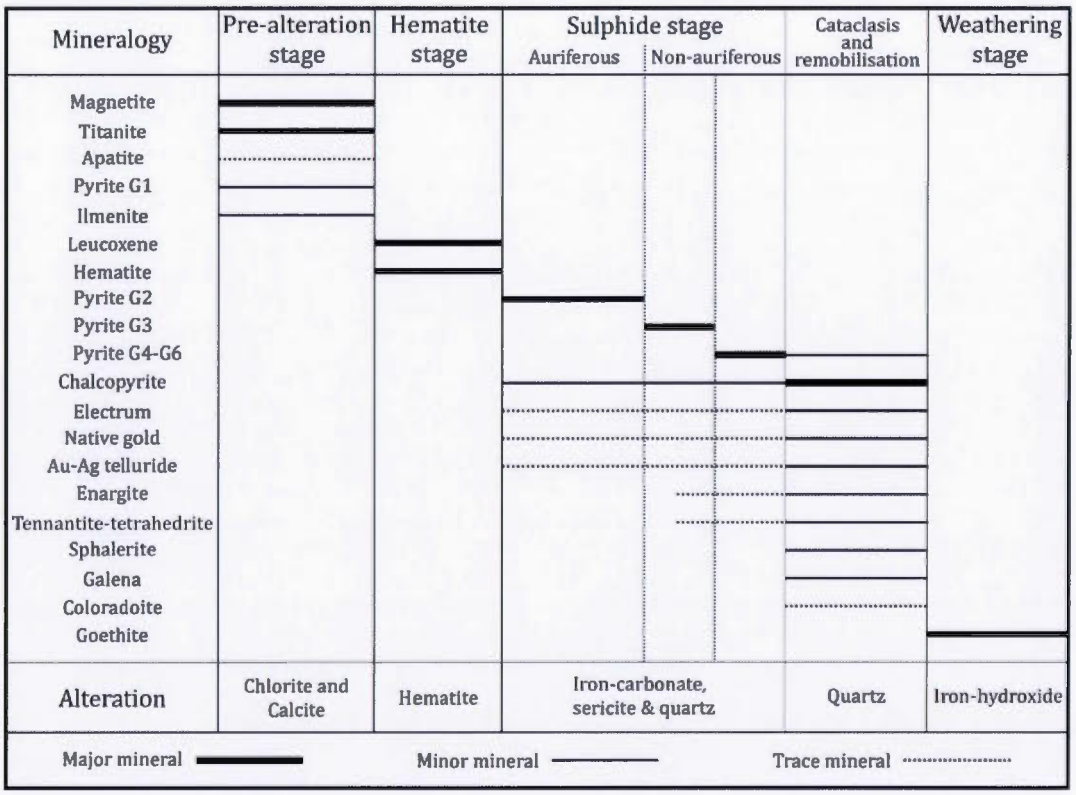

FIGURE 1.13– Mineral paragenesis of the Liz and Shaft zones. A multistage process: (1) Pre-ore metamorphic stage, (2) metasomatic oxidation where hematite replaces magnetite and leucoxene replaces titanite, (3) first generation of pyrite alters and becomes porous, enveloped by multiple generations of pyrite with gold and telluride inclusions, (4) cataclasis of pyrite and remobilisation of precious and base metals where gold crystallizes in the microfractures and along boundaries of cataclased pyrite, (5) sulphide weathering to iron-hydroxides.

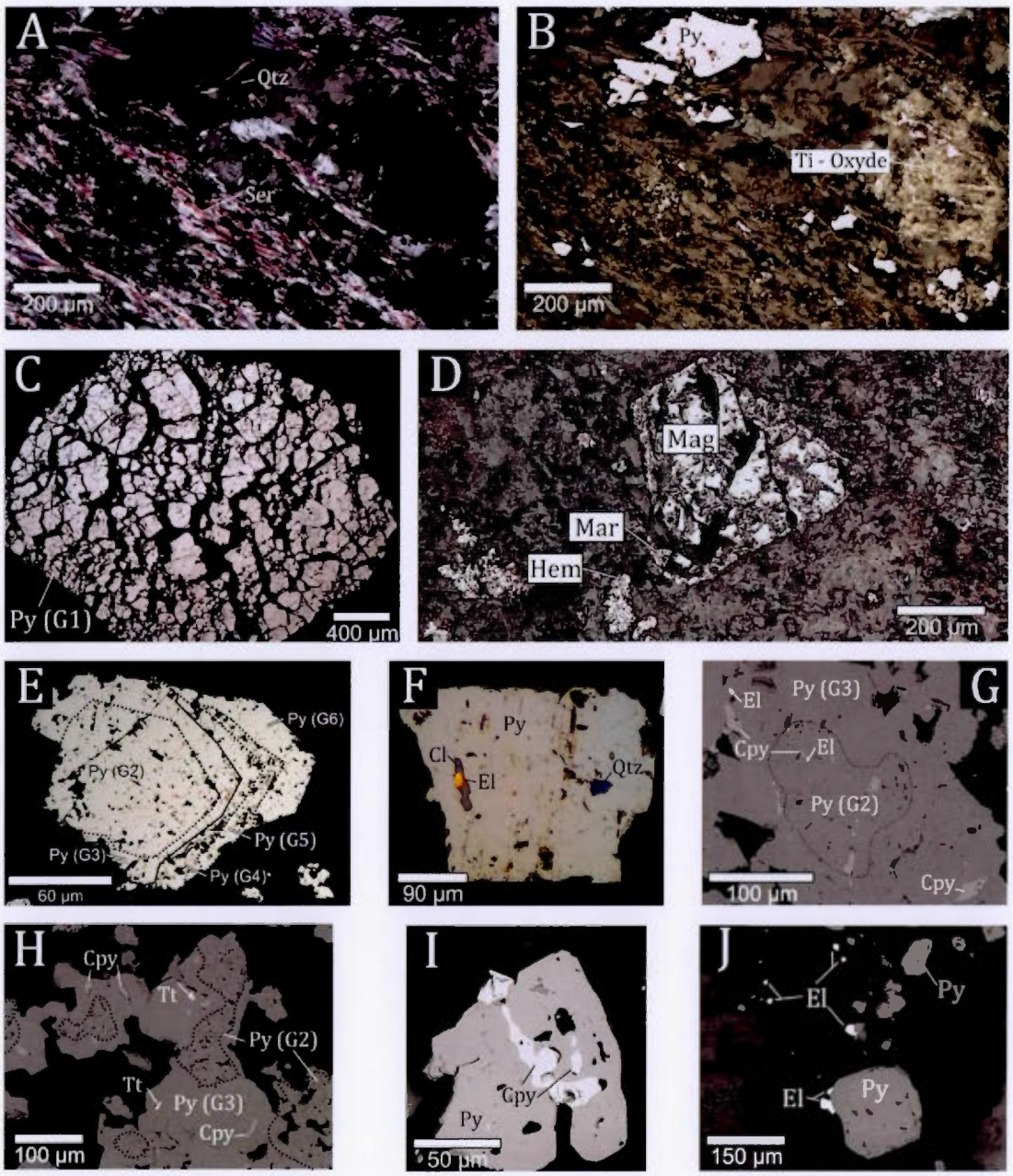

FIGURE 1.14– Microphotographs of the mineral paragenesis of the Shaft and Liz zones. (A) Typical Shaft and Liz zones proximal alteration assemblage related to mineralized zones, viewed in polarized light (B) Typical Shaft and Liz zonesproximal alteration assemblage related to mineralized zones, viewed in reflected light (C) First generation pyrite (G1) in least-altered mafic volcanic rock. (D) Martitization of magnetite forming hematite. (E) Sulphidation stage, overgrowth of multiple generations of pyrite (G2 to G6). (F) Electrum, coloradoite and quartz inclusions in pyrite. (G) Electrum and chalcopyrite inclusions within two generations of pyrite. (H) Tetrahedrite-tennantite and chalcopyrite inclusions in pyrite. (I) Chalcopyrite filling fracture and porosity in deformed pyrite grain. (I) Electrum at pyrite margin and in gangue minerals.

Abbreviation: Cl=Coloradoite, Cpy=Chalcopyrite, El= Electrum, Hem=Hematite, Mag=Magnetite, Mar=Martite, Py=Pyrite, Ser=Sericite, Qtz=Quartz, Tt=Tetrahedrite-Tennantite.

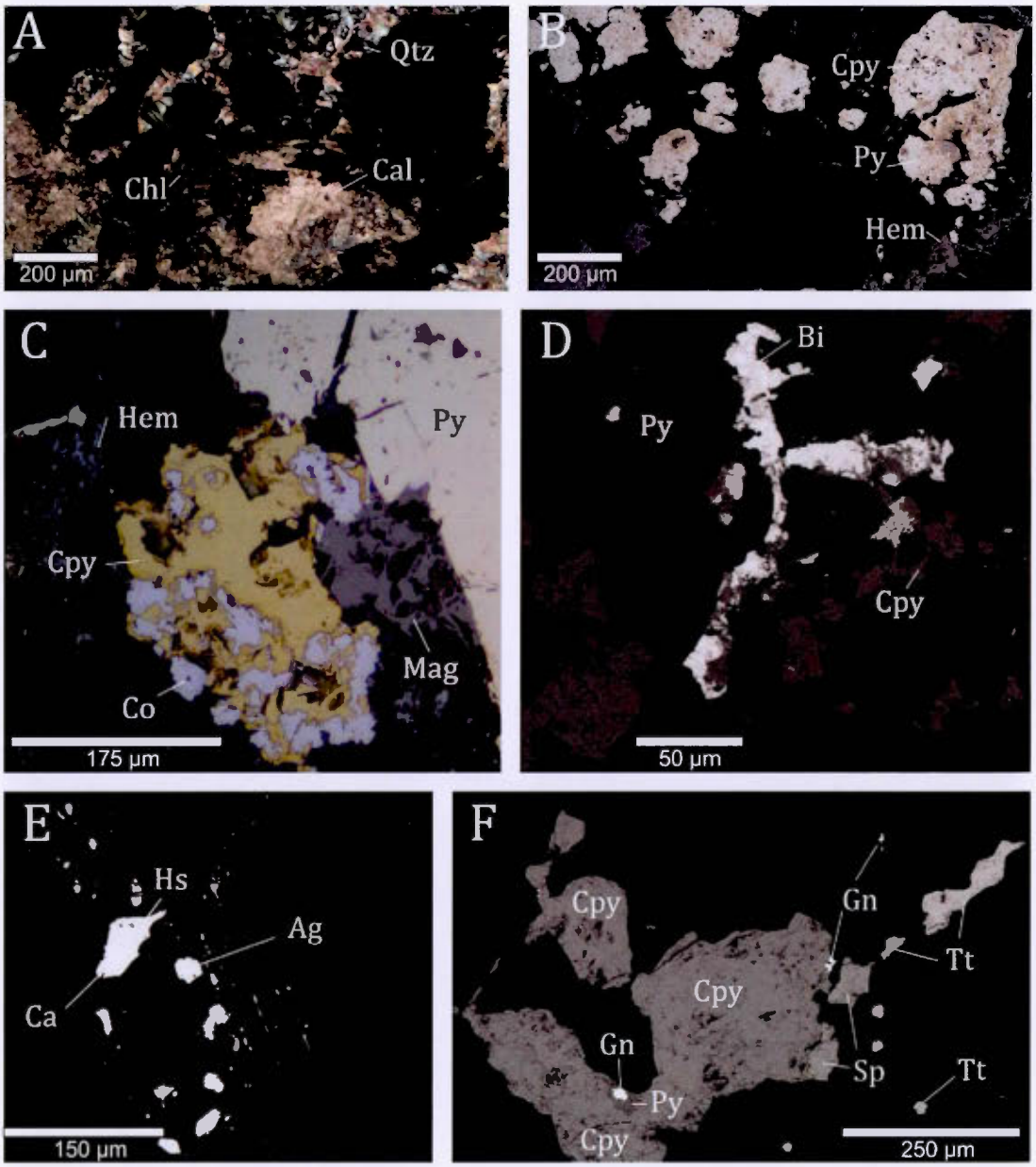

FIGURE 1.15– Photomicrographs of the Fox zone. (A) Typical Fox zone alteration assemblage related to mineralized zones, viewed in polarized light (B) Typical Fox zone alteration assemblage related to mineralized zones, viewed in reflected light (C) Bismuth-bearing mineral in a pyrite and chalcopyrite aggregate. (D) Typical Fox assemblage consisting of pyrite, hematite, magnetite and chalcopyrite clusters and a cobalt-bearing mineral. (E) Fine droplets of native silver and Au-Ag tellurides inclusions in pyrite. (F) Epithermal veinlet composed of chalcopyrite, pyrite, sphalerite and sulphosalts. Abbreviation: Ag= Native silver; Bi= Bismuth-bearing mineral; Ca=calaverite; Cal=Calcite; Chl= Chlorite; Co=Cobalt-bearing mineral,

Cpy=Chalcopyrite; Gn=Galena; Hem=Hematite; Hs= Hessite; Mag=Magnetite; Py=Pyrite; Qtz=Quartz; Sp=Sphalerite; Tt=Tetrahedrite-Tennantite.

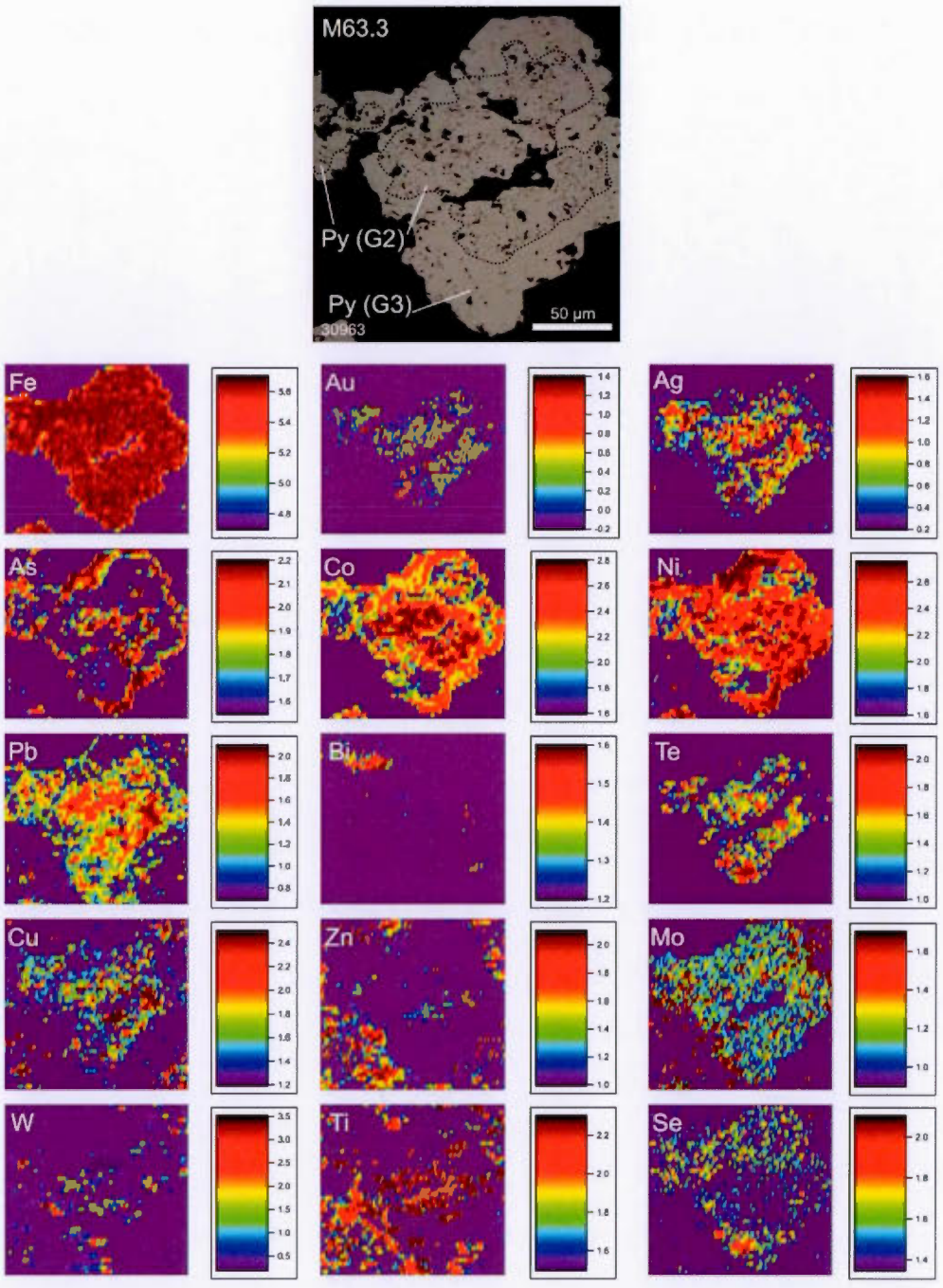

FIGURE 1.16– LA-ICP-MS element map of multistage pyrite of the Liz zone. Scale in ppm.

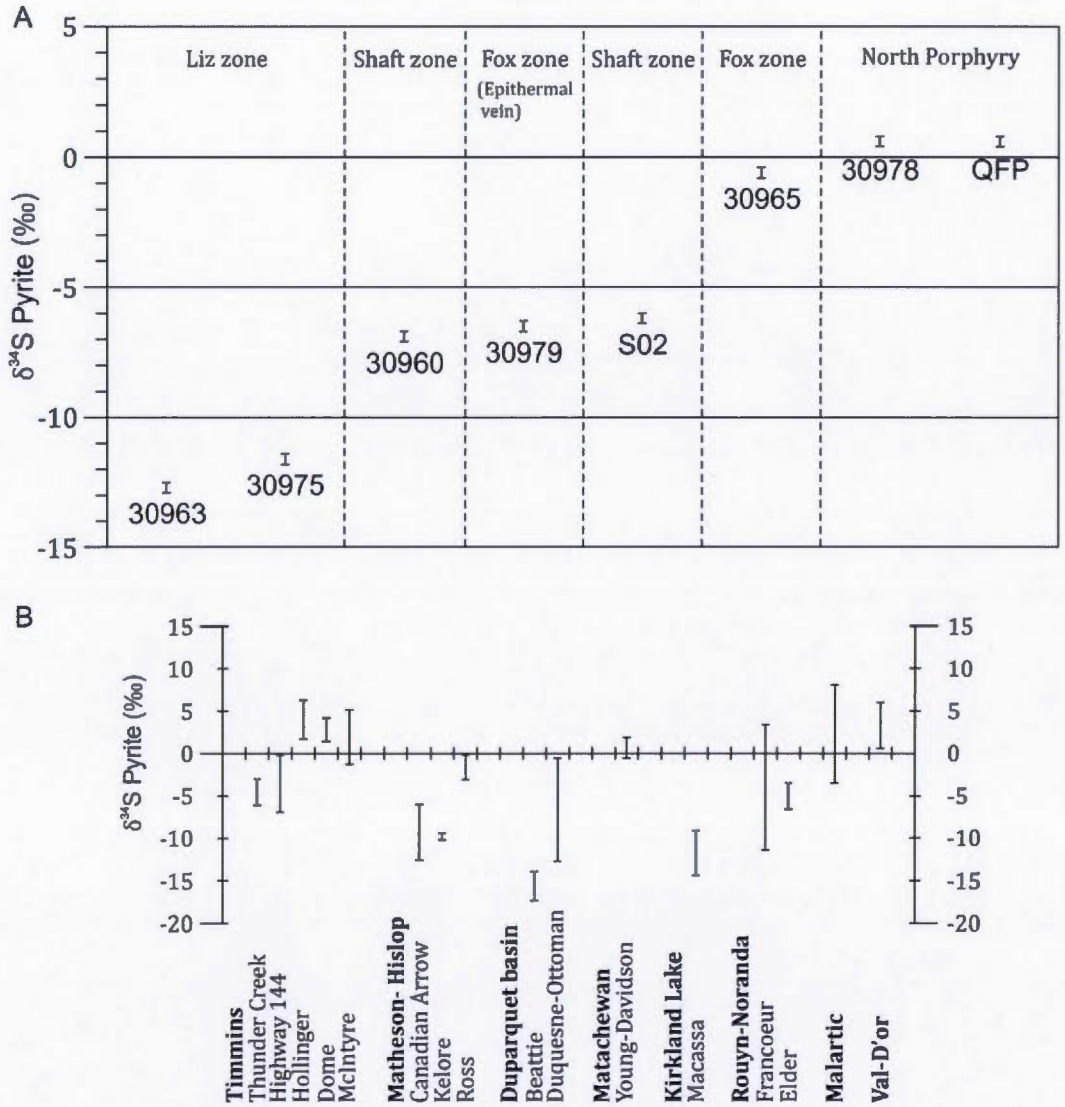

FIGURE 1.17– (A) Sulfur Isotope composition of pyrite in the Liz, Shaft and Fox zones of the Duquesne-Ottoman property. (B) Sulfur isotope composition of pyrite in selected orogenic gold deposits, Abitibi greenstone belt. Data from: Dome, Hollinger, McIntyre and Canadian Arrow from Schwarcz and Rees (1987), Thunder Creek and Highway 144 from Campbell (2014), Kelore, Ross and Macassa mine from Cameron and Hattori (1987), Beattie from Xue *et al.* (2012), Young Davidson from Ryan (2012), Francoeur mine from Couture and Pilote (1993), Elder from Trudel *et al.* (1991), Malartic from Helt *et al.* (2014) and Val-d'Or from Beaudoin and Pitre (2005). Modified and updated from Couture and Pilote (1993).

TABLE 1.1- Chemical composition of the rocks of the DOP.

Sample	30951	30952	30953	30954	30955	30956	30957	30958
Zone	East-Shaft	East-Shaft	East-Shaft	East-Shaft	East-Shaft	East-Shaft	East-Shaft	East-Shaft
Rock-type	Basalt	Rhyolite	Andesite	Basalt	Komatiite	QFP	Basalt	Andesite
SiO_2 (%)	43.47	80.96	44.69	42.65	41.07	65.59	43.15	46.85
Al_2O_3 (%)	11.75	8.49	12.18	10.98	4.64	15.00	11.86	13.67
$Fe_2O_{3(T)}$ (%)	15.56	2.51	8.33	15.36	11.12	2.72	13.41	9.15
MnO (%)	0.18	0.02	0.16	0.23	0.12	0.05	0.19	0.16
MgO (%)	5.11	0.57	6.28	4.62	26.62	1.68	5.87	5.33
CaO (%)	7.29	0.89	9.32	8.15	3.28	2.77	9.87	9.52
Na_2O (%)	1.50	0.29	2.40	2.62	0.02	4.07	1.58	3.91
K_2O (%)	1.05	2.60	1.73	0.88	<0.01	2.45	0.13	0.13
TiO_2 (%)	1.44	0.14	0.60	1.44	0.23	0.34	1.19	0.64
P_2O_5 (%)	0.11	0.01	0.28	0.12	0.02	0.12	0.08	0.24
LOI (%)	13.05	2.77	14.97	13.01	11.63	5.34	11.18	9.78
Total (%)	100.50	99.26	100.90	100.10	98.75	100.10	98.50	99.36
Au (ppb)	<2	14	<2	424	12	47	<2	<2
As (ppm)	4.9	4.5	5.8	4.8	9.8	5.5	4.5	2.3
Br (ppm)	<0.5	<0.5	<0.5	<0.5	<0.5	<0.5	<0.5	<0.5
Cr (ppm)	46	149	397	46	2800	110	129	193
Ir (ppm)	<5	<5	<5	<5	<5	<5	<5	<5
Sb (ppm)	4.2	1.6	2.5	9.2	3.9	1.4	1.5	0.9
Sc (ppm)	37.7	2.5	23.8	34.8	13.7	4.7	36.0	21.4
Se (ppm)	<3	<3	<3	<3	<3	<3	<3	<3
Be (ppm)	<1	2.0	2.0	<1	<1	1.0	<1	<1
V (ppm)	369	18	186	364	100	55	323	193
Ba (ppm)	122	312	250	158	44	710	80	109
Sr (ppm)	98	24	189	196	137	268	147	146
Y (ppm)	30	53	14	30	7	5	23	13
Zr (ppm)	83	290	83	88	24	100	63	81
Co (ppm)	40	4	29	32	101	7	45	32
Ni (ppm)	40	<20	100	20	880	20	70	60
Cu (ppm)	100	10	60	150	70	<10	130	<10
Zn (ppm)	180	30	100	150	140	50	130	90

* The analysis with the symbol « < » have values under the analytical limit of detection.

Sample	30959	30960	30961	30962	30963	30964	30965	30966
Zone	East-Shaft	East-Shaft	East-Shaft	East-Shaft	Liz	Liz	Fox	Fox
Rock-type	Rhyolite	Rhyolite	Basalt	Basalt	Basalt	Basalt	Komatiitic basalt	Komatiitic basalt
SiO_2 (%)	67.48	58.32	44.31	63.84	58.60	46.03	47.10	40.04
Al_2O_3 (%)	10.65	7.34	11.85	12.10	8.87	15.71	6.16	2.61
$Fe_2O_{3(T)}$ (%)	3.75	6.21	15.68	6.76	10.51	8.10	13.78	11.47
MnO (%)	0.06	0.15	0.18	0.13	0.11	0.20	0.24	0.28
MgO (%)	2.23	3.89	5.46	0.69	1.95	3.00	6.66	11.30
CaO (%)	4.18	7.90	6.09	4.96	3.56	7.67	8.88	17.41
Na_2O (%)	0.46	1.39	2.27	2.19	1.01	1.94	2.29	0.02
K_2O (%)	3.10	1.53	0.65	2.14	2.37	3.21	0.15	0.21
TiO_2 (%)	0.16	0.26	1.64	0.73	0.84	0.83	0.15	0.13
P_2O_5 (%)	0.03	0.02	0.13	0.19	0.09	0.10	0.03	0.02
LOI (%)	7.72	13.16	11.06	6.10	10.82	12.31	14.63	15.33
Total (%)	99.80	100.20	99.33	99.82	98.71	99.11	100.10	98.82
Au (ppb)	3550	9660	34	100	5170	557	120	18
As (ppm)	4.4	5.8	7.6	3.8	13.9	13.7	47.8	8.4
Br (ppm)	<0.5	<0.5	<0.5	<0.5	<0.5	<0.5	<0.5	<0.5
Cr (ppm)	35	107	103	43	142	195	888	1310
Ir (ppm)	<5	<5	<5	<5	<5	<5	<5	<5
Sb (ppm)	2.5	2.3	5.8	3.5	15.7	5.5	7.4	5.9
Sc (ppm)	2.8	7.3	38.8	19.9	18.9	25.4	8.7	10.0
Se (ppm)	<3	<3	<3	<3	<3	<3	<3	4.0
Be (ppm)	2.0	<1	<1	1.0	1.0	1.0	<1	<1
V (ppm)	66	53	372	9	72	202	71	61
Ba (ppm)	321	161	119	397	243	486	56	1706
Sr (ppm)	91	136	101	160	88	137	393	666
Y (ppm)	49	48	32	45	15	14	28	3
Zr (ppm)	437	174	98	289	58	68	74	11
Co (ppm)	4	13	41	5	30	49	67	55
Ni (ppm)	<20	<20	70	<20	70	140	420	1210
Cu (ppm)	10	<10	20	<10	50	20	360	20
Zn (ppm)	40	50	100	100	40	70	70	50

* The analysis with the symbol « < » have values under the analytical limit of detection.

Sample	30968	30969	30970	30971	30972	30973	30975	30976
Zone	East-Shaft	East-Shaft	South	South	South	South	Liz	Liz
Rock-type	Rhyolite	Rhyolite	Komatiite	Quartz-monzonite	Rhyolite	Quartz-monzonite	Basalte	Basalt
SiO_2 (%)	86.51	72.49	33.12	63.58	79.84	67.61	38.52	41.58
Al_2O_3 (%)	5.74	10.56	4.21	15.04	8.06	16.01	10.32	12.59
$Fe_2O_{3(T)}$ (%)	1.28	4.56	10.96	3.55	2.89	2.71	13.28	13.62
MnO (%)	0.04	0.05	0.17	0.06	0.03	0.04	0.19	0.24
MgO (%)	0.46	1.10	27.94	1.63	0.41	0.52	4.75	5.02
CaO (%)	0.73	2.70	1.33	2.76	0.92	1.16	8.10	6.84
Na_2O (%)	2.39	4.71	0.02	5.91	4.59	8.90	2.50	0.47
K_2O (%)	0.45	0.02	<0.01	1.95	0.06	0.21	2.01	3.73
TiO_2 (%)	0.08	0.30	0.21	0.49	0.18	0.29	1.19	1.45
P_2O_5 (%)	0.02	0.02	0.01	0.25	0.09	0.17	0.05	0.11
LOI (%)	1.29	2.13	20.00	4.77	2.11	2.49	17.08	14.16
Total (%)	98.99	98.63	97.98	99.97	99.19	100.10	97.98	99.80
Au (ppb)	6	<2	<2	<2	19	16	2110	217
As (ppm)	2.8	4.8	7.7	3.8	10.4	9.2	16.5	10.6
Br (ppm)	<0.5	<0.5	<0.5	<0.5	<0.5	<0.5	<0.5	<0.5
Cr (ppm)	174	199	5340	133	245	99	154	136
Ir (ppm)	<5	<5	<5	<5	<5	<5	<5	<5
Sb (ppm)	1.7	1.1	3.3	5.3	4.2	3.5	18.5	11.7
Sc (ppm)	1.3	7.9	15.8	6.8	2.8	3.8	31.7	40.9
Se (ppm)	<3	<3	<3	<3	<3	<3	<3	<3
Be (ppm)	<1	<1	<1	2.0	<1	<1	1.0	2.0
V (ppm)	14	44	94	69	13	27	252	347
Ba (ppm)	93	18	529	4069	68	497	170	286
Sr (ppm)	39	81	776	653	121	199	177	173
Y (ppm)	45	68	4	16	13	17	21	29
Zr (ppm)	176	299	13	194	101	210	74	88
Co (ppm)	2	7	101	9	14	6	36	44
Ni (ppm)	<20	<20	1400	30	30	<20	100	60
Cu (ppm)	<10	30	<10	90	30	<10	80	360
Zn (ppm)	<30	30	<30	40	50	<30	120	110

* The analysis with the symbol « < » have values under the analytical limit of detection.

Sample	30978	30980
Zone	Fox	South
Rock-type	QFP	Komatiite
SiO_2 (%)	67.80	38.89
Al_2O_3 (%)	15.26	6.87
$Fe_2O_{3(T)}$ (%)	2.60	9.50
MnO (%)	0.02	0.17
MgO (%)	1.21	16.66
CaO (%)	2.42	7.51
Na_2O (%)	3.98	0.03
K_2O (%)	3.21	0.01
TiO_2 (%)	0.34	0.39
P_2O_5 (%)	0.15	0.04
LOI (%)	3.18	18.11
Total (%)	100.20	98.17
Au (ppb)	256	<2
As (ppm)	5.0	4.0
Br (ppm)	<0.5	<0.5
Cr (ppm)	128	1390
Ir (ppm)	<5	<5
Sb (ppm)	7.4	2.2
Sc (ppm)	4.6	21.5
Se (ppm)	<3	<3
Be (ppm)	1.0	<1
V (ppm)	59	147
Ba (ppm)	875	60
Sr (ppm)	378	180
Y (ppm)	6	9
Zr (ppm)	114	26
Co (ppm)	7	66
Ni (ppm)	<20	760
Cu (ppm)	350	50
Zn (ppm)	30	60

* The analysis with the symbol « < » have values under the analytical limit of detection.

Sample	30951	30952	30953	30954	30955	30956	30957	30958
Zone	East-Shaft	East-Shaft	East-Shaft	East-Shaft	East-Shaft	East-Shaft	East-Shaft	East-Shaft
Rock-type	Basalt	Rhyolite	Andesite	Basalt	Komatiite	QFP	Basalt	Andesite
Ga (ppm)	17	12	14	17	6	21	16	17
Ge (ppm)	2	2	<1	1	2	<1	1	<1
Rb (ppm)	25	59	37	20	<2	55	3	3
Nb (ppm)	4	16	4	4	1	3	3	5
Mo (ppm)	<2	17	<2	2	<2	3	<2	<2
Ag (ppm)	<0.5	2.0	<0.5	<0.5	<0.5	<0.5	<0.5	<0.5
In (ppm)	<0.2	<0.2	<0.2	<0.2	<0.2	<0.2	<0.2	<0.2
Sn (ppm)	1	3	2	1	<1	<1	<1	<1
Cs (ppm)	0.6	1.5	1.2	0.6	<0.5	1.4	<0.5	0.6
La (ppm)	4.4	41.2	13.7	4.7	2.5	18.5	3.3	16.4
Ce (ppm)	12.0	92.7	33.5	12.4	5.9	37.8	9.0	35.9
Pr (ppm)	2.0	11.6	5.2	2.1	0.8	4.9	1.5	4.8
Nd (ppm)	10.4	49.0	25.2	10.8	3.4	17.8	7.5	19.6
Sm (ppm)	3.4	10.5	6.7	3.6	0.9	3.2	2.5	4.1
Eu (ppm)	1.1	1.6	1.4	1.2	0.2	0.7	0.9	1.2
Gd (ppm)	4.2	9.3	4.5	4.6	1.1	2.1	3.4	3.4
Tb (ppm)	0.8	1.5	0.5	0.9	0.2	0.2	0.6	0.5
Dy (ppm)	5.3	9.5	2.6	5.6	1.2	1.0	4.3	2.5
Ho (ppm)	1.1	2.1	0.5	1.1	0.3	0.2	0.9	0.5
Er (ppm)	3.3	6.5	1.3	3.4	0.8	0.4	2.8	1.4
Tm (ppm)	0.5	1.0	0.2	0.5	0.1	0.1	0.4	0.2
Yb (ppm)	3.3	7.4	1.4	3.5	0.8	0.4	2.8	1.4
Lu (ppm)	0.6	1.2	0.2	0.6	0.1	0.1	0.5	0.2
Hf (ppm)	2.2	7.4	1.9	2.3	0.5	2.6	1.8	2.1
Ta (ppm)	0.2	1.2	0.2	0.2	<0.1	0.2	0.2	0.2
W (ppm)	<1	1.0	2.0	17.0	<1	2.0	<1	<1
Tl (ppm)	0.1	0.2	0.2	0.1	<0.1	0.3	<0.1	<0.1
Pb (ppm)	<5	<5	<5	<5	<5	<5	<5	<5
Bi (ppm)	<0.4	<0.4	<0.4	<0.4	<0.4	<0.4	<0.4	<0.4
Th (ppm)	0.3	4.8	2.6	0.3	0.2	2.7	0.2	1.8
U (ppm)	<0.1	2.5	1.2	0.1	<0.1	0.9	<0.1	0.5

* The analysis with the symbol « < » have values under the analytical limit of detection.

Sample	30959	30960	30961	30962	30963	30964	30965	30966
Zone	East-Shaft	East-Shaft	East-Shaft	East-Shaft	Liz	Liz	Fox	Fox
Rock-type	Rhyolite	Rhyolite	Basalt	Basalt	Basalt	Basalt	Komatiitic basalt	Komatiitic basalt
Ga (ppm)	18	9	17	19	13	15	11	5
Ge (ppm)	1	<1	1	<1	2	<1	3	6
Rb (ppm)	70	33	16	57	42	73	4	14
Nb (ppm)	22	12	5	15	3	4	7	<1
Mo (ppm)	4	36	<2	3	11	6	4	5
Ag (ppm)	3.2	1.3	<0.5	2.2	0.6	<0.5	<0.5	<0.5
In (ppm)	<0.2	<0.2	<0.2	<0.2	<0.2	<0.2	<0.2	<0.2
Sn (ppm)	4	1	1	3	<1	<1	4	<1
Cs (ppm)	1.6	0.8	<0.5	1.3	1.3	2.9	0.5	2.8
La (ppm)	46.2	22.9	5.0	30.0	32.7	7.1	19.2	1.0
Ce (ppm)	104.0	51.4	13.9	68.5	43.9	16.1	42.8	2.3
Pr (ppm)	14.1	7.1	2.3	9.4	4.3	2.3	5.6	0.3
Nd (ppm)	56.7	29.8	11.8	38.5	14.6	9.8	22.1	1.4
Sm (ppm)	11.8	7.3	3.9	8.4	3.0	2.4	4.8	0.4
Eu (ppm)	1.8	1.4	1.2	1.9	0.9	0.8	0.5	0.2
Gd (ppm)	10.9	8.6	4.9	8.3	3.2	2.6	4.6	0.5
Tb (ppm)	1.8	1.5	0.9	1.3	0.5	0.4	0.8	<0.1
Dy (ppm)	10.3	8.5	6.0	8.0	3.0	2.5	4.7	0.6
Ho (ppm)	2.1	1.7	1.3	1.6	0.6	0.5	1.0	0.1
Er (ppm)	6.2	4.9	3.9	4.9	1.8	1.6	2.8	0.4
Tm (ppm)	1.0	0.7	0.6	0.7	0.3	0.2	0.4	0.1
Yb (ppm)	7.0	4.9	3.9	5.0	1.8	1.7	2.9	0.4
Lu (ppm)	1.2	0.8	0.7	0.9	0.3	0.3	0.5	0.1
Hf (ppm)	11.1	4.6	2.7	6.6	1.6	1.7	2.6	<0.2
Ta (ppm)	1.6	0.8	0.3	0.9	0.1	0.2	0.6	<0.1
W (ppm)	5.0	17.0	7.0	2.0	44.0	3.0	28.0	2.0
Tl (ppm)	0.3	0.2	<0.1	0.2	0.3	0.4	<0.1	0.1
Pb (ppm)	<5	5.0	<5	<5	8.0	<5	<5	6.0
Bi (ppm)	<0.4	<0.4	<0.4	<0.4	<0.4	<0.4	2.3	7.3
Th (ppm)	6.7	2.8	0.4	3.7	0.4	0.6	2.2	<0.1
U (ppm)	2.7	1.1	0.1	1.0	0.8	0.2	0.5	<0.1

* The analysis with the symbol « < » have values under the analytical limit of detection.

Sample	30968	30969	30970	30971	30972	30973	30975	30976
Zone	East-Shaft	East-Shaft	South	South	South	South	Liz	Liz
Rock-type	Rhyolite	Rhyolite	Komatiite	Quartz-monzonite	Rhyolite	Quartz-monzonite	Basalte	Basalt
Ga (ppm)	7	13	5	21	10	19	14	18
Ge (ppm)	1	<1	1	1	<1	<1	<1	1
Rb (ppm)	11	<2	<2	61	<2	5	41	111
Nb (ppm)	10	16	<1	9	6	10	3	4
Mo (ppm)	14	13	<2	7	27	13	3	2
Ag (ppm)	0.9	1.8	<0.5	0.8	<0.5	0.8	<0.5	<0.5
In (ppm)	<0.2	<0.2	<0.2	<0.2	<0.2	<0.2	<0.2	<0.2
Sn (ppm)	<1	4	<1	1	1	<1	<1	<1
Cs (ppm)	<0.5	<0.5	<0.5	2.1	<0.5	<0.5	1.3	2.7
La (ppm)	21.7	32.3	0.6	84.8	34.0	65.9	5.0	4.5
Ce (ppm)	45.9	78.3	1.5	156.0	66.6	132.0	11.7	11.9
Pr (ppm)	6.0	11.2	0.3	19.0	8.0	16.7	1.8	1.9
Nd (ppm)	23.6	46.0	1.2	70.3	30.0	63.6	8.9	9.8
Sm (ppm)	5.4	10.9	0.4	11.1	5.5	10.4	2.9	3.4
Eu (ppm)	0.5	1.8	0.1	2.6	1.1	2.4	0.9	1.0
Gd (ppm)	5.6	10.9	0.6	7.3	4.1	6.9	3.4	4.4
Tb (ppm)	1.0	1.8	0.1	0.7	0.5	0.7	0.6	0.8
Dy (ppm)	7.2	11.2	0.8	3.3	2.5	3.2	4.0	5.4
Ho (ppm)	1.7	2.4	0.2	0.5	0.4	0.5	0.8	1.1
Er (ppm)	5.7	7.2	0.5	1.4	1.2	1.5	2.6	3.4
Tm (ppm)	0.9	1.2	0.1	0.2	0.2	0.2	0.4	0.5
Yb (ppm)	6.1	8.1	0.5	1.2	1.1	1.4	2.6	3.5
Lu (ppm)	1.0	1.4	0.1	0.2	0.2	0.2	0.4	0.6
Hf (ppm)	4.8	7.8	0.3	5.0	2.5	5.1	2.0	2.4
Ta (ppm)	0.8	1.4	<0.1	0.5	0.4	0.4	0.2	0.2
W (ppm)	<1	<1	3.0	8.0	10.0	22.0	63.0	28.0
Tl (ppm)	<0.1	<0.1	<0.1	0.3	<0.1	<0.1	0.3	0.8
Pb (ppm)	<5	<5	<5	5.0	<5	10.0	<5	<5
Bi (ppm)	<0.4	<0.4	<0.4	<0.4	<0.4	<0.4	<0.4	<0.4
Th (ppm)	3.4	4.8	<0.1	9.8	4.6	11.5	0.3	0.3
U (ppm)	0.9	1.2	<0.1	2.3	1.9	3.5	0.4	0.1

* The analysis with the symbol « < » have values under the analytical limit of detection.

Sample	30978	30980
Zone	Fox	South
Rock-type	QFP	Komatiite
Ga (ppm)	22	8
Ge (ppm)	<1	<1
Rb (ppm)	75	<2
Nb (ppm)	3	<1
Mo (ppm)	5	<2
Ag (ppm)	<0.5	<0.5
In (ppm)	<0.2	<0.2
Sn (ppm)	<1	<1
Cs (ppm)	2.0	1.0
La (ppm)	16.5	1.5
Ce (ppm)	35.2	3.4
Pr (ppm)	4.6	0.6
Nd (ppm)	17.7	2.7
Sm (ppm)	3.4	0.9
Eu (ppm)	1.0	0.3
Gd (ppm)	2.5	1.3
Tb (ppm)	0.3	0.2
Dy (ppm)	1.2	1.6
Ho (ppm)	0.2	0.3
Er (ppm)	0.5	1.0
Tm (ppm)	0.1	0.2
Yb (ppm)	0.5	1.0
Lu (ppm)	0.1	0.2
Hf (ppm)	3.1	0.6
Ta (ppm)	0.2	<0.1
W (ppm)	3.0	3.0
Tl (ppm)	0.4	<0.1
Pb (ppm)	15.0	<5
Bi (ppm)	0.5	<0.4
Th (ppm)	2.8	<0.1
U (ppm)	1.1	<0.1

* The analysis with the symbol « < » have values under the analytical limit of detection.

TABLE 1.2- Main characteristics of the three types of mineralization of the DOP.

	Disseminated sulphide	Clusters of sulphides and iron oxides	Epithermal veins
Style of mineralization	Disseminated pyrite	Clusters of Py-Cpy-Hem-Mg	Clusters of polymetallic sulphides
Texture	Replacement and breccia	Replacement and stockwork	Fracture-filling veining
Setting of mineralization	In second-order fault zone	In fault zone adjacent to the North Porphyry	In fractures within the North Porphyry
Major lithological host	Basalts and komatiites	Komatiites	Quartz veins
Alteration	Ferroan dolomite, quartz and sericite	Calcite and hematite	Quartz
Metallic mineral	Py, Cpy, Tt, En, El, Cl, Au-Te, Ag-Te, Au-Ag-Te	Py, Hem, Cpy, Mag, Gn, Co, Bi, Bi-Te, El, Cl, Ag-Te, Au-Ag-Te	Cpy, Py, Sp, Tt, Gn, Cl, Au-Te, Ag-Te, Au-Ag-Te,
Elemental association	As, Mo, W, Sb, Cu, Te, Hg	Cu, As, Ag, W, Sn, Te, Bi, Pb	Cu, Pb, Ag, Zn, As, Sb, Te
Setting of gold	Native gold and electrum in inclusion in Py, in microfractures and along grain boundary	Native gold in inclusion in Py and along grain boundary	Gold telurides in inclusion in Py
Sulphide content	5 % to 10%	10% to 20%	Variable
Iron oxide content	0% to 3%	20% to 25%	None
DOP zone	Liz and Shaft	Fox	Fox, Stringer and 20-20 zones

Abbreviations: Ag-Te = Silver telluride; Au-Ag-Te = Silver and gold telluride; Au-Te = Gold telluride; Bi = Bismuth mineral; Bi-Te = Bismuth telluride; Cl = Coloradoite; Co = Cobalt-bearing mineral; Cpy = Chalcopyrite; El = Electrum; En = Enargite; Gn = Galena; Hem = Hematite; Mag = Magnetite; Py = Pyrite; Sp = Sphalerite; Tt = Tennantite-Tetrahedrite.

TABLE 1.3– Comparison of the DOP (Shaft, Liz and Fox zones), high-sulphidation epithermal deposits and Archean epigenetic gold deposits.

	Duquesne-Ottoman property		High-sulphidation epithermal	Hollinger-MCIntyre	Holloway	Beattie	Malartic	Sigma
	Shaft-Liz	Fox						
Main host rock	**Mafic**-ultramafic metavolcanic rocks	Mafic-**ultramafic** metavolcanic rocks, QFP	Variable	**QFP**, mafic metavolcanic rocks	**Mafic** metavolcanic rocks, metasediment	**Mafic** metavolcanic rocks, alcaline stock	**Metasedimentary** rocks, felsic to intermediary porphyry	**Intermediate** metavolcanic rocks diorite porphyry, FP
Associated magmatism	Intermediate calc-alkaline porphyry, alkaline porphyry		Intermediate calc-alkaline volcanic rocks,	Intermediate calc-alkaline porphyry	——	Alkaline porphyry	Sub-alkaline felsic intrusion	Intermediate calc-alkaline intrusion
Strucural regime	Brittle-ductile transition		——	Brittle to brittle-ductile	Ductile	Brittle-ductile transition	Brittle-ductile	Brittle-ductile
Main alteration	Dol, Ser, Py, Qtz, Chl	Sil, Cal, Hem	Sil (vuggy), clay	Alb, Sil, Ser, Fe-Cb	Alb, Hem, Fe-Cb, Ser	Fe-Cb, Ser, Sil	Kfs, Bt, Cb,Ser, Sil	Chl, Cb, Ser, Alb
Timing of mineralization	Syn- to post- 2689 Ma QFP stock		——	Syn- to post 2673 Ma albitite	Syn- to post 2672 Ma intermineral dyke	Syn- to post 2682 Ma alkaline stock	Syn- to post 2677 Ma alkaline prophyry	Post 2694 Ma FP dykes
Style of mineralization	Disseminated	Disseminated clusters, polly-metallic veins	Stratabound disseminated, stockwerk, breccia	Stockwork Qtz veins, disseminated	Disseminated, Qtz-Cb stockwork	Disseminated, Silicified breccia	Qtz-Cb veinlets, disseminated	Qtz-Chl-Tur veins
Ore mineralogy	Py, Cpy ± Tt, En, Te, Cl	Py, Hem, Cpy, ± Gl, Co, Bi, Te, Cl	Py, Cv-En, Tt, Cpy, El, Mag, Hem, Dg, Sp, Gn	Py, Sp, Cpy, Po, Gn, Te, Bi	Py, Apy, Tt, Cpy, Sp, Hem, Mo	Py, Apy, Gn, Sp, Cpy, En, Tt, Cl, Te	Py, Hem, Te, Sch, Cpy, Gn, Mo, Sp, Bi	Py, Cpy, Po, Sp, Gn, Mo, Te, Bi
Elemental association	**Au**, **Ag**, **As**, Cu, Mo, W, Sb, Te, Hg	**Au**, **Ag**, **Cu**, As, W, Sn, Pb, Sb, Te, Bi	**Au**, **Ag**, As, Cu, Sb, Bi, Hg, Te, Sn, Pb, Mo	**Au**, **Ag**, **Cu**, W, Pb, As, Bi, Te	**Au**, **As**, Cu, W	**Au**, **As**, **Ag**, Pb, Zn, Te, Hg, Mo, Se, Sb, Cu	**Au**, **Ag**, **Bi**, **Te**, Cu, Mo, Pb, Zn, W	**Au**, **Te**, Ag, Cu, Zn, Pb, Mo, Bi
Sulphide $\delta^{34}S$	-12.7‰ to -6.7‰	-6.5‰ to -0.6‰	> 8‰	-1.3‰ to 6.3‰	——	-17.3‰ to -13.9‰	-3.5‰ to 8.1‰	——
References	This study	This study	Jébrak and Marcoux (2008), White and Hedenquist(1995)	Berger (2001), Wood (1991), Schwarcz & Rees (1986)	Robert (2001), Luinstra (2001), Guy (1996)	Bigot & Jébrak (2015), Xue *et al.* (2013	Helt et al. (2014), De Souza *et al.* (2015)	Robert & Brown (1986 a,b), Wong *et al.* (1991)

Abbreviations: Alb= Albite; Ag-Te = Silver telluride; Apy = Arsenopyrite; Au-Ag-Te = Silver gold telluride; Au-Te = Gold telluride; Bi = Bismuth mineral; Bi-Te = Bismuth telluride; Bt=Biotite; Cal=Calcite; Cb=Carbonate; Chl=Chlorite; Cl = Coloradoite; Co = Cobalt-bearing mineral; Cpy = Chalcopyrite; Cv=Cavalerite; Dg=Digerite; Dol=Dolomite; El = Electrum; En = Enargite; Fe Cb= Ferroan carbonate; Gn = Galena; Hem = Hematite; Kfs= K-Feldspar; Mag = Magnetite; Mo = Molybdenite; Po = Pyrrothite; Py = Pyrite, Qtz= Quartz; Sch=Schorl; Ser=Sericite; Sil= Silica; Sp = Sphalerite, Te= Telluride; Tt = Tennantite-Tetrahedrite;Tur=Tourmaline.

CONCLUSION GÉNÉRALE

La cartographie de détail de tranchés, la description de relevés de forage et les études géochimiques et minéralogiques ont avancé la compréhension métallogénique de la propriété Duquesne-Ottoman. Deux phases hydrothermales distinctes ont été identifiées. Associée à la zone Fox, la première phase aurifère est localisée au contact entre un large massif porphyrique calco-alcalin et les roches volcaniques de la Formation de Lanaudière. La zone Fox est associée à une altération à quartz-calcite-hématite, à des veines épithermales et à une minéralisation aurifère à pyrite, hématite, magnétite et chalcopyrite, ainsi que de faibles proportions de tellurures et minéraux de bismuth et cobalt. L'or visible est observé en inclusions et dans le remplissage de fractures de la pyrite. L'étude minéralogique et géochimique indique un gain en SiO_2, CO_2, S, Cu, Au, Ag et Te, avec des gains mineurs en Pb, Zn, Bi et Co. La seconde phase aurifère, localisée dans les zones Shaft et Liz, est contrôlée par des failles secondaires est-ouest coupant toutes lithologies. Elle est caractérisée par un assemblage d'altération à carbonate de fer, séricite et quartz, ainsi que par une minéralisation en pyrite avec de la chalcopyrite et de faibles proportions de tellurures et sulfosels en traces. Cette phase d'altération montre des gains notables en CO_2, K_2O, S, Mo, W, Sb, As, Au et de légers gain en Te, Ag, Hg and Ba, avec une perte en Sn. La séquence paragenétique de cette phase montre une évolution des sulfures et de l'or en plusieurs étapes. Plusieurs pyrites ont une première génération poreuse enveloppée de plusieurs surcroissances. Ces pyrites montrent une zonation géochimique distincte et un cœur enrichie en Au, Ag et Te. Les valeurs isotopiques $\delta^{34}S$ de pyrites de la propriété sont négatives, de -12,7 à -0,6 ± 0,2 ‰. Les relations de recoupement observées indiquent que la minéralisation postdate la mise en place des intrusifs calco-alcalins datées à

2689 ± 3 Ma. La différente nature de ces deux phases hydrothermales est interprétée comme le résultat d'une première phase épithermale acide à laquelle se superpose un système orogénique à la transition épizonale-mézozonale. Plusieurs caractéristiques de la propriété Duquesne-Ottoman sont similaires à plusieurs gisements orogéniques du sud de la Sous-province de l'Abitibi, particulièrement le gisement Beattie.

Cette étude a progressé la compréhension de la géologie et métallogénie de la propriété Duquesne-Ottoman. Certains éléments présentés dans ce travail, tel que les analyses isotopiques du soufre dans les pyrites et la cartographie chimique des pyrites, apportent une nouvelle approche à l'étude des minéralisations et ouvre sur d'avantages d'options pour l'élaboration d'interprétations métallogéniques pour le secteur minier de Duparquet. Toutefois, certains aspects restent à être approfondis tels que l'étendu des phases hydrothermales à l'échelle de la propriété et de la région de Duparquet, la nature des fluides hydrothermaux impliqués, la nature de la précipitation de l'or dans la pyrite poreuse G2, l'âge exacte de la déposition de l'or et le lien génétique potentiel entre les minéralisations et les syénites de la propriété.

ANNEXE A

LOCALISATION DES ÉCHANTILLONS ET PHOTOS

Les échantillons et les photographies présentés dans ce travail sont localisés dans cette section afin de faciliter l'accès à l'information.

TABLE 1- Synthèse de la localisation des échantillons et des photographies .

Objet	#	Zone	Description	Localisation
Échantillon	30951	East-Shaft	Forage	DO-11-40; 7.25 à 7.45m
Échantillon	30952	East-Shaft	Forage	DO-11-40; 11.55 à 12.00m
Échantillon	30953	East-Shaft	Forage	DO-11-40; 17.40 À 17.60m
Échantillon	30954	East-Shaft	Forage	DO-11-40; 45.45 à 45.85
Échantillon	30955	East-Shaft	Forage	DO-11-40; 60.05 à 60.25m
Échantillon	30956	East-Shaft	Forage	DO-11-40; 80.35 à 80.75m
Échantillon	30957	East-Shaft	Forage	DO-11-51; 26.20 À 26.40m
Échantillon	30958	East-Shaft	Forage	DO-11-51; 29.25 à 29.45m
Échantillon	30959	East-Shaft	Forage	DO-11-51; 74.10 à 70.30m et 70.50 à 70.70m
Échantillon	30960	East-Shaft	Forage	DO-11-51; 72.15 à 72.4m
Échantillon	30961	East-Shaft	Forage	DO-11-51; 80.85 à 81.00m et 81.05 à 81.30m
Échantillon	30962	East-Shaft	Forage	DQ-04-22; 931.10 À 931.50m
Échantillon	30963	Liz	Forage	DQ-04-22; 929.75 À 930.15m
Échantillon	30964	Liz	Forage	DQ-04-22; 934.70 à 935.10m
Échantillon	30965	Fox	Forage	DQ-04-22;1038.40 à 1038.80m
Échantillon	30966	Fox	Forage	DQ-04-22; 1044.75 à 1045.15m
Échantillon	30968	East-Shaft	Décapage	Voir Annexe A, Fig. 1
Échantillon	30969	East-Shaft	Décapage	Voir Annexe A, Fig. 1
Échantillon	30970	South	Décapage	Non-disponible
Échantillon	30971	South	Décapage	Voir Annexe A, Fig. 2
Échantillon	30972	South	Décapage	Voir Annexe A, Fig. 2
Échantillon	30973	South	Décapage	Voir Annexe A, Fig. 2
Échantillon	30975	Liz	Forage	DO-12-71; 347.10 à 347.50m
Échantillon	30976	Liz	Forage	DO-11-73;191.95 à 192.20m et 192.30 à 192.45m
Échantillon	30978	Fox	Forage	DO-11-23; 995.10 à 995.50m
Échantillon	30979	Fox	Forage	DO-11-23;993.80 à 994.10m
Échantillon	30980	South	Décapage	Voir Annexe A, Fig. 2

Objet	#	Zone	Description	Localisation
Échantillon	S01	East-Shaft	Décapage	Voir Annexe A, Fig. 1
Échantillon	S02	East-Shaft	Décapage	Voir Annexe A, Fig. 1
Échantillon	S03	East-Shaft	Décapage	Voir Annexe A, Fig. 1
Échantillon	S04	East-Shaft	Décapage	Voir Annexe A, Fig. 1
Photographie	Fig. 8A	East-Shaft	Décapage	Voir Annexe A, Fig. 1
Photographie	Fig. 8B	East-Shaft	Décapage	Voir Annexe A, Fig. 1
Photographie	Fig. 8C	Shaft	Forage	DO-11-40; 66.45m
Photographie	Fig. 8D	20-20	Décapage	Voir Fig. 4, Zone 20-20 breccia
Photographie	Fig. 8E	Liz	Forage	DQ-04-22; 609.50m
Photographie	Fig. 8F	ND	Affleurement	Non-disponible
Photographie	Fig. 11A	Shaft	Échantillon	30951
Photographie	Fig. 11B	Liz	Forage	DO-12-71; 346m
Photographie	Fig. 11C	Shaft	Forage	DO-11-51; 76.15 à 76.2m
Photographie	Fig. 11D	East-Shaft	Décapage	Voir Annexe A, Fig. 1
Photographie	Fig. 11E	Fox	Forage	DQ-04-22; 1037.5 à 1046.05m
Photographie	Fig. 11F	Fox	Forage	DQ-04-22; 1046.05 à 1048.30m
Photographie	Fig. 11G	Fox	Forage	DQ-04-22; 1048.30 à 1048.80m
Photographie	Fig. 11H	East-Shaft	Décapage	Voir Annexe A, Fig. 1
Photographie	Fig. 15A	Liz	Lame mince	30963
Photographie	Fig. 15B	Liz	Lame mince	30963
Photographie	Fig. 15C	Shaft	Lame mince	30954
Photographie	Fig. 15D	Fox	Lame mince	30966
Photographie	Fig. 15E	Liz	Lame mince	30963
Photographie	Fig. 15F	Liz	Lame mince	30963
Photographie	Fig. 15G	Liz	Lame mince	30975
Photographie	Fig. 15H	Liz	Lame mince	30975
Photographie	Fig. 15I	Shaft	Lame mince	30954
Photographie	Fig. 15J	Shaft	Lame mince	30960
Photographie	Fig. 16A	Fox	Lame mince	30966
Photographie	Fig. 16B	Fox	Lame mince	30966
Photographie	Fig. 16C	Fox	Lame mince	30965
Photographie	Fig. 16D	Fox	Lame mince	30965
Photographie	Fig. 16E	Fox	Lame mince	30965
Photographie	Fig. 16F	Fox	Lame mince	30965
Photographie	M63.3	Liz	Lame mince	30963
Photographie	M63.2	Liz	Lame mince	30963

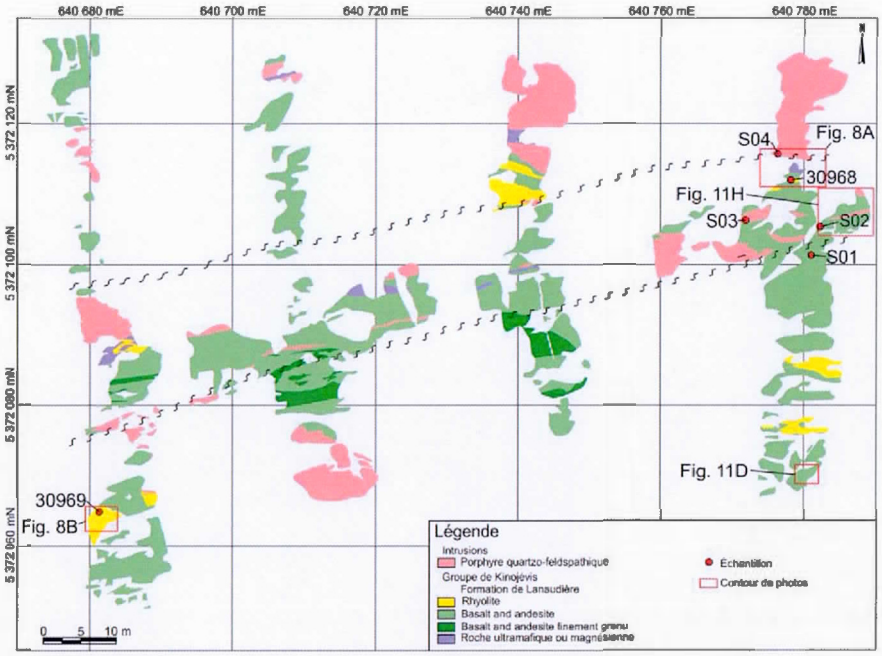

FIGURE 1- Carte géologique des décapages East-Shaft répertoriant la localisation d'échantillons et photographies.

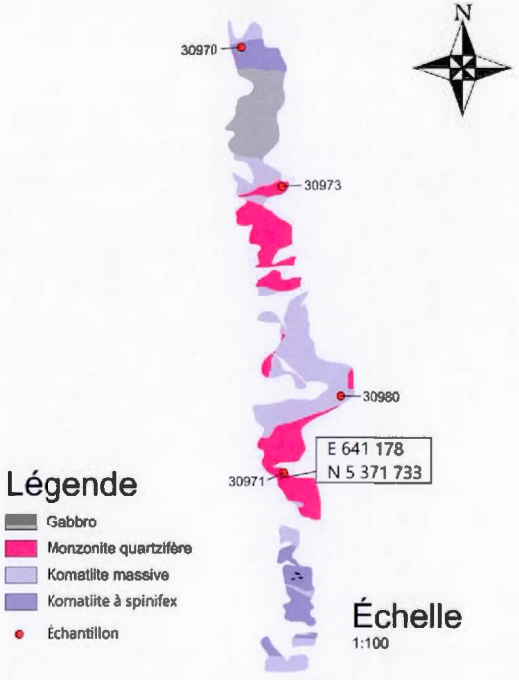

FIGURE 2- Carte géologique du décapage South #3 répertoriant la localisation d'échantillons et photographies.

ANNEXE B
BILAN DE MASSE

Méthodologie

Le calcul de bilan de masse permet de discerner la présence d'éléments majeurs ou traces reflétant une signature particulière au système minéralisateur d'origine hydrothermale de la propriété Duquesne-Ottoman. Les gains et pertes de ces éléments ont été calculés par la méthode du diagramme isochon (Grant, 2005). Pour ce faire, il faut définir un droite isochon à partir d'élément immobiles (ex. Al_2O_3, Zr, TiO_2) et comparer la position des analyses géochimiques d'échantillons frais et altérés par rapport à cette droite. Sept échantillons altérés et minéralisés ont été analysés sur la propriété Duquesne-Ottoman, trois proviennent de la zone Shaft (30954, 30959 et 30960) et quatre proviennent de la zone Liz (30963, 30964, 30975 et 30976). L'altération carbonate de fer-séricite-quartz correspond pour l'ensemble des échantillons au faciès proximal de l'altération lié à la minéralisation. Le tableau 1 résume l'information pourchaque calcul effectué, soit les échantillons utilisés, la nature du protolithe et les éléments immobiles utilisés. Le test d'immobilité est présenté en figure 1 alors que les diagrammes d'isochon sont présentés en figure 2.

TABLE 1- Synthèse des informations relatives aux calculs de bilan de masse

ID	Zone	Échantillon altéré	Précurseur (s)	Protolithe	Altération	Au (ppb)	Éléments immobiles
1	East-Shaft / Transitionel	30954	30951	Basalte	Dol-Qtz-Ser	424	Al_2O_3 et Zr
2	East-Shaft / Proximal	30959	30952	Rhyolite	Qtz-Ser	3550	Al_2O_3 et Zr
3	East-Shaft / Proximal	30960	30952	Rhyolite	Dol-Qtz-Ser	9660	Al_2O_3 et Zr
4	Liz / Proximal	30963	30953-30958	Basalte-Andésite	Dol-Qtz-Ser	5170	Al_2O_3 et Zr
5	Liz / Proximal	30964	30953-30958	Basalte-Andésite	Dol-Qtz-Ser	557	Al_2O_3 et Zr
6	Liz / Proximal	30975	30951	Basalte	Dol-Qtz-Ser	2110	Al_2O_3 et Zr
7	Liz / Proximal	30976	30951	Basalte	Dol-Qtz-Ser	217	Al_2O_3 et Zr

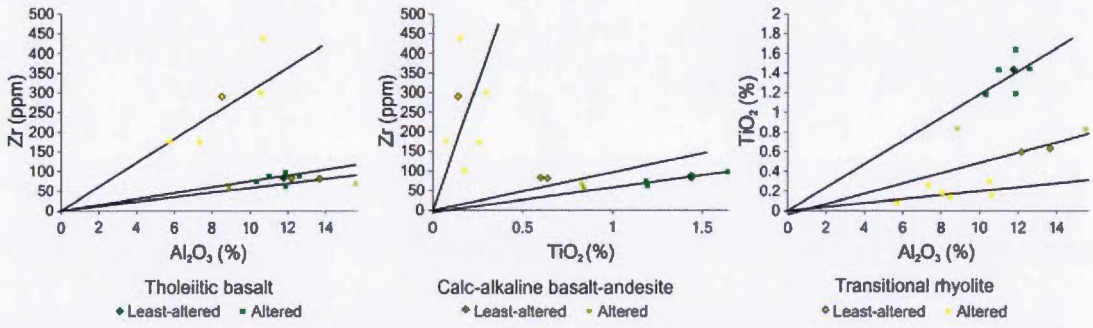

FIGURE 1- Diagrammes binaires testant l'immobilité de Zr et Al_2O_3 en fonction du TiO_2.

30954

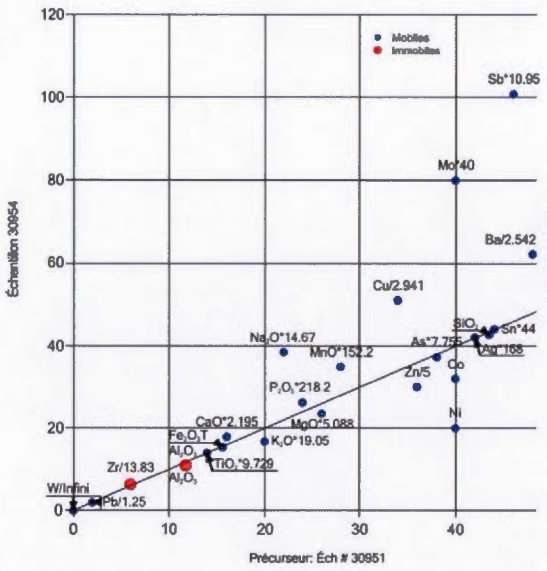

30959

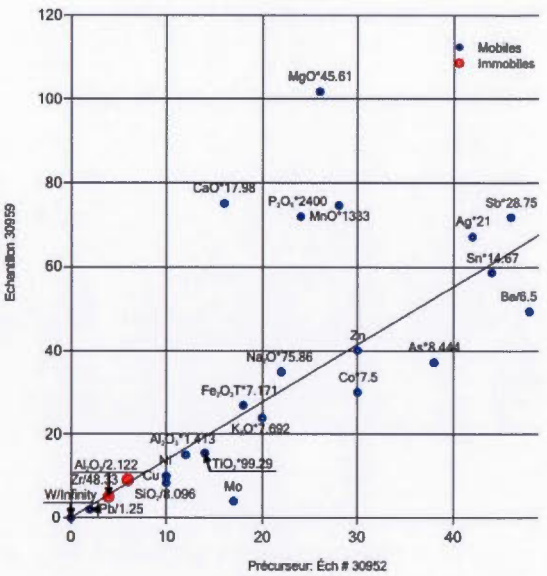

30960

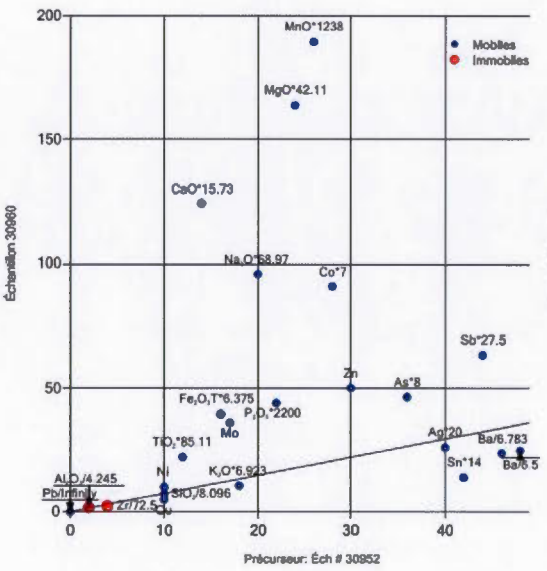

30963

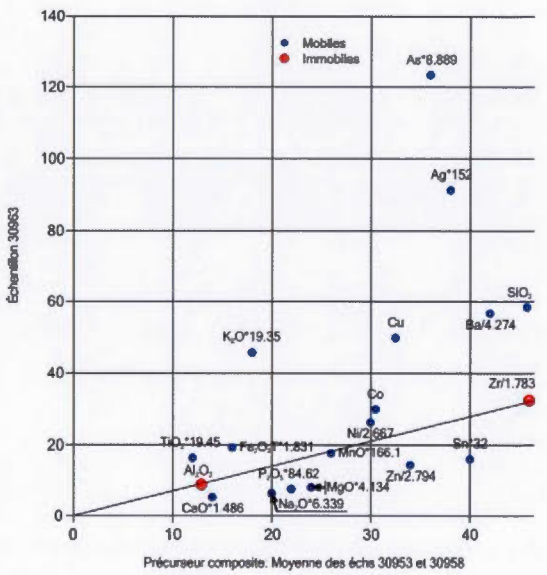

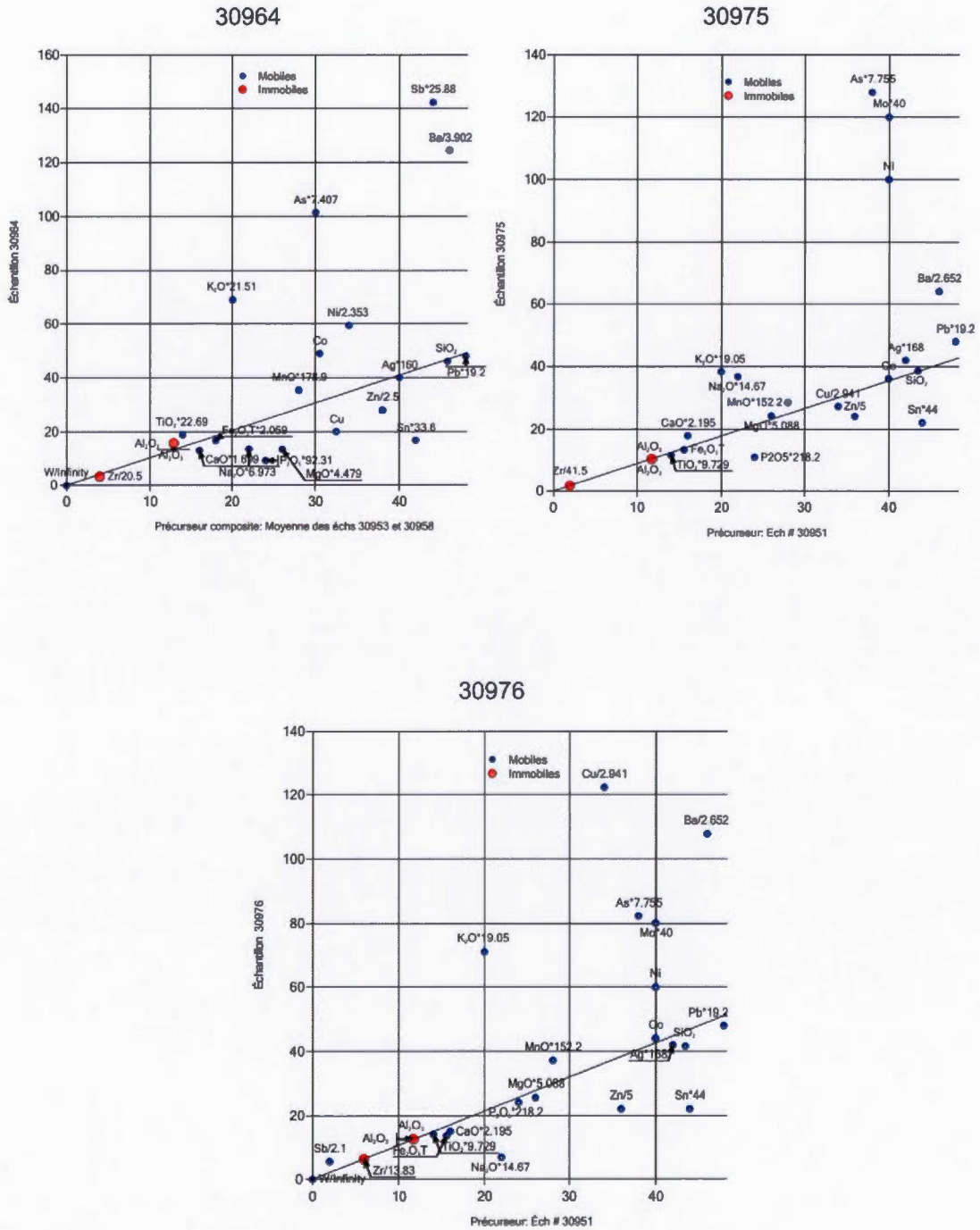

FIGURE 2- Diagrammes isochons des calculs de bilan de masse effectués respectivement sur les échantillons 30954, 30959, 30960, 30963, 30964, 30975 et 30976.

ANNEXE C

CARTOGRAPHIE GÉOCHIMIQUE DE PYRITES

TABLE 1- Synthèse d'information relative à la cartographie géochimique des pyrites de la propriété Duquesne-Ottoman.

# Pyrite	Échantillon	Zones	Type de minéralisation
M60-1	30960	Shaft	Sulfures disséminés
M60.3	30960	Shaft	Sulfures disséminés
M60.4	30960	Shaft	Sulfures disséminés
M63.1	30963	Liz	Sulfures disséminés
M63.2	30963	Liz	Sulfures disséminés
M65.1	30965	Fox	Amas de sulfures et d'oxydes de fer
M78.1	30978	Fox	Veines polymétalliques
M78.2	30978	Fox	Veines polymétalliques

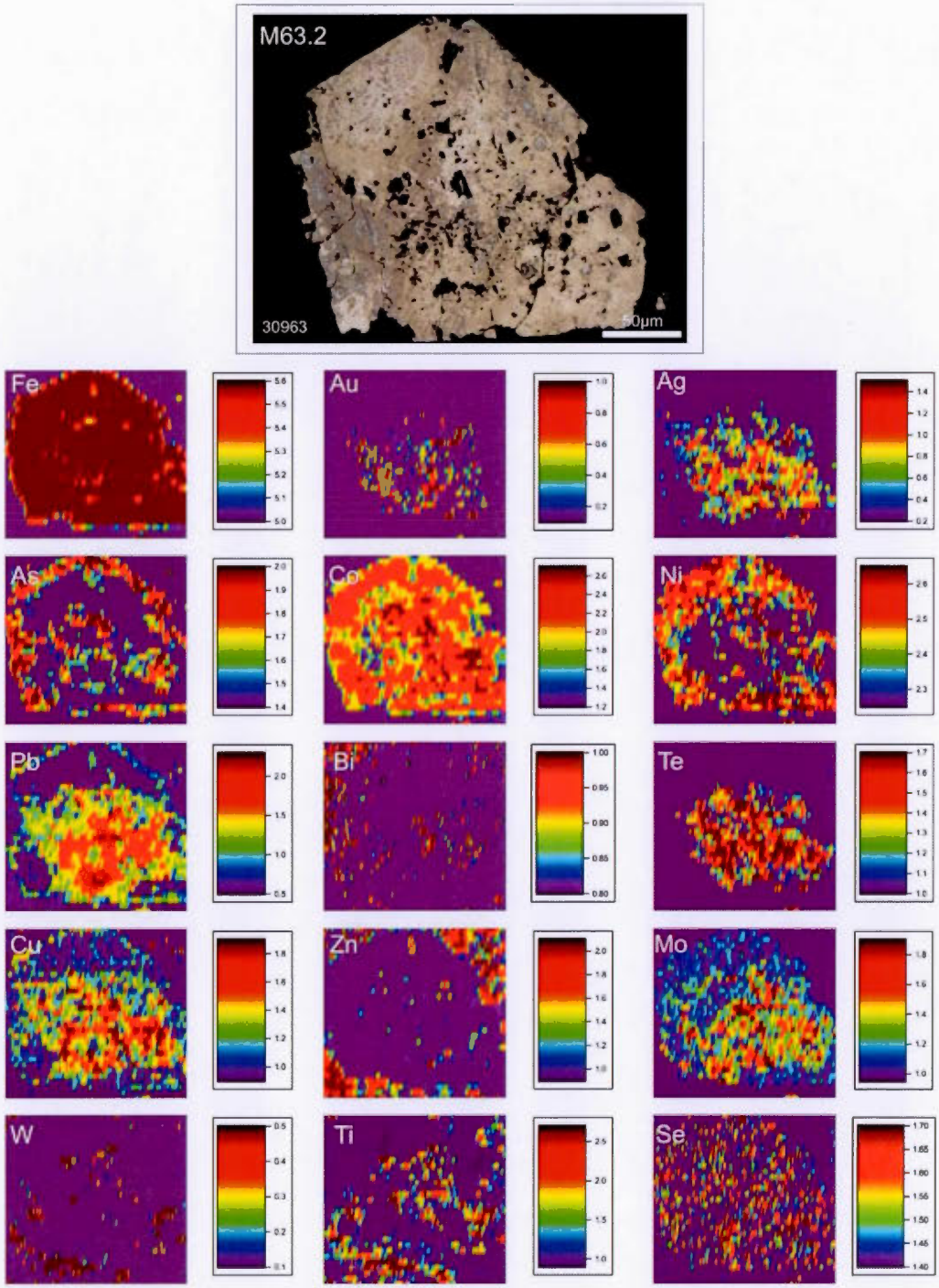

FIGURE 1- Cartographie géochimique de la pyrite M63.2 provenant de la zone Liz.

APPENDICE A

MÉTHODE ANALYTIQUE POUR L'ANALYSE MICROSTRUCTURALE DE LA DÉFORMATION

Introduction

Les cisaillements aurifères filoniens associés aux terrains métamorphiques surnommés « orogéniques » ou « mésothermaux » ont été caractérisés sous maints aspects. Outre la définition des contrôles pétrologiques et minéralogiques, l'étude structurale est un rouage important de la détermination de ce type de gîte. La classification des gîtes d'or hydrothermaux est effectuée en contexte orogénique en fonction de la distribution crustale et du faciès métamorphique (Gebre-Marian *et al.*, 1995; Groves *et al.*, 1998; Goldfarb *et al.*, 2005). La transition ductile-fragile est considérée favorable à ce type de minéralisation (Goldfarb *et al.*, 2005), car les fluides hydrothermaux générés en régime ductile migrent au moyen de la plomberie structural vers cette transition et concentrent certains minéraux d'intérêt économique tel que l'or.

L'analyse microtectonique est un outil efficace pour repérer les mécanismes de déformation et les indicateurs cinématiques associés à la déformation des roches de zone de cisaillement. Sous la forme d'une brève étude bibliographique et d'une expérimentation, les objectifs de ce rapport sont de répertorier les mécanismes de déformation et de définir les régimes structuraux associés à chaque échantillon prélevé au sein du cisaillement aurifère de la propriété Duquesne-Ottoman.

Méthodologie

Analyse microtectonique

Plusieurs échantillons orientés ont été prélevés au sein du cisaillement de l'affleurement #4 de la zone East-Shaft sur la propriété Duquesne-Ottoman. Deux lithologies ont été prélevées, des basaltes et des porphyres quartzo-

feldspathiques (QFP). Ces lithologies ont été coupées et préparées au laboratoire de l'Université du Québec à Montréal et envoyés au laboratoire Vancouver GeoTech Labs pour être préparés en lame mince. Ils sont caractérisés à partir des mécanismes de déformation élaborés dans Passchier et Trouw (1996) et de la description de l'évolution de la déformation d'agrégat feldspathique de Tullis et Yund (1987, 1991). Puisqu'ils réagissent à la déformation de façon similaire, les plagioclases et feldspaths alcalins sont regroupés sous le groupe des feldspaths. Les feldspaths ont été étudiés au moyen d'un microscope optique de type Leica possédant des oculaires de 5x, 10x, 50x et 100x et une caméra.

Une marge d'erreur existe car les microstructures cataclastiques observées en microscopie optique sont similaires à celles produites par le fluage de dislocation (Tullis et Yund, 1987). Il ne sera donc pas possible d'affirmer que les microstructures seront d'ordre fragile ou ductile exclusivement. Toutefois, la corrélation de plusieurs processus proposés dans cette méthodologie permettra d'améliorer cette imprécision instrumentale.

Quatre échantillons orientés (S01, S02, S03 et S04) ont été prélevés sur le décapage #4 de la zone East-Shaft (Fig. 1). Deux lames minces ont été faites pour chacun de ces échantillons selon deux plans par rapport au plan de cisaillement. La section est parallèle à la schistosité et à la linéation. Le plan est parallèle à la schistosité et perpendiculaire à la linéation.

Pour identifier le régime de déformation de la zone de cisaillement, les observations se concentreront sur le mécanisme de déformation principal visible en microscopie optique et sur l'état de déformation du quartz et des feldspaths. Ces deux minéraux se trouvent dans les échantillons prélevés. Afin d'éviter toute confusion possible avec les faciès d'altération, les observations portent principalement sur les phénocristaux de quartz et feldspath

micrométriques observés dans les lithologies cisaillées. La texture porphyrique de ces deux minéraux souligne leur origine magmatique et servira de comparaison pour les observations effectuées lors de cette méthodologie.

Résultats

D'ordre général, l'ensemble des échantillons observés en lames minces présente des fractures intracristallines, des traces de fragmentation mécanique et, par endroits, des gouges d'abrasion. Ces éléments sont coupés par une série de fractures continues, nettes et minces associées à un épisode de déformation fragile tardif.

Le basalte est folié et les textures primaires sont fortement oblitérées par l'altération en carbonate et séricite. On distingue aussi un clivage de crénulation bien développé et marqué par la disposition de la séricite. Les fractures sont fines, nettes et distribuées dans l'ensemble de l'unité. Les phénocristaux de quartz sont d'ordre micrométrique (50-250 μm) et présentent une extinction ondulante. Ils sont caractérisés par une fracturation intracristallines et des bordures arrondies. On n'observe aucun phénocristal de feldspath.

Le porphyre quartzo-feldspathique est peu à légèrement foliée et ne semble pas avoir d'orientation préférentielle des grains de la matrice. On distingue un clivage de crénulation et des zones de failles minces, nettes, en réseaux anastomosés et de type fragile. Il est possible d'observer une rotation de certains fragments et des zones de broyage. On observe dans cette unité de nombreux phénocristaux de quartz et de feldspath. Les feldspaths, de taille millimétrique, sont très altérés en séricite et sont identifiables de par leurs macles polysynthétiques. Ils sont abondamment fracturés. Ils sont découpés en losanges et/ou allongés selon la foliation. À un grossissement de 50x, certains cristaux semblent plissés de manière ductile. Lorsqu'on augmente le

grossissement à 200x ou 500x, on peut observer deux types de déformation. La première est la microfracturation, déplaçant les macles polysynthétiques le long de plans de failles, alors que la deuxième semble être un plissement ductile. Toutefois, tel que mentionné plus haut, seules des observations au TEM pourraient le confirmer. Les grains de quartz de taille centimétrique sont étirés selon la linéation minérale. En microscopie, cette déformation semble être principalement due à de la fracturation. On observe aussi une extinction ondulante de type irrégulière à lisse. Des lamelles de déformation sont aussi observées sur un grain. Le processus de recristallisation du quartz, si présent, est à trouver. L'ensemble de ces observations est présenté dans les planches photo 1 et 2.

Discussion

La description des roches observées permet de classer le cisaillement des unités porphyriques quartzo-feldspathiques dans le régime fragile de fluage cataclastique. Ainsi, les conditions de température et pression minimales interprétées sont de 300°C et 500 MPa, respectivement, selon les expériences sur la déformation des feldspaths de Tullis et Yund (1991). Ainsi, la limite supérieure de la température se situe à environ 600°C. Les lamelles de déformation observées sur un grain de quartz permettent de placer la limite supérieure de la pression à 420 MPa (Passhier et Trouw, 2005). Pour ce qui est de la déformation des unités basaltiques, le clivage de crénulation et la foliation bien enregistrée sur l'ensemble des échantillons soulèvent un caractère plus ductile pour les mêmes intervalles de température et pression. Or, il est évident qu'il faut prendre en compte la nature pétrologique du corps déformé lorsque l'on cherche à caractériser le régime structural des zones de faille ou de cisaillement. Les caractéristiques microscopiques de l'ensemble des unités

felsiques et mafiques observées dans le cisaillement indique un régime crustal ductile-cassant.

Cette méthodologie avait pour objectif d'explorer les racines des processus de déformation des matériaux crustaux et d'en appliquer les principes. À partir d'une revue bibliographique, les régimes fragiles et ductiles ainsi que leurs mécanismes de déformation ont été définis. Ces éléments ont été appliqués à la réalité du cisaillement aurifère de la propriété Duquesne-Ottoman. Les observations microscopiques se sont concentrées sur l'état de déformation des lithologies présentes et des phénocristaux porphyriques de feldspath et de quartz. Le but était de circonscrire précisément le régime structural pour en déduire les conditions de formation du cisaillement. Selon l'ensemble des évidences, les porphyres quartzo-feldspathiques de cette zone de cisaillement sont dominée par une déformation fragile. Les basaltes, plus riches en minéraux ferromagnésiens et moins résistant à la déformation, vont être au moins partiellement recristallisées et déformées de façon ductile. Donc, ces roches mafiques représente les caractéristiques d'une mylonite.

Toutefois, la catégorisation absolue des régimes structuraux et des roches déformées, quoique claire en théorie, se nuance par l'observation de la zone de cisaillement. La catégorisation tentée dans cette méthodologie soulève plus de questions que de réponses. À quelle proportion de déformation fragile ou ductile doit-on trancher pour classer une roche déformée? Comment est-il possible d'établir une proportion entre les éléments de classification qui possède une histoire géologique complexe. En somme, quoiqu'indicative de la nature du cisaillement, cette méthodologie comporte de fortes imprécisions sur plusieurs points tels que : (1) les limites d'observation microscopiques; (2) l'échelle d'observation; (3) le bagage historique du cisaillement; (4) l'interprétation des

conditions physiques de formation du cisaillement et; (5) l'analyse de roches qui montrent une distribution minéralogique du quartz et feldspath bimodale.

L'instrumentation utilisée ne peut répondre aux besoins d'une classification absolue. Comme mentionné dans la revue bibliographique, les mécanismes de déformation fragiles et ductiles s'articulent principalement au niveau de l'échelle nanométrique. L'observation microscopique des effets de ces mécanismes est alors insuffisamment précise. De plus, l'imprécision accroit car les microstructures cataclastiques observées à l'échelle microscopique sont similaires à celles produites par le fluage de dislocation (Tullis et Yund, 1987). Il est noté qu'un plissement ductile d'une certaine échelle peut être le produit de mécanisme de fracturation fragile de plus 21

Conclusion

Cette méthodologie a pour but de caractériser les processus de déformations et les régimes structuraux des échantillons étudiés. L'état de déformation du quartz et des feldspaths, dans les unités porphyriques quartzo-feldspathiques ainsi que la répartition des fractures a permis de classer cette roches comme une cataclastite appartenant à la fin du régime fragile et probablement au début de la transition ductile-fragile. Pour ce qui est des unités basaltiques, ils présentent une déformation ductile et correspondent à une mylonite appartenant au régime ductile. Considérant l'ensemble de ces observations, le cisaillement appartient au régime crustal ductile-cassant. Toutefois, certaines évidences sont impossibles à observer à l'échelle micrométrique. Afin de déterminer si le plissement des feldspaths est d'ordre ductile ou fragile, une observation au microscope à transmission électronique des échantillons serait déterminante. De plus, des intervalles de conditions de température et de pression ont été estimées, soit entre 300 et 600°C et ≥ 500

MPa. Ainsi, s'il y a effectivement recristallisation, le paléopiézomètre expérimentale proposé par certains auteurs (Bishop 1996; Stipp et Tullis 2003; Twiss 1977) sur le quartz pourrait préciser les conditions de pression. Des études d'assemblage minéralogiques et pétrologiques classiques pourraient aussi avancer l'étude des conditions de pression et température.

PLANCHE PHOTO 1- Éléments d'observation microscopique de l'évolution de la déformation des encaissants et de la déformation du quartz

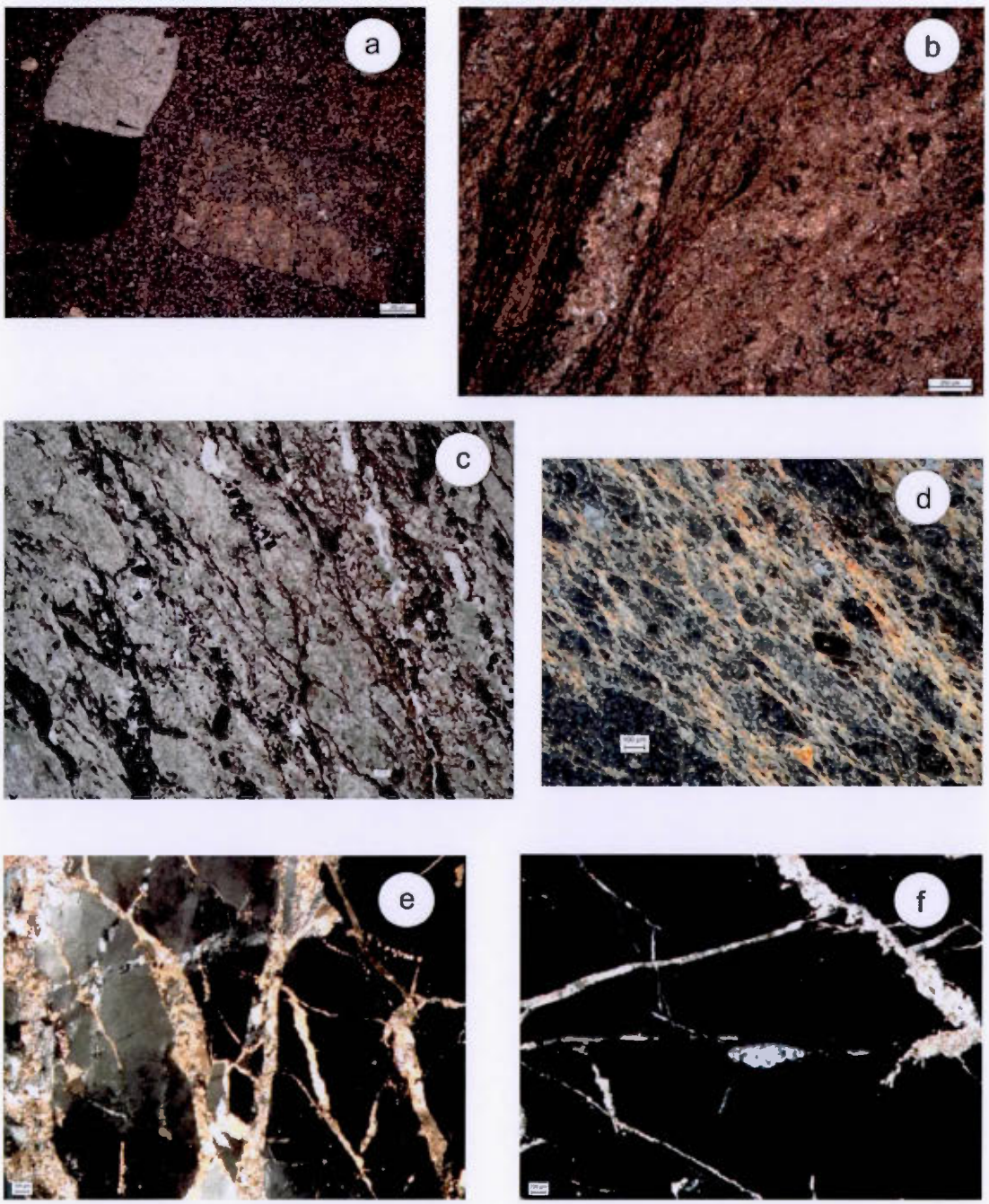

Descriptif de la planche de photo 1

a) Grains de quartz et de feldspath non-déformés de l'encaissant porphyrique quartzo-feldspathiques. Le feldspath est fortement séricitisé. La longueur des grains est d'environ 1-2mm. Observation en lumière polarisée non-analysée.

b) Zone de faille anastomosée locale au sein de métabasalte peu déformé. Observation en lumière polarisée non-analysée.

c) Failles anastomosées distribuées au sein de métabasalte déformé. Foliation faiblement imprimée. Observation en lumière polarisée non-analysée.

d) Foliation pénétrative irrégulière marquée par la disposition subparallèle de la séricite. Observation en lumière polarisée analysée.

e) Portion d'un grain de quartz centimétrique fracturé et à extinction ondulante lissée. Observation en lumière polarisée analysée.

f) Portion d'un grain de quartz millimétrique possédant une texture fortement apparentée aux lamelles de déformation du quartz. Observation en lumière polarisée analysée.

PLANCHE PHOTO 2- Éléments d'observation microscopique de la déformation des feldspaths.

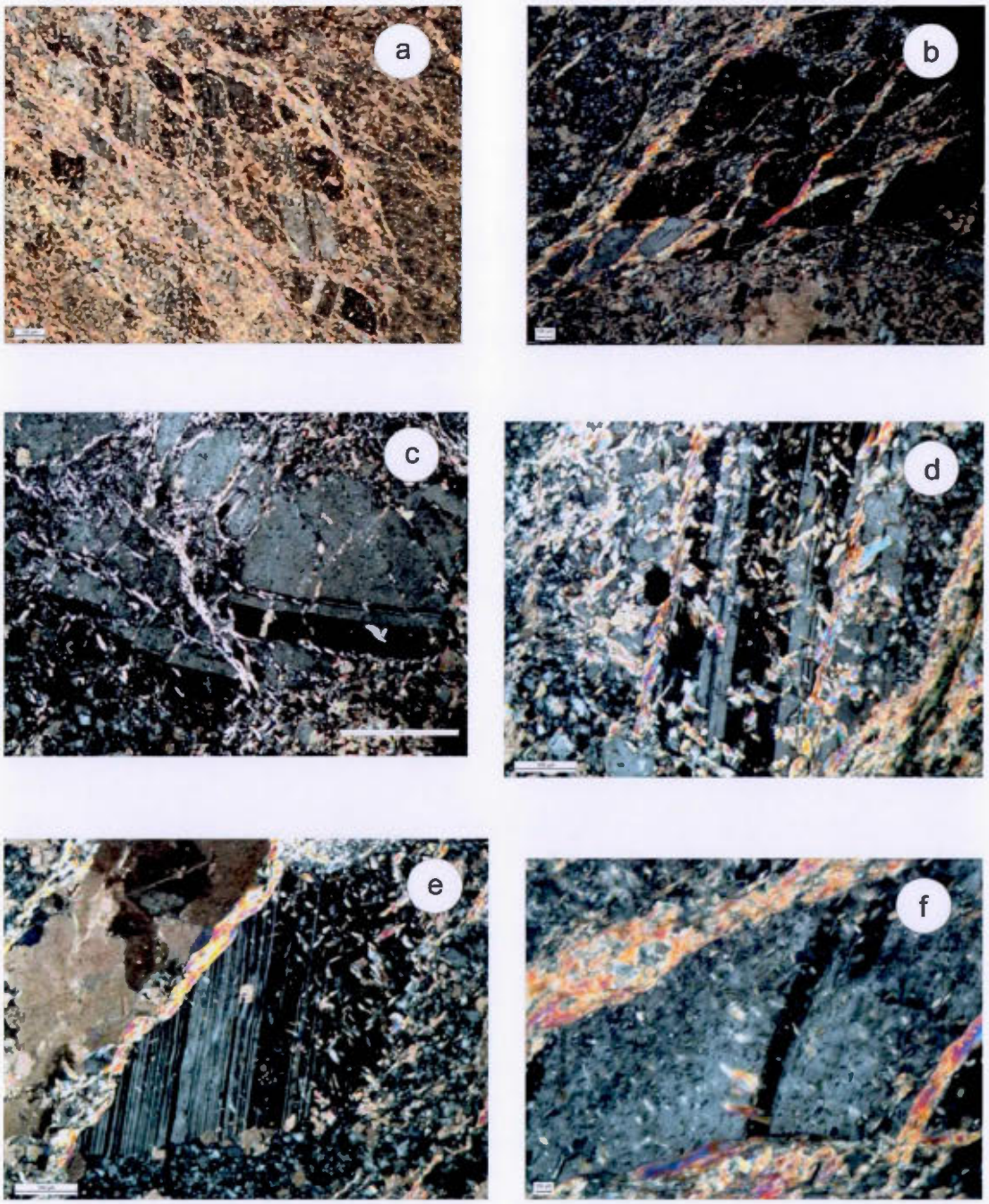

Descriptif de la planche de photo 2

a) Foliation pénétrative de l'encaissant et découpage en losange d'un cristal de feldspath altéré en séricite. Observation en lumière polarisée non-analysée.

b) Foliation pénétrative de l'encaissant et découpage en losange d'un cristal de feldspath altéré en séricite. Observation en lumière polarisée analysée.

c) Feldspath altéré en séricite millimétrique fracturé par déformation fragile. Les macles polysynthétiques sont à plusieurs reprises recoupées par des failles micrométriques conjuguées. Observation en lumière polarisée analysée.

d) Feldspath millimétrique fracturé par déformation fragile. Les macles polysynthétiques sont recoupées par des failles d'ordre micrométrique à mouvement apparent senestre. Observation en lumière polarisée analysée.

e) Feldspath millimétrique plissé. Les macles polysynthétiques sont courbées avec un mouvement apparent dextre. Observation en lumière polarisée analysée.

f) Feldspath millimétrique plissé. Les macles polysynthétiques sont légèrement courbées.

BIBLIOGRAPHIE GÉNÉRALE

Ayer, J., Amelin, Y., Corfu, F., Kamo, S., Ketchum, J., Kwok, K., & Trowell, N. (2002). Evolution of the southern Abitibi greenstone belt based on U–Pb geochronology: autochthonous volcanic construction followed by plutonism, regional deformation and sedimentation. Precambrian Research, 115(1), p. 63-95.

Ayer, J. A. and Ontario Geological Survey. (2005). Overview of results from the greenstone architecture project: discover Abitibi initiative. Ontario Geological Survey.

Bateman, R. and Bierlein, F. P. (2007). On Kalgoorlie (Australia), Timmins–Porcupine (Canada), and factors in intense gold mineralisation. Ore Geology Reviews, 32(1), p. 187-206.

Beaudoin, G., & Pitre, D. (2005). Stable isotope geochemistry of the Archean Val-d 'Or (Canada) orogenic gold vein field. Mineralium Deposita, 40(1), 59-75.

Beaudry, D. (1992). Analyse structurale des assemblages volcanosédimentaires au voisinage de la faille Porcupine-Destor, Abitibi, Québec. Chicoutimi: Université du Québec à Chicoutimi.

Bédard, J. H., Harris, L. B., & Thurston, P. C. (2013). The hunting of the snArc.Precambrian Research, 229, p. 20-48.

Benn, K., & Peschler, A. P. (2005). A detachment fold model for fault zones in the Late Archean Abitibi greenstone belt. Tectonophysics, 400(1), p. 85-104.

Berger, B. R. (2001). Variation in styles of gold mineralization along the Porcupine–Destor deformation zone in Ontario: an exploration guide. Ontario Geological Survey Open File Report, 6070, 9-1.

Bigot, L. and Jébrak, M. (2015). Gold Mineralization at the Syenite-Hosted Beattie Gold Deposit, Duparquet, Neoarchean Abitibi Belt, Canada. Economic Geology, 110(2), p.315-335.

Bleeker, W., & Parrish, R. R. (1996). Stratigraphy and U-Pb zircon geochronology of Kidd Creek: implications for the formation of giant volcanogenic massive sulphide deposits and the tectonic history of the Abitibi greenstone belt. Canadian Journal of Earth Sciences, 33(8), p. 1213-1231.

Bleeker, W. (2012). Targeted Geoscience Initiative 4. Lode gold deposits in ancient deformed and metamorphosed terranes: the role of extension in the formation of Timiskaming basins and large gold deposits, Abitibi greenstone belt—a discussion. Ontario Geological Survey, Summary of Field Work and Other Activities, 47-1.

Bleeker, W. (2015). Synorogenic gold mineralization in granite-greenstone terranes: the deep connection between extension, major faults, synorogenic clastic basins, magmatism, thrust inversion, and long-term preservation. Targeted Geoscience Initiative 4: Contributions to the Understanding of Precambrian Lode Gold Deposits and Implications for Exploration, Geological Survey of Canada, Open File 7852, p. 25–47.

Bourdeau, J. (2013). Petrology, Mineralogy and Geochemistry of the Beattie Syenite and Country Rocks, Abitibi Greenstone Belt, Québec. University of Ottawa, 440p.

Cameron, E. M., & Hattori, K. (1987). Archean gold mineralization and oxidized hydrothermal fluids. Economic Geology, 82(5), p. 1177-1191.

Campbell, R. A. (2014). Controls on Syenite-Hosted Gold Mineralization in the Western Timmins Camp. The University of Western Ontario, 159p.

Card, K. D. (1990). A review of the Superior Province of the Canadian Shield, a product of Archean accretion. Precambrian Research, 48(1), p. 99-156.

Chown, E. H., Daigneault, R., Mueller, W., & Mortensen, J. K. (1992). Tectonic evolution of the northern volcanic zone, Abitibi belt, Quebec. Canadian Journal of Earth Sciences, 29(10), p. 2211-2225.

Chown, E. H., Harrap, R., & Moukhsil, A. (2002). The role of granitic intrusions in the evolution of the Abitibi belt, Canada. Precambrian Research, 115(1), p. 291-310.

Colvine, A. C. (1988). Archean lode gold deposits in Ontario, Ontario Ministry of Northern Development and Mines, Vol. 139, 136 p.

Cook, N. J., Ciobanu, C. L., & Mao, J. (2009). Textural control on gold distribution in As-free pyrite from the Dongping, Huangtuliang and Hougou gold deposits, North China Craton (Hebei Province, China). Chemical Geology, 264(1), p. 101-121.

Corfu, F., Jackson, S. L., & Sutcliffe, R. H. (1991). U-Pb ages and tectonic significance of late Archean alkalic magmatism and nonmarine sedimentation: Timiskaming Group, southern Abitibi belt, Ontario. Canadian Journal of Earth Sciences, 28(4), p. 489-503.

Corfu, F. (1993). The evolution of the southern Abitibi greenstone belt in light of precise U-Pb geochronology. Economic Geology, 88(6), p. 1323-1340.

Couture, J. F., & Pilote, P. (1993). The geology and alteration patterns of a disseminated, shear zone-hosted mesothermal gold deposit; the Francoeur 3 Deposit, Rouyn-Noranda, Quebec. Economic geology, 88(6), p. 1664-1684.

Daigneault, R., Mueller, W. U., & Chown, E. H. (2002). Oblique Archean subduction: accretion and exhumation of an oceanic arc during dextral transpression, Southern Volcanic Zone, Abitibi Subprovince Canada.Precambrian Research, 115(1), p. 261-290.

Daigneault, R., Mueller, W. U., & Chown, E. H. (2004). Abitibi greenstone belt plate tectonics: the diachronous history of arc development, accretion and collision. The Precambrian Earth: Tempos and Events, Series: Developments in Precambrian geology, 12, 88-103.

David, J., Dion, C., Goutier, J., Roy, P., Bandyayera, D., Legault, M., & Rhéaume, P. (2006). Datations U-Pb effectuees dans la Sous-province de l'Abitibi a la suite des travaux de 2004-2005. Ressources naturelles et faune Québec. 22p.

David, J., Davis, D. W., Dion, C., Goutier, J., Legault, M., & Roy, P. (2007). Datations U-Pb effectuées dans la Sous-province de l'Abitibi en 2005-2006 Ressources naturelles et faune, 17p.

David, J., McNicoll, V., Simard, M., Bandyayera, D., Hammouche, H., Goutier, J., Pilote, P., Rhéaume, P., Leclerc, F. and Dion, C. (2011).Datations U-Pb effectuées dans les provinces du Supérieur et de Churchill en 2009-2010. Ressources naturelles et faune Québec, 37p.

De La Roche, H., Leterrier, J., Grandclaude, P., & Marchal, M. (1980). A classification of volcanic and plutonic rocks using R 1 R 2-diagram and major-element analyses—its relationships with current nomenclature. Chemical geology, 29(1), p. 183-210.

Deditius, A. P., Utsunomiya, S., Ewing, R. C., & Kesler, S. E. (2009). Nanoscale "liquid" inclusions of As-Fe-S in arsenian pyrite. American Mineralogist, 94(2-3), p. 391-394.

Dimroth, E., Imreh, L., Rocheleau, M., & Goulet, N. (1982). Evolution of the south-central part of the Archean Abitibi Belt, Quebec. Part I: Stratigraphy and paleogeographic model. Canadian Journal of Earth Sciences, 19(9), p. 1729-1758.

Dimroth, E., Imreh, L., Goulet, N., & Rocheleau, M. (1983). Evolution of the south-central segment of the Archean Abitibi Belt, Quebec. Part II: Tectonic evolution and geomechanical model. Canadian Journal of Earth Sciences,20(9), p. 1355-1373.

Eilu, P., Mikucki, E. J., & Dugdale, A. L. (2001). Alteration zoning and primary geochemical dispersion at the Bronzewing lode-gold deposit, Western Australia. Mineralium Deposita, 36(1), p. 13-31.

El Goumi, N., De Souza, S., Enkin, R. J., & Dubé, B. Targeted Geoscience Initiative 4: Contributions to the Understanding of Precambrian Lode Gold Deposits and Implications for Exploration.

Faure, S., and Rafini, S. (2009) Modélisation des paléocontraintes le long de la Faille Destor-Porcupine: implication pour l'exploration aurifère. Forum technologique CONSOREM-Divex

Gaboury, D. (2013). Does gold in orogenic deposits come from pyrite in deeply buried carbon-rich sediments?: Insight from volatiles in fluid inclusions. Geology, 41(12), p.1207-1210.

Gebre-Mariam, M., Hagemann, S. G., & Groves, D. I. (1995). A classification scheme for epigenetic Archaean lode-gold deposits. Mineralium Deposita,30(5), p. 408-410.

Gifkins, C. C., Herrmann, W., & Large, R. R. (2005). Altered volcanic rocks: A guide to description and interpretation (Doctoral dissertation, Centre for Ore Deposit Research, University of Tasmania), 275p.

Goldfarb, R.J., Baker, T., Dubé, B., Groves, D.I., Hart, C.J.R. and Gosselin, P. (2005). Distribution, character, and genesis of gold deposits in metamorphic terranes. Economic Geology 100th anniversary, Vol. 40, p. 407-450

Goutier, J., & Lacroix, S. (1992). Géologie du secteur de la Faille de Porcupine-Destor dans les cantons de Destor et Duparquet: Ministère de l'Énergie et des Ressources. Québec, MB, 92-06, 62p.

Goutier, J. (1997). Géologie de la région de Destor (32D/07-200-0201). Gouvernement du Québec, Ministère des ressources naturelles, Secteur des mines. 37p.

Goutier, J. (2003a). Compilation géoscientifique, Géologie 1:20 000, Duparquet (32D11-200-0102). Ministère des Ressources naturelles du Québec; carte SIGÉOM SI-32D11B-C4G-05F.

Goutier, J. (2003b). Compilation géoscientifique, Géologie 1:20 000, Roquemaure (32D11-200-0101). Ministère des Ressources naturelles du Québec; carte SIGÉOM SI-32D11A-C4G-05F.

Grant, J. A. (1986). The isocon diagram; a simple solution to Gresens' equation for metasomatic alteration. Economic Geology, 81(8), p. 1976-1982.

Groves, D. I. (1993). The crustal continuum model for late-Archaean lode-gold deposits of the Yilgarn Block, Western Australia. Mineralium deposita, 28(6), p. 366-374.

Groves, D. I., Goldfarb, R. J., Gebre-Mariam, M., Hagemann, S. G. and Robert, F. (1998). Orogenic gold deposits: a proposed classification in the context of their crustal distribution and relationship to other gold deposit types. Ore geology reviews, 13(1), p. 7-27.

Groves, D. I., Goldfarb, R. J., Robert, F. and Hart, C. J. (2003). Gold deposits in metamorphic belts: overview of current understanding, outstanding problems, future research, and exploration significance. Economic Geology, 98(1), p. 1-29.

Guy, R. L. (1996). The geology of the Holloway gold deposit, Abitibi Greenstone Belt, Ontario. National Library of Canada= Bibliothèque nationale du Canada.

Helt, K. M., Williams-Jones, A. E., Clark, J. R., Wing, B. A., & Wares, R. P. (2014). Constraints on the genesis of the Archean oxidized, intrusion-related Canadian Malartic gold deposit, Quebec, Canada. Economic Geology, 109(3), p. 713-735.

Hubert, C., Trudel, P., & Gélinas, L. (1984). Archean wrench fault tectonics and structural evolution of the Blake River Group, Abitibi Belt, Quebec. Canadian Journal of Earth Sciences, 21(9), p. 1024-1032.

Jackson, S. L., Sutcliffe, R. H., Ludden, J. N., Hubert, C., Green, A. G., Milkereit, B., ... & Verpaelst, P. (1990). Southern Abitibi greenstone belt: Archean crustal structure from seismic-reflection profiles. Geology, 18(11), p. 1086-1090.

Jébrak, M., & Marcoux, É. (2008). Géologie des ressources minérales. Ministère des ressources naturelles et de la faune, 668 p.

Jensen, L. S. (1976). A new cation plot for classifying subalkalic volcanic rocks, Vol. 66. Ministry of Natural Resources.

Kishida, A., & Kerrich, R. (1987). Hydrothermal alteration zoning and gold concentration at the Kerr-Addison Archean lode gold deposit, Kirkland Lake, Ontario. Economic Geology, 82(3), p. 649-690.

Kerrich, R., Polat, A., & Xie, Q. (2008). Geochemical systematics of 2.7 Ga Kinojevis Group (Abitibi), and Manitouwadge and Winston Lake (Wawa) Fe-rich basalt–rhyolite associations: Backarc rift oceanic crust?. Lithos, 101(1), p. 1-23.

Lambert, G. (2001) Compilation géophysique, projet Pitt Gold, SOQUEM, GM 59030, 5 p. et 8 plans.

Large, R. R., Bull, S. W. and Maslennikov, V. V. (2011). A carbonaceous sedimentary source-rock model for Carlin-type and orogenic gold deposits. Economic Geology, 106(3), p. 331-358.

Legault, M., Fallara, F., Goutier, J., Perron, G., and Cheng., L.Z.(2003). Étude métallogenique et modélisation 3D de la Faille Destor-Porcupine dans le secteur de Duparquet, Sous-province de l'Abitibi (phase 1 de 3) Ministère des Ressources Naturelles et de la Faune, Québec, RP 2003-02, 16 p.

Legault, M., Goutier, J., Beaudoin, G. and Aucoin, M. (2005). Synthèse métallogenique de la Faille Destor-Porcupine, Ministère des Ressources Naturelles et de la Faune, Québec;
ET 2005-01, 37 p.

Luinstra, B. R. (2001). Structural geology of the Holloway mine, Abitibi greenstone belt, Ontario. Ontario Geological Survey. 50p.

Luinstra, B. R. (2004). Geology, structure and gold mineralization within the Porcupine-Destor Deformation Zone, Harker-Holloway gold camp, southwestern Abitibi Greenstone Belt, Canada.

Martin, R. D. (2012). Syenite-hosted gold mineralization and hydrothermal alteration at the Young-Davidson deposit, Matachewan, Ontario, 172p.

McNicoll, V., Goutier, J., Dubé, B., Mercier-Langevin, P., Ross, P. S., Dion, C. & Gibson, H. (2014). U-Pb Geochronology of the Blake River Group, Abitibi Greenstone Belt, Québec, and Implications for Base Metal Exploration. Economic Geology, 109(1), p. 27-59.

Morey, A. A., Tomkins, A. G., Bierlein, F. P., Weinberg, R. F., & Davidson, G. J. (2008). Bimodal distribution of gold in pyrite and arsenopyrite: examples from the Archean Boorara and Bardoc shear systems, Yilgarn Craton, Western Australia. Economic Geology, 103(3),p. 599-614.

Mueller, W., Donaldson, J. A., Dufresne, D., & Rocheleau, M. (1991). The Duparquet Formation: sedimentation in a late Archean successor basin, Abitibi greenstone belt, Quebec, Canada. Canadian Journal of Earth Sciences, 28(9), p. 1394-1406.

Mueller, W. U., Daigneault, R., Mortensen, J. K., and Chown, E. H. (1996). Archean terrane docking: upper crust collision tectonics, Abitibi greenstone belt, Quebec, Canada. Tectonophysics, 265(1), p. 127-150.

Mueller, W. U., Friedman, R., Daigneault, R., Moore, L., & Mortensen, J. (2012). Timing and characteristics of the Archean subaqueous Blake River megacaldera complex, Abitibi greenstone belt, Canada. Precambrian Research, 214, p. 1-27.

Olivo, G. R. and Williams-Jones, A. E. (2002). Genesis of the auriferous C quartz-tourmaline vein of the Siscoe mine, Val d'Or district, Abitibi subprovince, Canada: structural, mineralogical and fluid inclusion constraints. Economic Geology, 97(5), p.929-947.

Passchier, C. W., & Trouw, R. A. (1996). Microtectonics (Vol. 2). Berlin: Springer, 366p.

Percival, J. A. (2007). Geology and metallogeny of the Superior Province, Canada. Mineral Deposits of Canada: A Synthesis of Major Deposit-Types, District Metallogeny, the Evolution of Geological Provinces, and Exploration Methods, p. 903-928.

Pilote, P., McNicoll, V., Daigneault, R. and Moorhead, J. (2009) Géologie et nouvelles corrélations dans la partie ouest du Groupe de Malartic et dans le Groupe de Kinojévis, Québec. Congrès Abitibi 2009, GM 64195, p.55-60

Pitcairn, I. K., Teagle, D. A., Craw, D., Olivo, G. R., Kerrich, R. and Brewer, T. S. (2006). Sources of metals and fluids in orogenic gold deposits: insights from the Otago and Alpine Schists, New Zealand. Economic Geology, 101(8), p.1525-1546

Polat, A., & Kerrich, R. (2001). Magnesian andesites, Nb-enriched basalt-andesites, and adakites from late-Archean 2.7 Ga Wawa greenstone belts, Superior Province, Canada: implications for late Archean subduction zone petrogenetic processes. Contributions to Mineralogy and Petrology, 141(1), p.36-52.

Powell, W. G., Carmichael, D. M., & Hodgson, C. J. (1995). Conditions and timing of metamorphism in the southern Abitibi greenstone belt, Quebec.Canadian Journal of Earth Sciences, 32(6), p. 787-805.

Power-Fardy, D. and Breede, K. (2011). Technical report and mineral resource estimate update for the Duquesne-Ottoman Property, Québec, Canada. For Xmet Inc. 104 p.

Rabeau, O., Royer, J. J., Jébrak, M., & Cheilletz, A. (2013). Log-uniform distribution of gold deposits along major Archean fault zones. Mineralium Deposita, 48(7), p. 817-824.

Rafini, S. (2014). Typologie des minéralisations aurifères associées à la Faille de Cadillac. Rapport du projet CONSOREM 2011-01 et 2012-01, 45 p.

Robert, F., & Brown, A. C. (1986). Archean gold-bearing quartz veins at the Sigma Mine, Abitibi greenstone belt, Quebec; Part I, Geologic relations and formation of the vein system. Economic Geology, 81(3), p. 578-592.

Robert, F., & Brown, A. C. (1986). Archean gold-bearing quartz veins at the Sigma Mine, Abitibi greenstone belt, Quebec; Part II, Vein paragenesis and hydrothermal alteration. Economic Geology, 81(3), p. 593-616.

Robert, F. (2001). Syenite-associated disseminated gold deposits in the Abitibi greenstone belt, Canada. Mineralium Deposita, 36(6), p. 503-516

Ross, P. S., & Bédard, J. H. (2009). Magmatic affinity of modern and ancient subalkaline volcanic rocks determined from trace-element discriminant diagrams. Canadian Journal of Earth Sciences, 46(11),p. 823-839.

Robert, F., Poulsen, K. H., Cassidy, K. F. and Hodgson, C. J. (2005). Gold metallogeny of the Superior and Yilgarn cratons. Economic Geology 100th anniversary, p. 1001-1033.

Schwarcz, H. P., & Rees, C. E. (1986). Sulphur isotope studies of Archean gold deposits. Ontario Ministry of Northern Development and Mines.

Simard, M., Gaboury, D., Daigneault, R., & Mercier-Langevin, P. (2013). Multistage gold mineralization at the Lapa mine, Abitibi Subprovince: insights into auriferous hydrothermal and metasomatic processes in the Cadillac–Larder Lake Fault Zone. Mineralium Deposita, 48(7), p. 883-905

Stott, G. M., Corkery, M. T., Percival, J. A., Simard, M., & Goutier, J. (2010). 20. Project Units 98-006 and 98-007. A Revised Terrane Subdivision of the Superior Province.

Taylor, S. R., McLennan, S. M., Armstrong, R. L., & Tarney, J. (1981). The composition and evolution of the continental crust: rare earth element evidence from sedimentary rocks [and discussion]. Philosophical Transactions of the Royal Society of London A: Mathematical, Physical and Engineering Sciences, 301(1461), p. 381-399.

Thurston, P. C., Ayer, J. A., Goutier, J., & Hamilton, M. A. (2008). Depositional gaps in Abitibi greenstone belt stratigraphy: a key to exploration for syngenetic mineralization. Economic Geology, 103(6), p. 1097-1134.

Trudel, P., Hoy, L., Gaulin, R., Lao, K. (1991). Géologie de la mine Elder, canton de Beauchastel – Région de Rouyn-Noranda. Ministère de l'Énergie, des Mines et des Ressources du Québec. MB 91-09, 153p.

Tullis, J., & Yund, R. A. (1987). Transition from cataclastic flow to dislocation creep of feldspar: mechanisms and microstructures. Geology, 15(7), p. 606-609.

Tullis, J., & Yund, R. A. (1991). Diffusion creep in feldspar aggregates: experimental evidence. Journal of Structural Geology, 13(9), p. 987-1000.

White, N. C., & Hedenquist, J. W. (1995). Epithermal gold deposits: styles, characteristics and exploration. SEG newsletter, 23(1), p. 9-13.

Winchester, J. A., & Floyd, P. A. (1977). Geochemical discrimination of different magma series and their differentiation products using immobile elements. Chemical geology, 20, p. 325-343.

Wood, P. C. (1991). The Hollinger-McIntyre gold-quartz vein system, Timmins, Ontario: geologic characteristics, fluid properties and light stable isotope geochemistry. Ontario Ministry of Northern Development and Mines, Ontario Geological Survey. 402p.

Wong, L., Davis, D. W., Krogh, T. E., & Robert, F. (1991). U Pb zircon and rutile chronology of Archean greenstone formation and gold mineralization in the Val d'Or region, Quebec. Earth and Planetary Science Letters, 104(2), p. 325-336.

Xue, Y., Campbell, I., Ireland, T. R., Holden, P., & Armstrong, R. (2013). No mass-independent sulfur isotope fractionation in auriferous fluids supports a magmatic origin for Archean gold deposits. Geology, 41(7), p. 791-794.